/
Article / Book Information

| ( )	
Title(English)	Production, Transport , and Induction Acceleration of Heavy Ion Beams in the KEK Digital Accelerator
( )	
Author(English)	Xingguang Liu
( )	: ( ), : , : 10025 , :2015 12 31 , : , : , , , , ,
Citation(English)	Degree:Doctor (Science), Conferring organization: Tokyo Institute of Technology, Report number: 10025 , Conferred date:2015/12/31, Degree Type:Course doctor, Examiner:,,,,,
( )	
Type(English)	Doctoral Thesis

A THESIS PRESENTED FOR THE DEGREE OF
DOCTOR OF SCIENCE

Production, Transport, and Induction Acceleration of Heavy Ion Beams in the KEK Digital Accelerator

Xingguang LIU

supervisors:
Professor Ken TAKAYAMA
Professor Kazuhiko HORIOKA
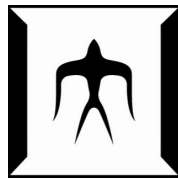
DEPARTMENT OF ENERGY SCIENCES

TOKYO INSTITUTE OF TECHNOLOGY
December, 2015

Abstract

Experimental and theoretical studies for the fast-cycling induction synchrotron, the KEK Digital Accelerator (KEK-DA), have been conducted. They cover whole the aspects of this accelerator from the ion source to the ring. Crucial issues that have been observed in the existing ion source, such as discharge in the extraction gap, was resolved to provide stable heavy ion beams for beam transport experiments and acceleration experiments. In order to understand beam optics in the beam transportation line, a quasi-3D profile monitor was developed. Momentum error in the beam bunch, which is originated from the longitudinal chopping mechanism in the Einzel lens and beam loading effects on the extraction and post-acceleration devices, has been clearly observed. A 3D particle tracking code was developed to understand the beam behavior observed in the KEK-DA ring. These works are not only useful for the present studies of the KEK-DA, but also insightful for the development of future induction synchrotron accelerators. Thesis describes entire beam physics of the KEK-DA including the injector.

Contents

Contents

Chapter 1

Introduction

1.1 Induction synchrotron concept

The concept of induction synchrotron was proposed in 2000 by K. Takayama and J. Kishiro [1].

By simply replacing RF cavities in a traditional synchrotron with induction cells, this concept has at least the following advantages compared with the conventional RF based synchrotron:

1). Wide band acceleration

2). Capability of accelerating all species of ion with possible charge state

3). Super bunch acceleration

4). Flexible beam manipulation in the longitudinal phase space

In fact, they are realized by two essential features of the induction synchrotron: intrinsic pulse acceleration scheme in an induction acceleration system and the separation of the longitudinal beam acceleration and confinement. The two features can be explained by the comparison between the RF synchrotron and the induction synchrotron.

The first feature comes directly from the adaption of the Switching Power Supply (SPS) which directly drives the induction cell. Solid-state switches employed in the SPS can generate the pulse when it is necessary, for example, when accelerating the beam as it passes through the induction cell. Unlike a RF system which has to work within a bandwidth, the SPS generates the pulses on demand. Although it has an upper band limits of 1 MHz at present, it covers such a wide bandwidth that is
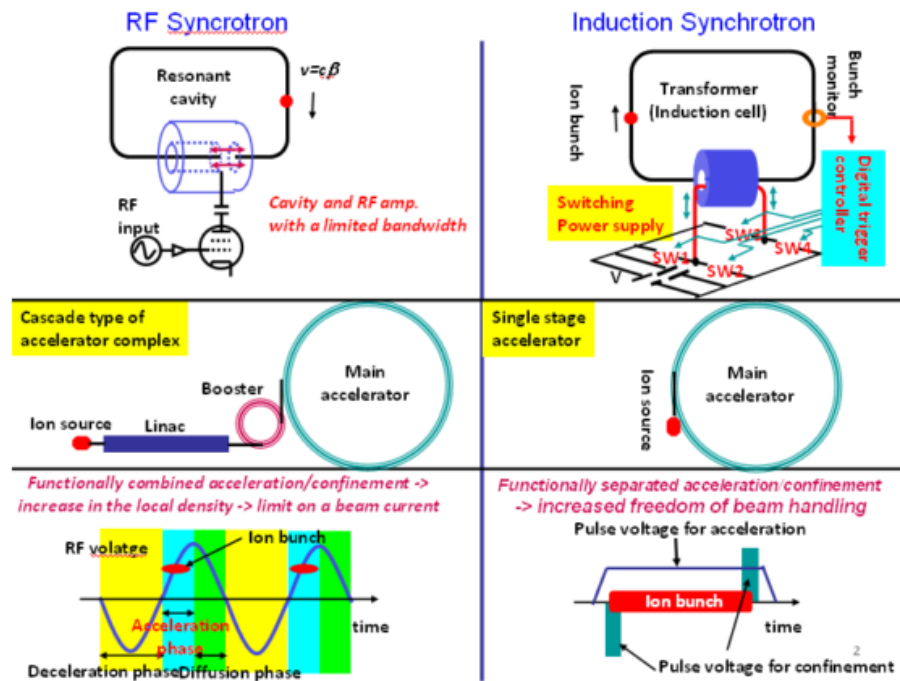
Figure 1.1: Comparison between the RF synchrotron and the induction synchrotron.

impossible for a RF system. This wide band operation make it possible to accelerate the heavy ion beam from very low energy to the high energy in a single ring. For the same reason, in principle, it can accelerate any ion species of any charge state at any injection energy [2].

The second feature comes from the fact that it separates the acceleration and longitudinal confinement as shown in the bottom figure of Fig. 1.1. The RF synchrotron has a feature that the acceleration and the longitudinal confinement of the beam are realized at the same time. In the induction synchrotron, the beam will be accelerated with an voltage pulse whose width should cover the whole beam length. Because the voltage pulses are given by the SPS, the beam length can be as long as it can fill in the ring and be covered by the acceleration voltage pulse. Note that this beam length should be less than the revolution period of the beam traveling in the ring because the induction cell has to be reset with an inversed voltage pulse. This feature is called super bunch acceleration [3].

The validity of replacing the RF cavities with induction cells was successfully demonstrated in 2006 when the proton beam was accelerated from $500\,\mathrm{MeV}$ to $6\,\mathrm{GeV}$ [4] using the KEK Proton Synchrotron (KEK-PS) right before it was shut down.

1.2   The KEK Digital Accelerator

The induction acceleration in the KEK-PS was a demonstration of slow cycling induction synchrotron where the beam revolution period in the ring was not so short and stayed within a small frequency range. In order to demonstrate an induction synchrotron with wide band acceleration of heavy ion beams, the former fast cycling booster synchrotron for the KEK-PS was modified to the new induction accelerator. This new accelerator is called the KEK Digital Accelerator (KEK-DA) [5]. The following hardwares has been developed and implemented for the KEK-DA,

1). Ion source: construction of an Electron Cyclotron Electron Resonance Ion Source(ECRIS) and a $200\,\mathrm{kV}$ high voltage platform; development of an Einzel Lens Chopper as a longitudinal chopper.

2). Beam transport line: rearrangement of the low energy transport line(LEBT).

3). KEK-DA Ring: development of an Electrostatic Injection Kicker; induction cells installation; improvement of the vacuum.

The beam commissioning has started in 2010 and the recent commissioning results can be found as in [6–8].

1.3 Thesis work and structure

This thesis will discuss the experimental studies and simulation works on beam dynamics related to the KEK-DA from the ion source to the ring. It is organized in the following structure.

In the next chapter, Chapter 2, the beam dynamics of the induction synchrotron will be reviewed. The most fundamental beam dynamics of the transverse motion in an circular accelerator is included as well as the unique longitudinal beam motion in an induction synchrotron. This chapter serves as the theoretical backgroud of the experimental studies in Chapter 5 and the simulation studies in Chapter 6 and Chapter 7.

Chapter 3 presents the outline of the KEK-DA including the most recent development related to the thesis work. The ion source, LEBT line, electrostatic injection kicker, the KEK-DA ring, induction acceleration system, trigger system and diagnostic system will be introduced. Description of these subsystems is necessary to get a complete image of this facility. In addition, the sources of some phenomenon observed at downstream are found to be from the upstream. For example, the beam loading effects found in the extraction region of the ion source and the post-acceleration column are the sources of the momentum modulation in time, which will be discussed in Chapter 5.

Chapter 4 will give a brief review on the ion source and the production of ion beams in the KEK-DA ECRIS. Several operational optimizations such as the extraction voltage, the Einzel Lens Chopper settings and the gas flow rate have been done so as to realize the best performance of the KEK-DA ECRIS after the modification work in Chapter 3. The experimental studies in Chapter 5 also relies on the work of this chapter. The results in this chapter also reveal the limits of present ion source.

Chapter 5 describes two experimental studies on the LEBT line in order to understand the beam distribution in phase space which is important for injection match and beam loss discussion in the ring. In the first study, the Courant-Snyder parameters of the beam were measured experimentally with the wire-grid profile monitor. In the other study, the wire grid profile monitor was modified in order to capture the beam profile in a quasi-3D way. This newly developed method make it possible to measure the longitudinal momentum deviation within a beam pulse. These studies are not only useful to understand the upstream status of the beam but also necessary for the beam study in the ring.

Chapter 6 introduces a 3D tracking simulation code specifically developed for the induction synchrotron. The beam distribution in 6D phase space evolution is calculated by the transfer matrix along the beam line. A sub-3D space charge solver

is included in this simulation code. Details of this space charge solver will be given with justification results. The most noticeable feature of this particle tracking code is the inclusion of the practical boundaries of vacuum duct or other element in a beam line.

Chapter 7 discusses the simulation studies of the KEK-DA. Beam loss under the injection magnetic field is discussed by comparing the results of the beam survival rate from the simulation and the beam commissioning.

Chapter 8 summarizes the thesis work and gives some perspectives on the following studies related to this thesis work.

The highlights of this thesis work are Chapter 5, Chapter 6 and Chapter 7. In the second experimental study in Chapter 5, we developed a quasi-3D profile monitor by modifying present wire-grid based profile monitor. The new profile monitor made it possible to give the beam profile with time-structure. As an application, the longitudinal momentum deviation in a beam pulse was experimentally measured. Chapter 6 describes the developed 3D tracking simulation code. This is the first and the only code available at present for the induction synchrotron as a comprehensive design and study tool featuring sub-3D space charge solver. In Chapter 7, preliminary simulation results are shown, suggesting that for present KEK-DA, space charge plays only limited role on the beam loss in the KEK-DA ring.

Chapter 2

Beam Dynamics of an Induction synchrotron

In this chapter, the single particle motion of a charged particle in an electromagnetic field in the Hamiltonian form will be briefly reviewed. Then the equations of motion can be derived from the Hamiltonian. These equations of motion are then expressed in the form of transfer matrix which is convenient to use in the particle tracking simulation.

The longitudinal motion of an induction synchrotron is different from that of a conventional RF synchrotron. The longitudinal beam confinement and acceleration in the induction synchrotron will be discussed by comparing it with the RF synchrotron.

In the end, the "pulse density control" scheme which is adopted in the KEK-DA is introduced.

2.1 Single particle motion and transfer matrix

2.1.1 Single particle motion

Particle motion under the electromagnetic fields

The force on a particle of charge q traveling with a velocity $\mathbf{v}$ under the electric field $\mathbf{E}$ (electric field strength) and magnetic field $\mathbf{B}$ (magnetic flux density) is:

$$\mathbf{F} = q(\mathbf{E} + \mathbf{v} \times \mathbf{B}) \tag{2.1}$$

From Newton's second law, the motion of the particle is governed by:

$$\frac{d\mathbf{p}}{dt} = \mathbf{F} \tag{2.2}$$

Meanwhile, the Maxwell's equations in the differential form are:

$$\nabla \cdot \mathbf{D} = \rho \tag{2.3}$$

$$\nabla \cdot \mathbf{B} = 0 \tag{2.4}$$

$$\nabla \times \mathbf{H} = J + \frac{\partial \mathbf{D}}{\partial t} \tag{2.5}$$

$$\nabla \times \mathbf{E} = -\frac{\partial \mathbf{B}}{\partial t} \tag{2.6}$$

where ρ is the electric charge density (charge per unit volume, $\mathrm{C/m^3}$) and the J is electric current density. The electric displacement $\mathbf{D}$ and magnetic field $\mathbf{H}$ are related to the electric field $\mathbf{E}$ and magnetic flux density $\mathbf{B}$ as follows:

$$\mathbf{D} = \varepsilon \mathbf{E} \tag{2.7}$$

$$\mathbf{B} = \mu \mathbf{H} \tag{2.8}$$

The electric permittivity ε and the magnetic permeability μ depends on the medium where the fields exist. In the vacuum, they are defined as:

$$\varepsilon_0 = 8.854 \times 10^{-12} \ \mathrm{F/m} \tag{2.9}$$

$$\varepsilon_0 \mu_0 = \frac{1}{c^2} \tag{2.10}$$

Hamiltonian

In Hamiltonian mechanics, the Hamiltonian plays a role similar to the total energy as in Newtonian mechanics.

$$H = T + V \tag{2.11}$$

where T is the kinetic energy and V is the potential energy. As a matter of fact, the Hamiltonian is expressed as a function of the coordinates and the momentum. For example, the dynamics of a given system is described by the Hamilton's equations:

$$\frac{dx_i}{dt} = \frac{\partial H}{\partial p_i} \tag{2.12}$$

$$\frac{dp_i}{dt} = -\frac{\partial H}{\partial x_i} \tag{2.13}$$

where x_i ($i = 1, 2, 3, ..., N$ for N dimensional space) are the coordinates of the particle, p_i are the canonical momentum, and H is the Hamiltonian.

In the Hamiltonian mechanics, for the particle motion in an electromagnetic field, the equations of motion are usually expressed in terms of the scalar potential ϕ and the vector potential $\mathbf{A}$, instead of the electric field strength and magnetic flux density in Eq. (2.1). They are defined as:

$$\mathbf{B} = \nabla \times \mathbf{A} \tag{2.14}$$

$$\mathbf{E} = -\nabla\phi - \frac{\partial \mathbf{A}}{\partial t} \tag{2.15}$$

Usually, the scalar potential ϕ and the vector potential $\mathbf{A}$ are functions of the coordinates x, y and z. If the electromagnetic field is time dependent, they are also function of t. Accordingly, the canonical momentum is defined as,

$$\mathbf{P} = m\mathbf{v} + q\mathbf{A} \tag{2.16}$$

In the Newtonian mechanics in free space, the total energy E of a particle moving with relativistic velocity v, is then given as,

$$E = \gamma m c^2 \tag{2.17}$$

$$\mathbf{p} = \gamma \boldsymbol{\beta} m c \tag{2.18}$$

$$E^2 = (\mathbf{p}c)^2 + (mc^2)^2 \tag{2.19}$$

where c is the speed of the light and,

$$\beta = v/c \tag{2.20}$$

$$\gamma = 1/\sqrt{1 - \beta^2} \tag{2.21}$$

In the existence of electromagnetic field, if we simply include the scalar potential and the vector potential to the total energy in Eq. (2.17) and the momentum in Eq. (2.18):

$$E' = \gamma mc^2 + q\phi \tag{2.22}$$
$$\mathbf{P} = \gamma\boldsymbol{\beta}mc + q\mathbf{A} \tag{2.23}$$

Now with Eq. (2.19) the total energy E' can be solved to be the Hamiltonian,

$$H = c\sqrt{(\mathbf{P} - q\mathbf{A})^2 + (mc)^2} + q\phi \tag{2.24}$$

where now it is expressed in terms of the canonical momentum $\mathbf{P}$, the scalar potential ϕ and the vector potential $\mathbf{A}$. The Hamiltonian in Eq. (2.24) follows the Hamiltonian in Eq. (2.12) and Eq. (2.13) where the independent variable is the time t. However, in accelerator physics, where the magnetic field is dependent on the position along the beam line, it is more convenient to use the distance along the path as the independent variable.

Considering one dimensional case, perform the following integral from time t_0 to t_1,

$$S = \int_{t_0}^{t_1} P\dot{x} - Hdt \tag{2.25}$$

where S is called the action. The change of action is,

$$\delta S = \int_{t_0}^{t_1} \delta P\dot{x} + P\delta\dot{x} - \delta Hdt \tag{2.26}$$

where the change of Hamiltonian H is (with Eq. (2.12) and Eq. (2.13),$\dot{x} = \frac{dx}{dt}$, $\dot{P} = \frac{dP}{dt}$),

$$\delta H = \frac{\partial H}{\partial x}\delta x + \frac{\partial H}{\partial P}\delta P$$
$$= -\dot{P}\delta x + \dot{x}\delta P \tag{2.27}$$

Now Eq. (2.26) becomes,

$$\delta S = \int_{t_0}^{t_1} P\delta\dot{x} + \dot{P}\delta xdt = \int_{t_0}^{t_1} \frac{d}{dt}(P\delta x)dt = (P\delta x)|_{t_0}^{t_1} \tag{2.28}$$

For a given t_0 and t_1, $\delta x = 0$ for both points in the phase space (x, p). This is the Hamilton's principle [9] which states that the motion of the system from time t_0 to t_1, the action integral has a stationary value for the actual path of the motion or the

variation of the action integral is zero. The action in Eq. (2.25) can be also expressed in terms of the coordinate x.

$$
\begin{aligned}
S &= \int_{x_0}^{x_1} (P\dot{x} - H)\frac{dt}{dx}dt \\
&= \int_{x_0}^{x_1} -H\frac{dt}{dx} + Pdx
\end{aligned}
\tag{2.29}
$$

By observing Eq. (2.25) and Eq. (2.29), one can find that if P is replaced with $-H$ in Eq. (2.25), x and t change their roles, a new set of Hamiltonian equations can be written as,

$$
\frac{dt}{dx} = \frac{\partial P}{\partial H}
\tag{2.30}
$$

$$
\frac{dH}{dx} = -\frac{\partial P}{\partial t}
\tag{2.31}
$$

where the $-P$ works as a Hamiltonian. In the three dimensional case, the action can be written as,

$$
S = \int_{x_0}^{x_1} P_x\dot{x} + P_y\dot{y} + P_z\dot{z} - H dt
\tag{2.32}
$$

In case of particle moving along z in a Cartesian system, $-P_z$ works like a Hamiltonian while (x, Px) and (y, Py) stay the same. By rewriting Eq. (2.24), the new Hamiltonian expressed as $-P_z$ is,

$$
H' = -P_z = -\sqrt{\frac{(E - q\phi)^2}{c^2} - (P_x - qA_x)^2 - (P_y - qA_y)^2 - m^2c^2} - qA_z
\tag{2.33}
$$

Dynamical variables

Usually beam lines are designed for a specific referential particle while within a beam all the particles have different positions and momenta. Therefore, the relative information of individual particle to the referential particle is more useful. In a Cartesian coordinate system, the scaled momenta in terms of the referential momentum can be chosen as:

11

$$p_x = \frac{P_x}{p_0} \tag{2.34}$$

$$p_y = \frac{P_y}{p_0} \tag{2.35}$$

$$p_z = \frac{E}{cp_0} - \frac{1}{\beta_0} \tag{2.36}$$

where P_x, P_y are the canonical momenta, E is the total energy as in Eq. (2.17) and the referential momentum is defined as in Eq. (2.18), $p_0 = \beta_0\gamma_0 mc$. The meaning of p_z can be seen more clearly from Eq. (2.36) and Eq. (2.17),

$$p_z = \frac{E}{\beta_0 E_0} - \frac{1}{\beta_0} = \frac{1}{\beta_0}\frac{\Delta E}{E_0} \tag{2.37}$$

where $\Delta E = E - E_0$ is the energy difference from the referential particle. In terms of the momentum deviation,

$$\delta = \frac{\Delta p}{p_0} \tag{2.38}$$

where $\Delta p = p - p_0$, and with the relationship,

$$\frac{\Delta p}{p} = \frac{1}{\beta^2}\frac{\Delta E}{E} \tag{2.39}$$

then p_z is,

$$p_z = \beta_0\delta \tag{2.40}$$

Similarly, the scaled vector potential can be also chosen as,

$$\mathbf{a} = \frac{q}{p_0}\mathbf{A} \tag{2.41}$$

Now Eq. (2.34) and Eq. (2.35) can be explicitly expressed as,

$$P_x = \frac{\beta_x\gamma mc}{P_0} + a_x \tag{2.42}$$

$$P_y = \frac{\beta_y\gamma mc}{P_0} + a_y \tag{2.43}$$

As for the position coordinates, the referential particle is assumed to be moving along s at time t, which is along the longitudinal direction, the relative particle position coordinates can be expressed as (X, Y, Z), with Z defined as,

$$Z = \frac{s}{\beta_0} - ct \tag{2.44}$$

$$= \frac{1}{\beta_0}(s - \beta_0 ct) = \frac{1}{\beta_0}\Delta s = c\Delta t \tag{2.45}$$

where $\Delta s = s - s_0$ is the distance and the Δt is the time difference from the referential particle.

The dynamical variables used to describe the particle motion now can be summarized as a vector (X, p_x, Y, p_y, Z, p_z). With these variables, the scaled Hamiltonian (with the same notation here, H_s) is,

$$H = \delta - \sqrt{\left(\frac{1}{\beta_0} - \frac{q\phi}{cP_0} + \beta_0\delta\right)^2 - (p_x - a_x)^2 - (p_y - a_y)^2 - \frac{1}{\beta_0^2\gamma_0^2}} - a_z \tag{2.46}$$

Hamiltonian in a curved coordinate system

In the accelerator system, the beam line is usually a curved one. Thus, instead of the Cartesian coordinates such as (x, y, z), the curved coordinates (x, y, s) are often used to describe the particle motion, where s is the moving direction of the referential particle, or the tangential line along the curved orbit. Now we denote the Cartesian coordinate as (X, Y, Z) and the curved coordinates as x, y, s as shown in Fig. 2.1.
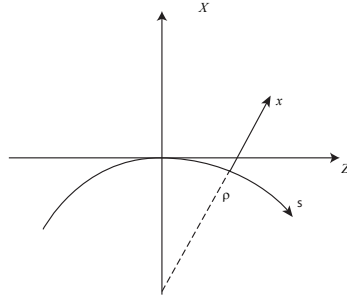
Figure 2.1: Cartesian coordinates and curved coordinates.

The relationship between the Cartesian coordinate and the curved coordinates are simply given:

13

$$X = (x + \rho)\cos(\frac{s}{\rho}) - \rho \tag{2.47}$$

$$Y = y \tag{2.48}$$

$$Z = (x + \rho)\sin(\frac{s}{\rho}) \tag{2.49}$$

Finally, the Hamiltonian turns out to be,

$$H = \delta - (1 + hx)\sqrt{\left(\frac{1}{\beta_0} - \frac{q\phi}{cP_0} + \beta_0\delta\right)^2 - (p_x - a_x)^2 - (p_y - a_y)^2 - \frac{1}{\beta_0^2\gamma_0^2}} - (1 + hx)a_s \tag{2.50}$$

where h is the curvature of the referential orbit $h = 1/\rho$ and the independent variable is s.

2.1.2 Transfer matrix

Reduced Hamiltonian

With the Hamiltonian expressed in Eq. (2.50), the particle of motion can be derived under specific electromagnetic field defined by the scalar potential ϕ and the vector potential $\mathbf{A}$. The Hamiltonian equations for Eq. (2.50) are,

$$\frac{dx_i}{ds} = \frac{\partial H}{\partial p_i} \tag{2.51}$$

$$\frac{dp_i}{ds} = -\frac{\partial H}{\partial x_i} \tag{2.52}$$

The most common component in accelerators are magnets which have no magnetic field in the longitudinal direction, namely $A_x = A_y = 0$. In addition, there is no electric field for these magnets, thus $\phi = 0$. Now the Hamiltonian in Eq. (2.50) reduces to,

$$H = \delta - (1 + hx)\sqrt{\left(\frac{1}{\beta_0} + \beta_0\delta\right)^2 - p_x{}^2 - p_y{}^2 - \frac{1}{\beta_0^2\gamma_0^2}} - (1 + hx)a_s \tag{2.53}$$

But the results still have complexness. To simplify the problem, the square root part of the Hamiltonian in Eq. (2.53) can be expanded to the second order in terms p_x and p_y,

$$
\sqrt{\left(\beta_0\delta + \frac{1}{\beta_0}\right)^2 - p_x^2 - p_y^2 - \frac{1}{\beta_0^2\gamma_0^2}}
$$

$$
= (\sqrt{2\delta + \frac{1}{\beta_0^2} + \delta^2\beta_0^2 - \frac{1}{\beta_0^2\gamma_0^2}} - \frac{p_y^2}{2\sqrt{2\delta + \frac{1}{\beta_0^2} + \delta^2\beta_0^2 - \frac{1}{\beta_0^2\gamma_0^2}}} + O[p_y]^3)
$$

$$
+ (-\frac{1}{2\sqrt{2\delta + \frac{1}{\beta_0^2} + \delta^2\beta_0^2 - \frac{1}{\beta_0^2\gamma_0^2}}} - \frac{p_y^2}{4\left(2\delta + \frac{1}{\beta_0^2} + \delta^2\beta_0^2 - \frac{1}{\beta_0^2\gamma_0^2}\right)^{3/2}} + O[p_y]^3)p_x^2 + O[p_x]^3
$$

$$
\tag{2.54}
$$

Notice that

$$
\frac{1}{\beta_0^2} - \frac{1}{\beta_0^2\gamma_0^2} = \frac{1 - \frac{1}{\gamma_0^2}}{\beta_0^2} = 1
\tag{2.55}
$$

and assume,

$$
D = \sqrt{2\delta + \beta_0{}^2\delta^2 + 1}
\tag{2.56}
$$

Hamiltonian in Eq. (2.53) is now reduced to,

$$
H = \delta + (1 + hx)\left(\frac{p_x^2}{2D} + \frac{p_y^2}{2D} - D - a_s\right)
\tag{2.57}
$$

which is valid only when $\frac{p_x^2 + p_y^2}{D^2} \ll 1$. This approximation is usually referred to as paraxial approximation or small angle approximation.

Drift space

In case of a drift space, the curvature to be zero, $h = 0$, and there is no magnetic field ($a_s = 0$), the Hamiltonian is then,

$$
H = \delta - \sqrt{\left(\beta_0\delta + \frac{1}{\beta_0}\right)^2 - p_x^2 - p_y^2 - \frac{1}{\beta_0^2\gamma_0^2}}
\tag{2.58}
$$

or to the second order of transverse momenta,

$$
H = \delta + \frac{p_x^2}{2D} + \frac{p_y^2}{2D} - D
\tag{2.59}
$$

15

Furthermore, expand this equation to the second order in terms of D and $1/D \approx 1$,

$$H = -1 + \frac{1}{2}\left(p_x^2 + p_y^2\right) + \frac{\delta^2}{2\gamma_0^2} \tag{2.60}$$

Apply Eq. (2.51) and Eq. (2.52) to each pair $(x, p_x), (y, p_y)$ and (z, p_z),

$$\frac{dp_x}{ds} = \frac{-\partial H}{\partial x} = 0 \tag{2.61}$$

$$\frac{\mathrm{d}x}{\mathrm{d}s} = \frac{\partial H}{\partial p_x} = p_x \tag{2.62}$$

$$\frac{\mathrm{d}p_y}{\mathrm{d}s} = \frac{-\partial H}{\partial y} = 0 \tag{2.63}$$

$$\frac{\mathrm{d}y}{\mathrm{d}s} = \frac{\partial H}{\partial p_y} = p_y \tag{2.64}$$

$$\frac{\mathrm{d}(\beta_0\delta)}{\mathrm{d}s} = \frac{-\partial H}{\partial z} = 0 \tag{2.65}$$

$$\frac{\mathrm{d}z}{\mathrm{d}s} = \frac{\partial H}{\partial p_z} = \frac{\delta}{\beta_0\gamma_0^2} \tag{2.66}$$

where Eq. (2.40) has been used.

Suppose the particle travels from $s1$ to $s2$ and $L = s2 - s1$, these equations can be solved exactly as,

$$p_{x2} = p_{x1} \tag{2.67}$$
$$x_2 = x_1 + p_{x1}L \tag{2.68}$$
$$p_{y2} = p_{y1} \tag{2.69}$$
$$y_2 = y_1 + p_{y1}L \tag{2.70}$$
$$\beta_0\delta_2 = \beta_0\delta_1 \tag{2.71}$$
$$z_2 = z_1 + \frac{\delta_1}{\beta_0\gamma_0^2}L \tag{2.72}$$

Notice that these equations can be written in the form of the matrix,

$$\mathbf{x_{s2}} = M\mathbf{x_{s1}} \tag{2.73}$$

where M is a 6×6 matrix and $\mathbf{x} = (x, p_x, y, p_y, z, \beta_0\delta)$. M is called transfer matrix. For example, above equations can be written as,

$$
\begin{pmatrix} x \\ p_x \\ y \\ p_y \\ c\Delta t \\ \beta_0\delta \end{pmatrix}_{s2}
=
\begin{pmatrix}
1 & L & 0 & 0 & 0 & 0 \\
0 & 1 & 0 & 0 & 0 & 0 \\
0 & 0 & 1 & L & 0 & 0 \\
0 & 0 & 0 & 1 & 0 & 0 \\
0 & 0 & 0 & 0 & 1 & \frac{L}{\beta_0^2\gamma_0^2} \\
0 & 0 & 0 & 0 & 0 & 1
\end{pmatrix}
\begin{pmatrix} x \\ p_x \\ y \\ p_y \\ c\Delta t \\ \beta_0\delta \end{pmatrix}_{s1}
\tag{2.74}
$$

For practical use, especially for the experiment, $(\Delta t, \delta)$ is much more meaningful than (z, p_z) for the longitudinal direction. For example, Δt describes the time difference of a particle to the referential particle. Experimentally, for a bunched beam, the longitudinal change of the beam intensity can be measured in terms of time by an oscilloscope. The momentum deviation δ is also easy to use than the canonical variable p_z. The relationship between the two sets can be seen from Eq. (2.40) and Eq. (2.43). Accordingly, the transfer matrix becomes,

$$
\begin{pmatrix} x \\ p_x \\ y \\ p_y \\ \Delta t \\ \delta \end{pmatrix}_{s2}
=
\begin{pmatrix}
1 & L & 0 & 0 & 0 & 0 \\
0 & 1 & 0 & 0 & 0 & 0 \\
0 & 0 & 1 & L & 0 & 0 \\
0 & 0 & 0 & 1 & 0 & 0 \\
0 & 0 & 0 & 0 & 1 & \frac{L}{\beta_0 c\gamma_0^2} \\
0 & 0 & 0 & 0 & 0 & 1
\end{pmatrix}
\begin{pmatrix} x \\ p_x \\ y \\ p_y \\ \Delta t \\ \delta \end{pmatrix}_{s1}
\tag{2.75}
$$

Another convenient choice for the coordinates of the longitudinal direction is $(\Delta s, \delta)$, with which the transfer matrix becomes,

$$
\begin{pmatrix} x \\ p_x \\ y \\ p_y \\ \Delta s \\ \delta \end{pmatrix}_{s2}
=
\begin{pmatrix}
1 & L & 0 & 0 & 0 & 0 \\
0 & 1 & 0 & 0 & 0 & 0 \\
0 & 0 & 1 & L & 0 & 0 \\
0 & 0 & 0 & 1 & 0 & 0 \\
0 & 0 & 0 & 0 & 1 & \frac{L}{\gamma_0^2} \\
0 & 0 & 0 & 0 & 0 & 1
\end{pmatrix}
\begin{pmatrix} x \\ p_x \\ y \\ p_y \\ \Delta s \\ \delta \end{pmatrix}_{s1}
\tag{2.76}
$$

17

Dipole

In case of a pure dipole, the magnetic field is in the vertical direction,

$$\mathbf{B} = (0, B_0, 0) \tag{2.77}$$

The potential vector for such a field can be found as,

$$\mathbf{A} = \left(0, 0, \frac{B_0 h x^2}{2(hx+1)} - B_0 x\right) \tag{2.78}$$

It can be confirmed that $\mathbf{B} = \nabla \times \mathbf{A}$ and $\nabla \cdot \mathbf{B} = 0$. A scaled vector potential can be written as,

$$\mathbf{a} = \frac{q}{P_0}\mathbf{A} = \left(0, 0, -k_0 x + \frac{k_0 h x^2}{2(1+hx)}\right) \tag{2.79}$$

where,

$$k_0 = \frac{B_0 q}{p_0} \tag{2.80}$$

Put the Eq. (2.79) and Eq. (2.80) back to Eq. (2.53) and expand the Hamiltonian to the second order in terms of p_x, p_y and δ, dropping the higher orders,

$$H = \frac{p_x^2}{2} + \frac{p_y^2}{2} + \frac{\delta^2}{2\gamma_0^2} + (k_0 - h(1+\delta))x + \frac{k_0 h x^2}{2} \tag{2.81}$$

In Eq. (2.81), if $k_0 = 0$, then the Hamiltonian is reduced to be the same as the drift case as Eq. (2.60). The linear term of x describes a deflection by the magnetic field which is expected from a dipole. Usually the referential orbit is chosen to have $k_0 = h$, thus this linear term indicates that particle with a momentum deviation $\delta \neq 0$ is deflected differently and thus follows different trajectory. This effect is called dispersion. The second order term of x looks like the Hamiltonian for an oscillator. This focus effect provided by the dipole is often referred to as weak focusing. There are dipole magnets which also provide strong focusing with quadrupole effects by changing the shape of the pole faces. This kind of dipole is called combined function type and the KEK-DA ring mainly consists of eight combined function type magnets.

For combined function type dipole magnets, the scaled magnetic field can be expressed as,

$$\mathbf{b} = (k_1 y, k_0 + k_1 x, 0) \tag{2.82}$$

where k_1 is the quadrupole component of the magnetic field. Similarly, the third component of the vector potential to the second order of x and y is,

$$a_s = -k_0 x + \frac{1}{2} k_0 h x - \frac{1}{2} k_1 (x^2 - y^2) + O(2) \tag{2.83}$$

Substitute this into Eq. (2.53) and drop the high order terms, the Hamiltonian for the combined function type dipole is,

$$H = \frac{p_x^2}{2} + \frac{p_y^2}{2} + \frac{\delta^2}{2\gamma_0^2} + (k_0 - h(1+\delta)) x + \frac{k_0 h x^2}{2} + \frac{k_1}{2} (x^2 - y^2) \tag{2.84}$$

Compared with Eq. (2.81), the only difference is the quadrupole component in x and y direction with the inversed sign to each other, which means that while the beam is focused in the $x-$ direction, it is defocused the beam the $y-$ direction, vice versa.

Applying the Hamiltonian equations of Eq. (2.51) and Eq. (2.52), the transfer matrix for the combined function type dipole is,

$$
\begin{pmatrix} x \\ p_x \\ y \\ p_y \\ c\Delta t \\ \beta_0 \delta \end{pmatrix}_{s2}
=
\begin{pmatrix}
c_x & s_x & 0 & 0 & 0 & \bar{h}\frac{1-c_x}{\omega_x^2} \\
-\omega_x^2 s_x & c_x & 0 & 0 & 0 & \bar{h}s_x \\
0 & 0 & c_y & s_y & 0 & 0 \\
0 & 0 & \omega_y^2 s_y & c_y & 0 & 0 \\
-\bar{h}s_x & -\bar{h}\frac{1-c_x}{\omega_x^2} & 0 & 0 & 1 & \frac{L}{\beta_0^2\gamma_0^2} - \bar{h}^2\frac{L-s_x}{\omega_x^2} \\
0 & 0 & 0 & 0 & 0 & 1
\end{pmatrix}
\begin{pmatrix} x \\ p_x \\ y \\ p_y \\ c\Delta t \\ \beta_0 \delta \end{pmatrix}_{s1}
\tag{2.85}
$$

where,

$$s_x = \frac{\sin(\omega_x L)}{\omega_x} \tag{2.86}$$

$$c_x = \cos(\omega_x L) \tag{2.87}$$

$$s_y = \frac{\sinh(\omega_y L)}{\omega_y} \tag{2.88}$$

$$c_y = \cosh(\omega_y L) \tag{2.89}$$

$$\bar{h} = \frac{h}{\beta_0} \tag{2.90}$$

$$\omega_x = \sqrt{hk_0 + k_1} \tag{2.91}$$

$$\omega_y = \sqrt{k_1} \tag{2.92}$$

In terms of $(\Delta s, \delta)$, this becomes,

$$
\begin{pmatrix} x \\ p_x \\ y \\ p_y \\ \Delta s \\ \delta \end{pmatrix}_{s2} = \begin{pmatrix} c_x & s_x & 0 & 0 & 0 & h\frac{1-c_x}{\omega_x^2} \\ -\omega_x^2 s_x & c_x & 0 & 0 & 0 & h s_x \\ 0 & 0 & c_y & s_y & 0 & 0 \\ 0 & 0 & \omega_y^2 s_y & c_y & 0 & 0 \\ -h s_x & -h\frac{1-c_x}{\omega_x^2} & 0 & 0 & 1 & \frac{L}{\gamma_0^2} - h^2\frac{L-s_x}{\omega_x^2} \\ 0 & 0 & 0 & 0 & 0 & 1 \end{pmatrix} \begin{pmatrix} x \\ p_x \\ y \\ p_y \\ \Delta s \\ \delta \end{pmatrix}_{s1}
\tag{2.93}
$$

Quadrupole

In the case of quadrupole magnet, the transfer matrix is simply given by setting $h \to 0$ in the case of combined function type magnet as in Eq. (2.85),

$$
\begin{pmatrix} x \\ p_x \\ y \\ p_y \\ c\Delta t \\ \beta_0 \delta \end{pmatrix}_{s2} = \begin{pmatrix} \cos(\omega L) & \frac{1}{\omega}\sin(\omega L) & 0 & 0 & 0 & 0 \\ -\omega\sin(\omega L) & \cos(\omega L) & 0 & 0 & 0 & 0 \\ 0 & 0 & \cosh(\omega L) & \frac{1}{\omega}\sinh(\omega L) & 0 & 0 \\ 0 & 0 & \omega\sinh(\omega L) & \cosh(\omega L) & 0 & 0 \\ 0 & 0 & 0 & 0 & 1 & \frac{L}{\beta_0^2\gamma_0^2} \\ 0 & 0 & 0 & 0 & 0 & 1 \end{pmatrix} \begin{pmatrix} x \\ p_x \\ y \\ p_y \\ c\Delta t \\ \beta_0 \delta \end{pmatrix}_{s1}
\tag{2.94}
$$

where,

$$
\omega = \sqrt{k_1}
\tag{2.95}
$$

It can be directly derived from Hamiltonian Eq. (2.53) again with $\mathbf{a} = \left(0, 0, -\frac{k_1}{2}(x^2 - y^2)\right)$ and $h = 0$. Also notice that the longitudinal terms are the same as the drift space. Therefore, in terms of $(\Delta s, \delta)$, Eq. (2.94) is explicitly written as,

$$
\begin{pmatrix} x \\ p_x \\ y \\ p_y \\ \Delta s \\ \delta \end{pmatrix}_{s2} = \begin{pmatrix} \cos(\omega L) & \frac{1}{\omega}\sin(\omega L) & 0 & 0 & 0 & 0 \\ -\omega\sin(\omega L) & \cos(\omega L) & 0 & 0 & 0 & 0 \\ 0 & 0 & \cosh(\omega L) & \frac{1}{\omega}\sinh(\omega L) & 0 & 0 \\ 0 & 0 & \omega\sinh(\omega L) & \cosh(\omega L) & 0 & 0 \\ 0 & 0 & 0 & 0 & 1 & \frac{L}{\gamma_0^2} \\ 0 & 0 & 0 & 0 & 0 & 1 \end{pmatrix} \begin{pmatrix} x \\ p_x \\ y \\ p_y \\ \Delta s \\ \delta \end{pmatrix}_{s1}
$$

$$(2.96)$$

Chromaticity

In Eq. (2.94), the transverse deflection does not depend on the longitudinal variables. In fact, the focusing strength depends on the particle energy as well, which is known as chromaticity effect. This can be seen by going back to the Hamiltonian Eq. (2.57) where no approximation is made for D. In the case of the quadrupole magnet, it is,

$$
H = \frac{p_x^2}{2D} + \frac{p_x^2}{2D} + \frac{\delta}{\beta_0} - D + \frac{k_1}{2}\left(x^2 - y^2\right) \tag{2.97}
$$

By solving it with Eq. (2.51) and Eq. (2.52) in the transverse direction and write it in the form of transfer matrix, the only difference from the Eq. (2.94) is that the ω term is replaced with $\sqrt{\frac{k_1}{\omega}}$, or,

$$
\begin{aligned}
\omega' &= \sqrt{\frac{k_1}{D}} \\
&= \sqrt{k_1\left(1 - \delta + \left(\frac{3}{2} - \frac{\beta_0^2}{2}\right)\delta^2 + O[\delta]^3\right)} \\
&\approx \sqrt{k_1(1 - \delta)}
\end{aligned} \tag{2.98}
$$

Compared with Eq. (2.95), we see that the simple way to include the chromaticity for a quadrupole magnet is multiplying the value k_1 by $(1 - \delta)$.

2.1.3 Courant-Snyder parameters and emittance

Until now the properties of the transfer matrix M have not been discussed. For all the transfer matrices in previous section, it consists of three group, corresponding to the three directions.

In the case of the uncoupled motion, which means there is no interaction between each direction, the horizontal (or vertical) 2×2 transfer matrix can be generally written as,

$$M = I \cos(\mu) + S \sin(\mu) \tag{2.99}$$

where I is the 2×2 identity matrix, μ is the phase advance and S is,

$$S = \begin{pmatrix} \alpha & \beta \\ -\gamma & -\alpha \end{pmatrix} \tag{2.100}$$

or explicitly,

$$M = \begin{pmatrix} \cos \mu + \alpha \sin \mu & \beta \sin \mu \\ -\gamma \sin \mu & \cos \mu - \alpha \sin \mu \end{pmatrix} \tag{2.101}$$

The quantities α, β, γ are called the Courant-Snyder parameters [10], also known as Twiss parameters [11]. β is also often called beta function. Their relationship between these parameters are,

$$\beta\gamma - \alpha^2 = 1 \tag{2.102}$$

$$\alpha = -\frac{1}{2}\frac{d\beta}{ds} \tag{2.103}$$

In a periodic beam line, for example in the ring where the beam travels through the same lattice repeatedly, for one period L, the periodic solution requires that,

$$M(s + L) = M(s) \tag{2.104}$$

for a stable motion, the condition is that the trace of the M is bounded,

$$tr(M) = 2 \cos \mu \tag{2.105}$$

Eq. (2.105) is often used to calculate the phase advance of a periodic lattice and in case of a ring, the tune for an accelerator is defined as,

$$\nu = \frac{\mu}{2\pi} \tag{2.106}$$

The Courant-Snyder parameters forms a phase space ellipse which can be expressed in the equation,

$$\varepsilon = \gamma x^2 + 2\alpha x p_x + \beta p_x^2 \tag{2.107}$$

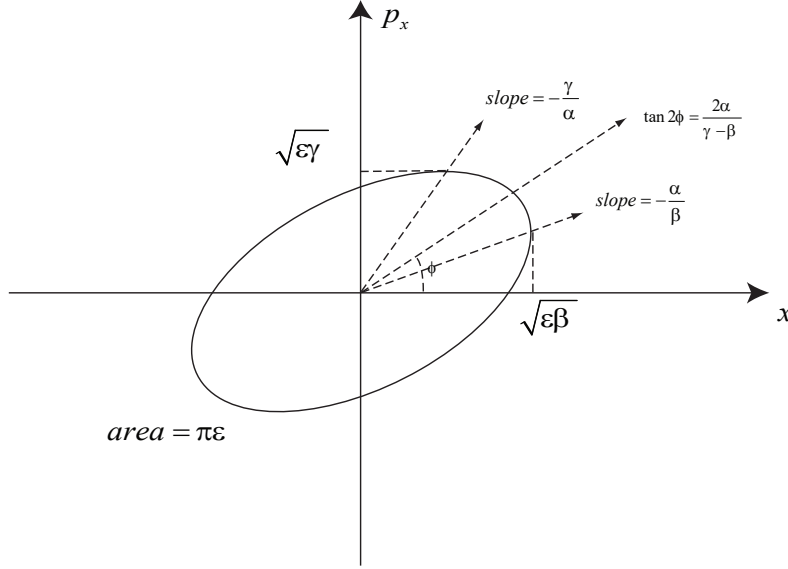where ε is the emittance. Eq. (2.107) can be plotted in Fig. 2.2. Particle that follows

Figure 2.2: Phase space formed by Courant-Snyder paramters.

Eq. (2.107) circulates around the space as shown in Fig. 2.2, with the largest excursion as $\sqrt{\varepsilon\beta}$. For a group of particles in a beam bunch, the area of the largest ellipse is called the emittance of the beam.

As the phase space which can be described with the beam emittance and the Courant-Snyder parameters is so important in the discussion of beam dynamics, the transport of the Courant-Snyder parameters is also helpful. All the transfer matrices are used to transport the particle coordinates. For example, assuming coordinates are transported from $s1$ to $s2$ as,

$$
\begin{pmatrix} x \\ p_x \end{pmatrix}_{s2} = \begin{pmatrix} a_{11} & a_{12} \\ a_{21} & a_{22} \end{pmatrix} \begin{pmatrix} x \\ p_x \end{pmatrix}_{s1}
\tag{2.108}
$$

and at the same time, the Courant-Snyder parameters are transported as,

$$
\begin{pmatrix} \beta \\ \alpha \\ \gamma \end{pmatrix}_{s2} = \begin{pmatrix} m_{11} & m_{12} & m_{13} \\ m_{21} & m_{22} & m_{23} \\ m_{31} & m_{32} & m_{33} \end{pmatrix} \begin{pmatrix} \beta \\ \alpha \\ \gamma \end{pmatrix}_{s1}
\tag{2.109}
$$

With the relationship in Eq. (2.107), the transfer matrix for Courant-Snyder parameters is solved to be,

23

$$\begin{pmatrix} m_{11} & m_{12} & m_{13} \\ m_{21} & m_{22} & m_{23} \\ m_{31} & m_{32} & m_{33} \end{pmatrix} = \begin{pmatrix} a_{11}^2 & -2a_{11}a_{12} & a_{12}^2 \\ -a_{11}a_{21} & a_{11}a_{22} + a_{21}a_{12} & -a_{12}a_{22} \\ a_{21}^2 & -2a_{21}a_{22} & a_{22}^2 \end{pmatrix} \tag{2.110}$$

2.1.4 Equation of motion

Alternative approach for the description of the linear dynamics of a particle along the beam line in terms of Courant-Snyder parameters is through Hill's equation. In fact, in Eq. (2.52), for the paraxial approximation(small angle approximation), $p_x \approx x'$, Eq. (2.52) can be written as,

$$x'' = -\frac{\partial H}{\partial x} \tag{2.111}$$

For example, in the case of a drift space, with Hamiltonian in Eq. (2.60), the equation of motion is,

$$x'' = 0 \tag{2.112}$$

In the case of a quadrupole magnetic field, with Eq. (2.97),

$$x'' = -k_1 x \tag{2.113}$$

where k_1 is,

$$k_1 = \frac{q}{P_0} \frac{\partial B_y}{\partial x} \tag{2.114}$$

Eq. (2.112) and Eq. (2.113) are similar to the equation for simple harmonic motion, thus the general solution can be written as,

$$x = \sqrt{\varepsilon\beta} \cos \phi \tag{2.115}$$

where the ε is the emittance and β is the beta function in Courant-Snyder parameters. Eq. (2.115) also indicate that the largest excursion is $\sqrt{\varepsilon\beta}$ and the particle oscillates with a phase angle ϕ. This is exactly the same motion in the phase space as shown in Fig. 2.2. From Eq. (2.112) to Eq. (2.113), the formation of Hill's equation provides a simple method to include the effect of external electromagnetic field on the particle motion, by simply adding corresponded terms to its right.

2.1.5 Transverse-Longitudinal coupled motion

Dispersive system

In case of uncoupled motion, the motion in each direction does not depend on the motions in other directions. However, as shown in Eq. (2.93), in the case of dipole magnet, the horizontal motion depends on the longitudinal coordinate, explicitly,

$$
\begin{pmatrix} x \\ x' \\ \delta \end{pmatrix}_{s2} = \begin{pmatrix} a_{11} & a_{12} & D \\ a_{21} & a_{22} & D' \\ 0 & 0 & 1 \end{pmatrix} \begin{pmatrix} x \\ x' \\ \delta \end{pmatrix}_{s1}
\tag{2.116}
$$

where D is called dispersion function, and from Eq. (2.93),

$$
D = h \frac{1 - c_x}{\omega_x^2}
\tag{2.117}
$$

$$
D' = h s_x
\tag{2.118}
$$

or,

$$
x = a_{11}x + a_{12}x' + D\delta = x_\beta + D\delta
\tag{2.119}
$$

in which the betatron oscillation described by Eq. (2.115) is noted as x_β to distinguish it from the total excursion noted as x. Eq. (2.119) indicates that the motion including the coupling term from the longitudinal momentum deviation can be simply realized by adding a linear term. The coupling between the transverse and longitudinal direction is also called synchro-beta coupling.

Momentum compaction and phase slip

As indicated by Eq. (2.119), particle with different momentum follows different trajectory along the beamline. If we consider a beamline with a total length of C_0, a referential particle with no momentum deviation ($\delta = 0$) and $x_\beta = 0$ will travel a distance C_0. In order to calculate how long the particle with the momentum deviation δ will travel, we suppose the travel length is dC corresponding to a small ds along the trajectory, as shown in Fig. 2.3. Then we have,

$$
dC = (\rho + x)d\theta = (\rho + x)\frac{ds}{\rho}
\tag{2.120}
$$

The total path length traveled by a particle along C_0 is,

$$
C = \int_0^{C_0} (1 + \frac{x}{\rho})ds = C_0 + \int_0^{C_0} \frac{x}{\rho}ds
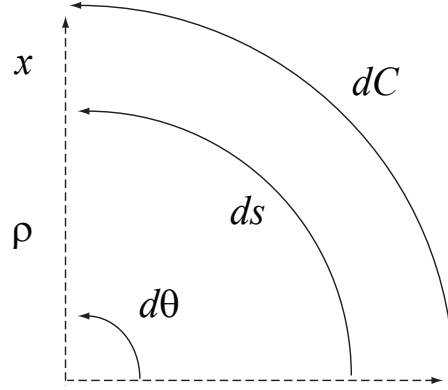\tag{2.121}
$$

Figure 2.3: Particle trajectory with momentum deviation.

Note that the excursion now comes from only dispersion and is described in Eq. (2.119), $x = D\delta$, the difference of the distance is then,

$$dC = C - C_0 = \delta \int_0^{C_0} \frac{D}{\rho} ds \qquad (2.122)$$

The momentum compaction factor α_c is defined as,

$$\alpha_c = \frac{1}{C} \frac{dC}{d\delta}\bigg|_{\delta=0} = \frac{1}{C_0} \int_0^{C_0} \frac{D}{\rho} ds \qquad (2.123)$$

The momentum compaction factor describes the difference of the travel distance due to the momentum deviation. Its definition in Eq. (2.123) also indicates that the drift space and the quadrupole where $\rho \rightarrow$ inf have no contribution.

Correspondingly, the phase slip factor η, which is used to describes the difference of time of flight due to the momentum deviation, is defined as by analogy with the momentum compaction factor,

$$\eta = \frac{1}{T} \frac{dT}{d\delta}\bigg|_{\delta=0} \qquad (2.124)$$

where T is the time required for an referential particle travels to C. Thus,

$$T = \frac{C}{\beta c} \qquad (2.125)$$

Then,

$$\frac{dT}{d\delta} = \frac{1}{\beta c}\frac{dT}{d\delta} - C\frac{d(\beta c)}{d\delta} \tag{2.126}$$

Given that by definition, the momentum deviation is $\delta = \frac{P-P_0}{P_0}$, thus,

$$P = (1 + \delta)P_0 \tag{2.127}$$

namely,

$$\gamma\beta = (1 + \delta)\gamma_0\beta_0 \tag{2.128}$$

therefore,

$$\frac{d(\gamma\beta)}{d\delta} = \gamma\frac{d\beta}{d\delta} + \beta\frac{d\gamma}{d\delta} \tag{2.129}$$

$$= \gamma^3\frac{d\beta}{d\delta} \tag{2.130}$$

$$= \gamma_0\beta_0 \tag{2.131}$$

Substitute Eq. (2.129) and Eq. (2.126) into Eq. (2.124) and evaluate at $\delta = 0$,

$$\eta = \alpha_c - \frac{1}{\gamma_0^2} \tag{2.132}$$

When particle at an energy that slippage factor $\eta = 0$, the time of flight will never depend on the momentum deviation. This energy is called transition energy and defined as,

$$\gamma_T = \frac{1}{\sqrt{\alpha_c}} \tag{2.133}$$

2.2 Longitudinal motion of an induction synchrotron

Even though the longitudinal variables have been included in the discussion in previous section, the transfer matrices derived for different kinds of magnet describe only the evolution of the dynamical variables along the beam line. The most important factor, acceleration, has not been discussed yet. In this section, the longitudinal motion of an induction synchrotron will be described. For better understanding of the uniqueness of the induction synchrotron, the longitudinal motion of the RF synchrotron is briefly reviewed here.

2.2.1 RF synchrotron and phase stability

Acceleration equation and longitudinal motion

In the RF synchrotron, the accelerating voltage excited in resonant cavities can be expressed by a sinusoidal waveform(Fig. 2.4),

$$V(\phi) = V_{RF} \sin \phi \tag{2.134}$$

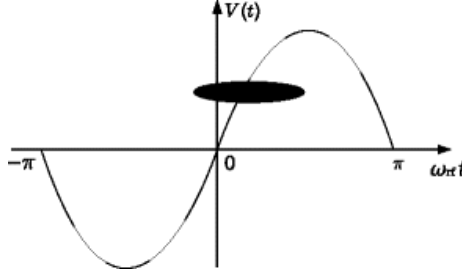where $\phi = \omega_{RF} t$, ω_{RF} is angular frequency for RF cavity.

Figure 2.4: RF voltage used to accelerate particle beam.

Because the magnetic field is ramping, the beam must be accelerated in order to stay on the referential orbit. A synchronous particle is assumed to be in the center of the bunch and gets accelerated by the RF voltage by $V_{RF} = \sin \phi^s$ every time when it passes through the RF cavity in order to stay on the referential orbit. This phase is called synchronous phase, ϕ^s . Fig. 2.5 can help to derive the longitudinal equations of motion for RF synchrotron.

The equations of motion describing the energy and phase difference with respect to the synchronous particle are,

$$(\Delta E)_{n+1} = (\Delta E)_n + Q e V_{RF} (\sin \phi_n - \sin \phi_n^s) \tag{2.135}$$

$$(\Delta \phi)_{n+1} = (\Delta \phi)_n + \frac{2\pi h \eta_{n+1}}{(\beta^s)^2} \frac{(\Delta E)_{n+1}}{E^s} + \Delta \phi_{RF,n+1} \tag{2.136}$$

In the above equations, n is the turn number; Q is the charge state; $\Delta E = E - E^s$, is the energy deviation from the synchronous particle; $\Delta \phi = \phi - \phi^s$, is the phase difference from the synchronous particle; $\eta = \frac{1}{\gamma_t^2} - \frac{1}{\gamma_s^2}$ is slippage factor defined in Eq. (2.132)(γ_s is relativistic factor for synchronous particle and γ_t is transition gamma, respectively); $\Delta \phi_{RF,n+1}$ is phase shift which is usually needed at transition crossing. The first equation describes the energy difference for a particle with respect
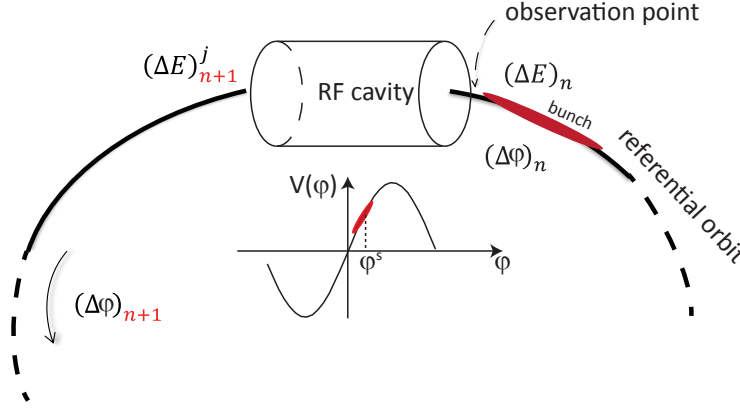
28

Figure 2.5: Bunch gets accelerated by RF cavity, ϕ^s indicating the position for synchronous particle at bunch center.

to synchronous particle due to different acceleration phase. This equation is justified when the length of RF cavity is rather small compared with the circumference of the RF synchrotron. Therefore, energy change ΔE happens locally and almost instantly. The second equation describes the relative position inside a beam for a specific particle. As shown in Fig. 2.5, this phase change relies on the particle information after the cavity.

Phase stability

As seen in Fig. 2.4, on the rising edge of the RF voltage, those particle ahead of the synchronous phase, ϕ^s will get less acceleration energy and they will arrive later for the next turn; meanwhile, those particles after the ϕ^s will get more acceleration energy will arrive faster for the next turn. In other word, particles will oscillate around the synchronous phase. This phenomenon is called longitudinal oscillation or synchrotron oscillation and this characteristics of RF synchrotron is called "phase stability". When the beam's energy surpasses transition energy($\gamma_t mc^2$), particle's relativistic mass comes into such a role that particles with higher energy will follow a larger orbit then arrive later for the next turn. To keep them along with the synchronous particle(assumed as the bunch center), they should get more energy to travel faster. Particles with less energy will follow a shorter distance then arrives faster for the next turn, thus they should get less energy to slow them down. In conclusion, under transition energy, ϕ^s should fall on the rise edge of the RF voltage

while above the transition energy, ϕ^s should fall on the fall edge of the RF voltage.

Under the condition that ϕ is close to ϕ^s (namely $\Delta\phi = \phi - \phi^s$ is a small value), Eq. (2.135) and Eq. (2.136) can be written into continuous form,

$$\frac{dW}{dt} = \frac{QeV_{RF}}{2\pi h}(\sin\phi - \sin\phi^s) \simeq \frac{QeV_{RF}\cos\phi^s}{2\pi h}\Delta\phi \qquad (2.137)$$

$$\frac{d\Delta\phi}{dt} = \frac{\omega_{RF}^2\eta}{(\beta^s)^2}W \qquad (2.138)$$

where $W = \frac{\Delta E}{\omega_{RF}}$. These two equations can be derived from Hamiltonian,

$$H(\phi, W; t) = \frac{\omega_{RF}^2\eta}{2(\beta^s)^2 E^s}W^2 + \frac{ZeV_{RF}}{2\pi h}[\cos\phi - \cos\phi^s + (\phi - \phi^s)\sin\phi^s] \qquad (2.139)$$

Fig. 2.6 shows a typical contour plot for Eq. (2.139)($\frac{\Delta p}{p} = \frac{1}{\beta^2}\frac{\Delta E}{E}$). A notable feature for this contour plot is that it shows a "bucket" inside which particles do synchrotron oscillation. This bucket size determines the longitudinal maximum emittance reserved for the beam.
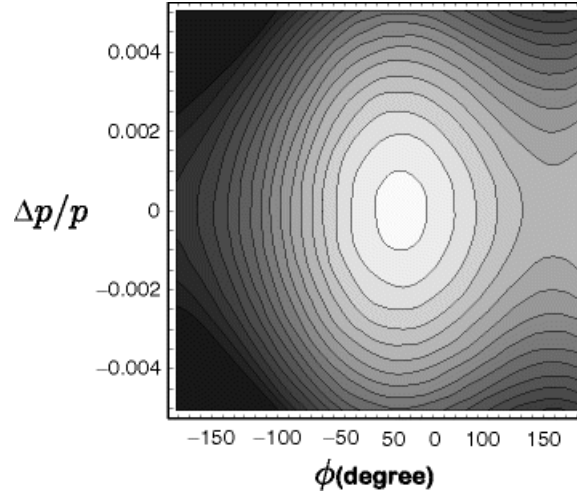

Figure 2.6: Typical Hamiltonian contour of RF Synchrotron in phase space.

2.2.2 Induction synchrotron: barrier buckets confinement and acceleration

Unlike RF synchrotron where the sinusoidal voltage plays the role of both acceleration and longitudinal confinement, induction synchrotron, by employing induction

cells instead of RF cavities, provides the acceleration and longitudinal confinement separately for the beam.
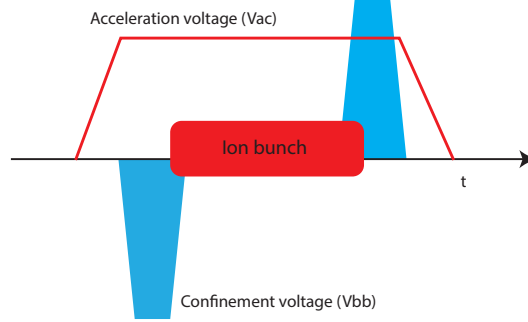

Figure 2.7: Acceleration voltage and confinement voltage are separately provided in induction synchrotron.

In Fig. 2.7 the longer pulse voltage is used for acceleration (Vac) and the other two short pulse voltages (barrier bucket voltage, Vbb) are used to confine the beam longitudinally. The equations of motion for induction synchrotron are similar to Eq. (2.140) and Eq. (2.141) with the different forms of the pulse voltage. The equations of longitudinal motion for induction synchrotron are,

$$(\Delta E)_{n+1} = (\Delta E)_n + Qe[V(\phi_n) - V_n^s] \tag{2.140}$$

$$(\Delta \phi)_{n+1} = (\Delta \phi)_n + \frac{2\pi \eta_{n+1}}{(\beta^s)^2 E^s} \frac{(\Delta E)_{n+1}}{E^s} \tag{2.141}$$

where $V(\phi)$ is the pulse profile as shown in Fig. 2.7. In Eq. (2.140) $V(\phi)$ at some phase position should be the net voltage of the acceleration voltage and barrier bucket voltage. V_n^s is the voltage felt by synchronous particle when the beam passes through the induction cells.

In a continuous form, Eq. (2.140) and Eq. (2.141) are,

$$\frac{dW}{dt} = \frac{Qe}{2\pi}(V(\phi) - Vac) \tag{2.142}$$

$$\frac{d\Delta\phi}{dt} = \frac{\omega_0^2 \eta}{(\beta^s)^2 E^s} W \tag{2.143}$$

31

where $W = \frac{\Delta E}{\omega_0}$. Similarly, these two equations can be derived from Hamiltonian,

$$H(\phi, W; t) = \frac{\omega_{RF}^2 \eta}{2(\beta^s)^2 E^s} W^2 - \frac{Ze}{2\pi} \int^{\phi} [V(\phi)' - Vac] d\phi' \tag{2.144}$$

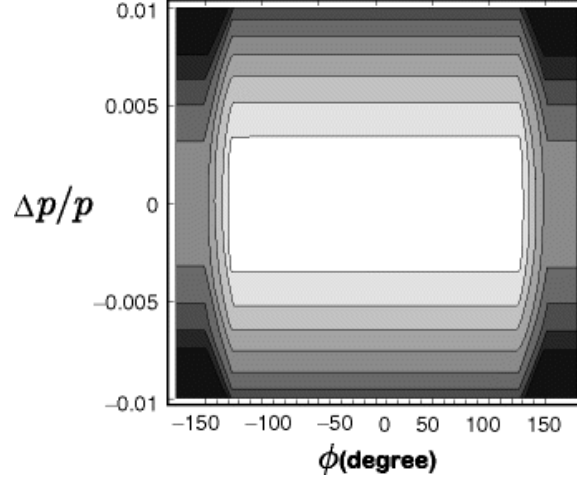Fig. 2.8 shows a typical contour plot for this Hamiltonian.

Figure 2.8: Typical Hamiltonian contours of induction synchrotron in phase space.

2.3 Acceleration consideration

2.3.1 Required acceleration voltage

To keep the particle synchronized with the ramping magnetic field, the required acceleration voltage for each turn inside the ring can be obtained by starting from the Lorentz Law which states,

$$\frac{\gamma A m v^2}{\rho} = QevB \tag{2.145}$$

where A is the mass number of the particle and m is the proton mass, ρ is the bending radius of the orbit, Q is the charge states, e is the electron charge state, e is the electron charge, v is the speed of the particle and B is the magnetic flux intensity.

With$\beta = vc$ where c is the light velocity,

$$\frac{\gamma A m \beta c}{\rho} = QeB \tag{2.146}$$

Taking the derivative of time on both sides of Eq. (2.146),

$$\frac{Amc}{\rho}\frac{d(\gamma\beta)}{dt} = Qe\frac{dB(t)}{dt} \qquad (2.147)$$

In addition,

$$\gamma\beta = \sqrt{\gamma^2 - 1} \qquad (2.148)$$

taking the time derivative on both sides,

$$\frac{d(\gamma\beta)}{dt} = \frac{1}{\beta}\frac{d\gamma}{dt} \qquad (2.149)$$

Also notice that,

$$E = \gamma Amc^2 \qquad (2.150)$$

thus in fact,

$$\frac{dE}{dt} = Amc^2\frac{d\gamma}{dt} \qquad (2.151)$$

Combining Eqs (2.147), (2.149) and (2.151), the result is,

$$\frac{dE}{dt} = \frac{\rho Qe}{\beta c}\frac{dB(t)}{dt} \qquad (2.152)$$

Considering the particle travel in a ring with the circumference is C_0, the energy change by the acceleration voltage should be,

$$\frac{dE}{dt} \approx \frac{\Delta E}{\Delta T} = Qe\frac{V_{acc}}{T} = Qe\frac{V_{acc}}{C_0/\beta c} \qquad (2.153)$$

Now the required acceleration voltage in terms of the ramping magnetic field is obtained as,

$$V_{acc} = C_0\rho\frac{dB(t)}{dt} \qquad (2.154)$$

for a ramping magnetic defined as,

$$B(t) = \frac{1}{2}(B_{\min} + B_{\max}) - \frac{1}{2}(B_{\max} - B_{\min})\cos\omega t \qquad (2.155)$$

With Eq. (2.154),the required voltage is then,

$$V_{required} = C_0\rho\frac{(B_{\max} - B_{\min})}{2}\omega\sin\omega t \qquad (2.156)$$

2.3.2 Pulse density control scheme

From Eq. (2.156) one see that the required voltage is gradually changing to accommodate the ramping magnetic field. In the KEK-DA system, the magnetic field is ramped at a frequency of 10 Hz. in the case of maximum magnetic field 0.3 T, the required voltage and the revolution period are shown in Fig. 2.9 and Fig. 2.10, respectively.
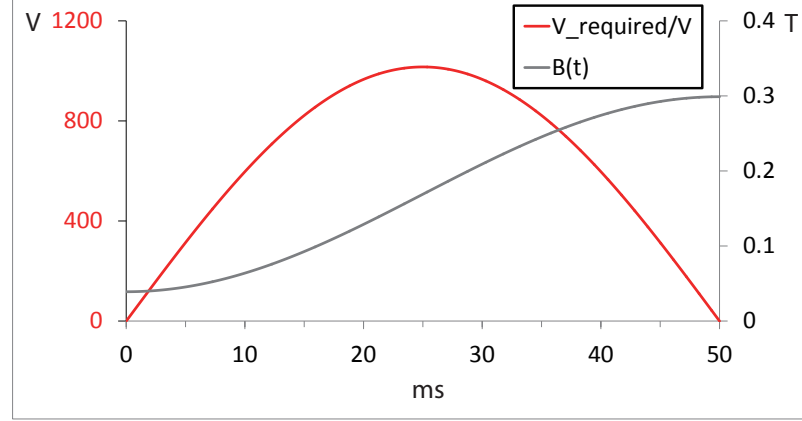

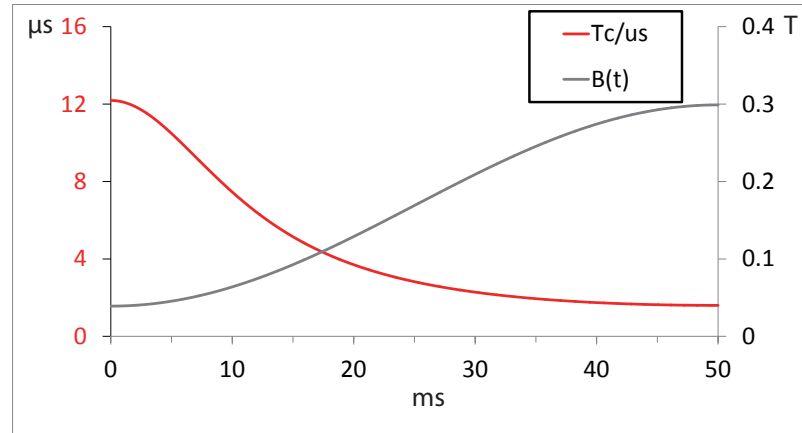Figure 2.9: Required voltage with ramping magnetic field.

Figure 2.10: Revolution period with ramping magnetic field.

However, for the present Switching Power Supply (SPS) system which will be described in Sec. 3.6.2, the output pulse voltage is predefined by the DC power supply,

34

which is set to be a specific value but can not be changed within an acceleration cycle. Thus a scheme called "pulse density control" was proposed in [12]. The basic idea is to wait for the integrated required voltage to achieve the set output voltage. As seen in Fig. 2.9, the required voltage at the beginning is very small, while in the middle of the acceleration when the ramping field changes almost linearly in time, the required voltage comes to the maximum. As a result, the pulse density profile which is realized in the pulse density control scheme, becomes as shown in Fig. 2.11.
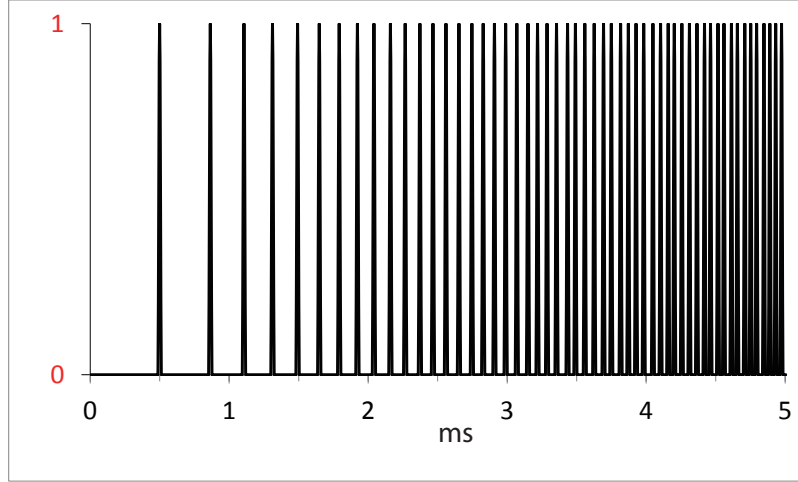
Figure 2.11: Pulse density control scheme.

As can be expected, with the pulse density control, the beam deviates from the referential particle when it gets no acceleration voltage. In a dispersive system, this will caused synchro-beta coupling as indicated in Eq. (2.93) and Eq. (2.119).

2.4 Summary

In this chapter, the fundamental beam dynamics related to an induction synchrotron has been reviewed.

From the Hamiltonian for a particle in an external electromagnetic fields, the transfer matrix for the drift space, the dipole magnet (including the combined function) and the quadrupole magnet have been deduced. These transfer matrices deduced in Sec. 2.1.2 have been given in the six dimensional phase space. They were directly used in the 3D particle tracking code developed for the induction synchrotron (Chapter 6) for the beam evolution. Generally speaking, these knowledge and formations are the

35

same as an conventional synchrotron in a storage ring where no acceleration of the beam is applied.

The uniqueness of an induction synchrotron lies in the longitudinal motion discussed in Sec. 2.2 as it utilizes the induction pulses to confine the beam longitudinally and accelerate the beam. This uniqueness leads to much more flexible beam manipulation in the longitudinal phase space, but it also raises the questions of the beam behavior under different settings of the induction pulses. Therefore, in order to be able to study the beam motion in such an accelerator, we have chosen to develop a specific code instead of adopting existing codes which are not designed for the induction synchrotron.

Besides, the beam dynamics in this chapter also provides the necessary theoretical tools for the experimental studies in the LEBT line as discussed in Chapter 5,

1). The transport of Courant-Snyder parameters along a beam line in Sec. 2.1.3 is used to measure these parameters with profile monitors;

2). The dispersion function in Sec. 2.1.5 is used to measure the longitudinal momentum deviation within a beam pulse.

Chapter 3

KEK Digital Accelerator

In the Introduction of this thesis, it was mentioned that the KEK-DA was built as a demonstration of slow cycling induction synchrotron. In addiction, we went through the theoretical basics of such a machine in previous chapter. Before the discussion of the experimental studies and simulation works on such a machine in the following chapters, we provide an overall description of the KEK-DA here. The relationship between each sub-system and the thesis study will also be clarified in this chapter.

3.1 Layout

As a complete demonstration project of the induction synchrotron concept, the KEK-DA has been built as compact as possible. A schematic view of this facility is shown in Fig. 3.1.

A permanent magnet Electron Cyclotron Resonance Ion Source (ECRIS) embedded in a 200 kV High Voltage Platform (HVT) has been used to generate the heavy ion beam. After transported through the Low Energy Beam Transport (LEBT) line, the beam will be injected into the KEK-DA ring with an electrostatic kicker. Two stacks of induction cells are installed in the S6 Section and S7 Section for the longitudinal confinement and acceleration, respectively. After being accelerated, the beam will be extracted with the extraction kickers installed at S2 Section and septum at S4 Section to the High Energy Beam Transport (HEBT) line.

These systems will be briefly introduced in this chapter with their present status and the latest development.
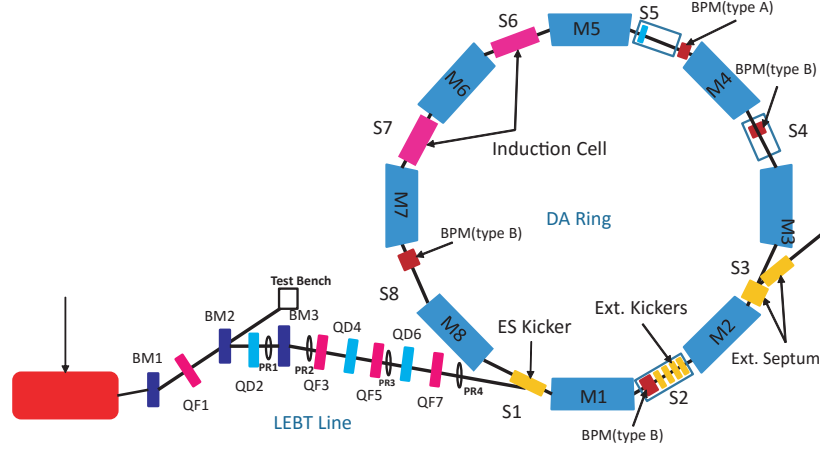
Figure 3.1: Schematic view of the KEK-DA

3.2 Ion Source

At the very upstream of the KEK-DA is the High voltage Platform (HVT) where an Electron Cyclotron Resonance(ECR) ion source (KEK-DA ECRIS) is installed inside. One of the feature of the induction synchrotron is the capability of accelerating all ion species, regardless of the mass-charge (A/Q) ratio. Therefore, an ECR ion source was chosen because it can provide various ion species by simply changing the seed gas. In addition, a specific charge state of the beam can be selected with a bending magnets.

A photo of the HVT with the ECRIS embedded inside is shown in Fig. 3.2.

3.2.1 High Voltage Terminal

A schematic view of the HVT layout is shown in Fig. 3.3.

Except for the ECRIS, the other subsystems such as the micro wave system, gas inlet, vacuum system and power supplies for all the devices are also embedded inside the HVT.

The beam comes from the ECRIS will leave the HVT through a post-acceleration column which is a ceramic chamber installed to insulate the high voltage of the platform and the LEBT line.
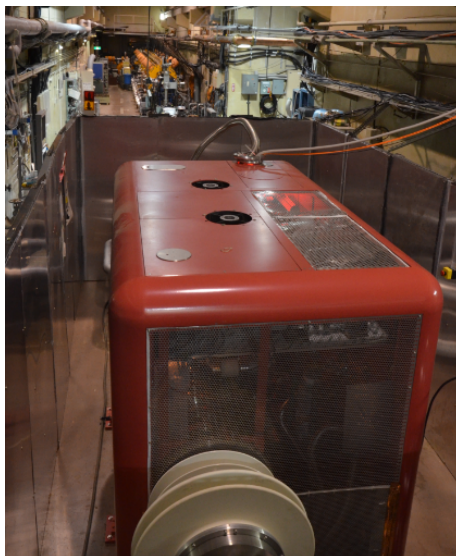
Figure 3.2: 200 kV high voltage platform with the ECRIS and Einzel lens chopper installed inside (view from downstream).
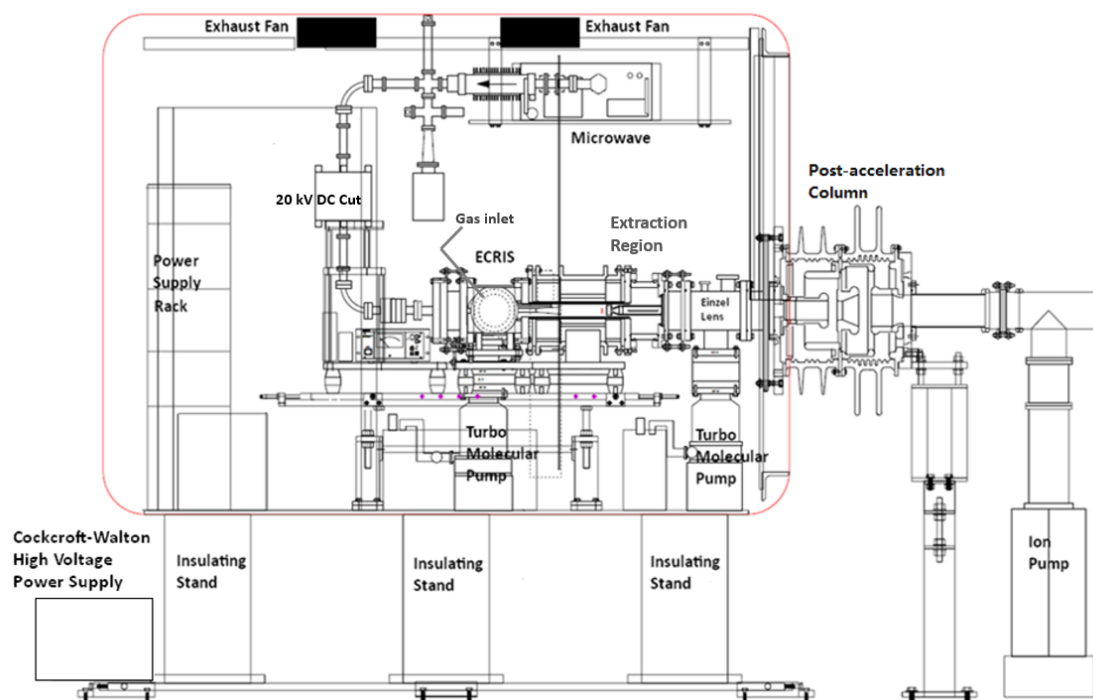

Figure 3.3: Layout of the High Voltage Terminal (HVT).

3.2.2 ECRIS

Electron Cyclotron Resonance Ion Sources (ECRIS) are commonly used to produce the multiply charged ion beams for heavy ion accelerators due to their easy maintenance. The main parameters of the KEK-DA ECRIS is listed in Table 3.1. More details of the ECRIS will be given in Chapter 4 where the production of ion beam is discussed.

Table 3.1: Typical parameters for the KEK-DA ECRIS.

f	$\sim 9.4\,\mathrm{GHz}$
plasma chamber diameter	$30\,\mathrm{mm}$
orifice diameter	$2\,\mathrm{mm}$

The core part of the ECR ion source of the KEK-DA is schematically illustrated in Fig. 3.4. The plasma is generated by the microwave heating and confined in the
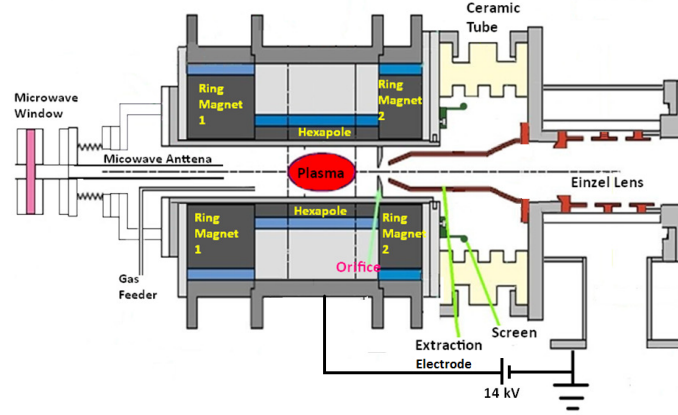
Figure 3.4: Schematic view of the ECR ion source for the KEK-DA.

plasma chamber by the mirror magnetic field. The ion beam is extracted through the orifice and transported to the downstream.

3.2.3 Einzel Lens Chopper

Einzel Lenses are usually used to focus the beam transversely. It consists of three electrodes. For the KEK-DA, it is also used as a longitudinal beam chopper by controlling the voltage on the middle electrode [13] using a solid state Marx pulse

generator. Thus it is referred as Einzel Lens Chopper here. A photo of the Einzel Lens installed right after the ECRIS is shown in Fig. 3.5 and Fig. 3.6.
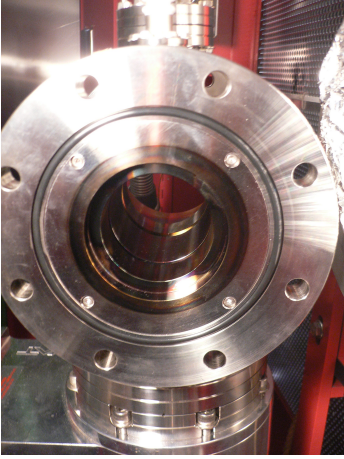

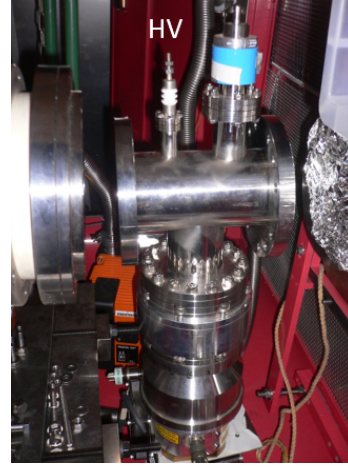Figure 3.5: Einzel Lens Chopper(inside).

Figure 3.6: Einzel Lens Chopper(side).

3.3 LEBT line

3.3.1 Layout

At the very beginning, the beam pass through a bending magnet (BM1) which is used to select the specified A/Q beam because the beam from the ECRIS usually contains particles with different charge state. Another bending magnet (BM2) is used to deflect the beam to the downstream or let it pass and reach the test bench. The third bending magnet (BM3) is used to tune the beam's orbit towards the ring.

There are seven quadrupole magnets in the LEBT line providing strong focusing to the beam. A picture of the LEBT region is shown in Fig. 3.7.

3.3.2 Diagnostics on LEBT

In the chamber located at the end of the test bench, a Faraday Cup (FC1) is used to test the beam intensity and a screen monitor with scintillating material can be used to measure the 2D beam profile. A pepper pot monitor can also replace the screen
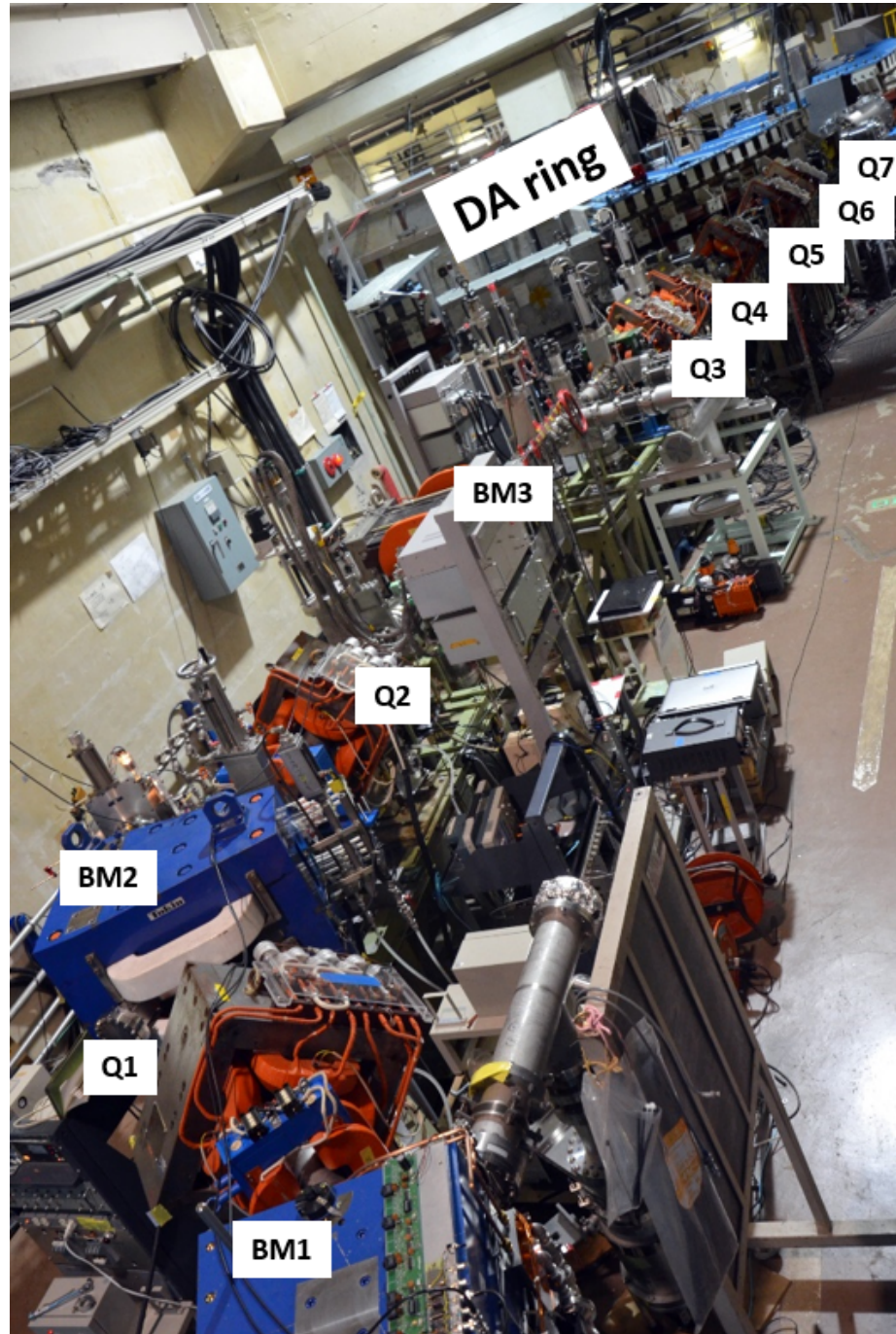
Figure 3.7: LEBT Region(view from upstream).

monitor for the emittance measurement. A second Faraday Cup (FC2) is installed after Q5 (Fig. 3.1).

Four multi-wire grid profile monitors are installed along the LEBT line to observe the horizontal or transverse beam profile. These diagnostic devices play key roles in the beam diagnostics in the LEBT line region.

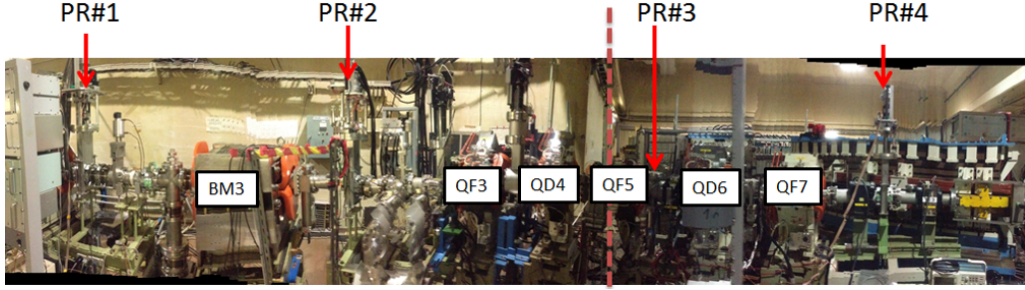Fig. 3.8 shows all the four profile monitors on the LEBT line.

Figure 3.8: Profile monitors on the LEBT line.

Fig. 3.9 shows the main body of the profile monitor (PR1 in this picture). A step motor drive is used to insert the head of the monitor into beam line. Fig. 3.10 shows the control system and the signal processing unit for the profile monitor.
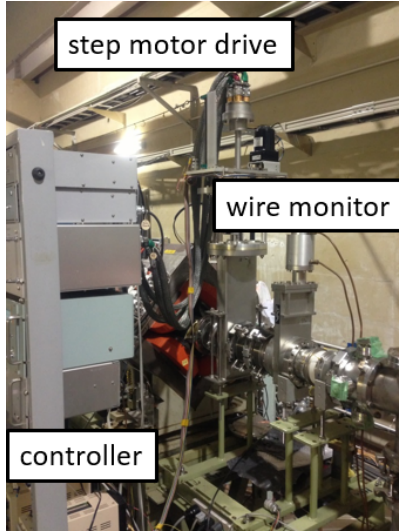

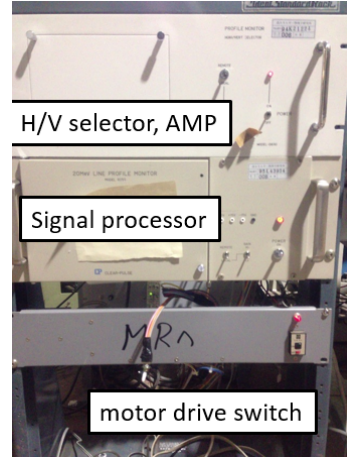Figure 3.9: The body of the profile monitor(PR1).

Figure 3.10: The control and signal processing unit of the profile monitor(PR1).

More discussion on the profile monitor is in Chapter 5 where they are extensively used for the beam studies in the LEBT region.

In 2014, in order to measure the quasi-3D profile of the beam, we modified the present profile monitor. This will also be discussed in Chapter 5.

3.4 Injection Kicker

After the LEBT line, the beam is injected into the KEK-DA main ring. To make the beam into the right orbit for the beam injection, an Electrostatic(ES) Kicker is installed at S1 Section (see Fig. 3.1) to kick the beam with horizontal electric fields. Fig. 3.11 shows a photograph of the ES Kicker and Fig. 3.12 shows a schematic view of how the beam is kicked by its electric field at injection. A detailed discussion on the ES Kicker for the KEK-DA can be seen in Ref. [14].
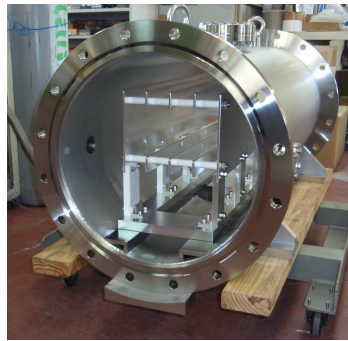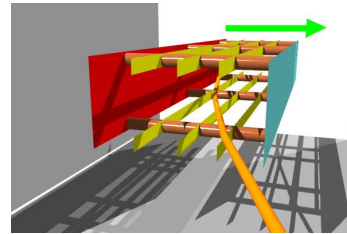

Figure 3.11: Photograph of the ES Kicker.

Figure 3.12: Schematic view the ES Kicker with electric field and the injection beam orbit.

After the beam enters into the ring, it circulates along the ring and returns to S1 Section. The high voltage on the ES Kicker has to be turned off to prevent it from kicking the beam again. Therefore, the maximum allowed beam length inside the ring has to be within the beam revolution time. This is why we need to chop the beam with the Einzel Lens Chopper. For He^{1+} with kinetic energy of $200\,\text{keV}$, $\beta \approx 0.01$. Given that the total length of the main ring of the KEK-DA is 37 m, the revolution time for the He^{1+} particle inside the ring just after injection is $\sim 12\,\mu\text{s}$. This demands that the drop edge must be very sharp. Fig. 3.13 shows the voltage profile on the high voltage electrode of the ES Kicker in actual operation.

At present, the high voltage used for the ES Kicker is $20\,\text{kV}$. Originally, this pulse was generated with Thyratron switch. A new compact SI-Thyristor Matrix Array
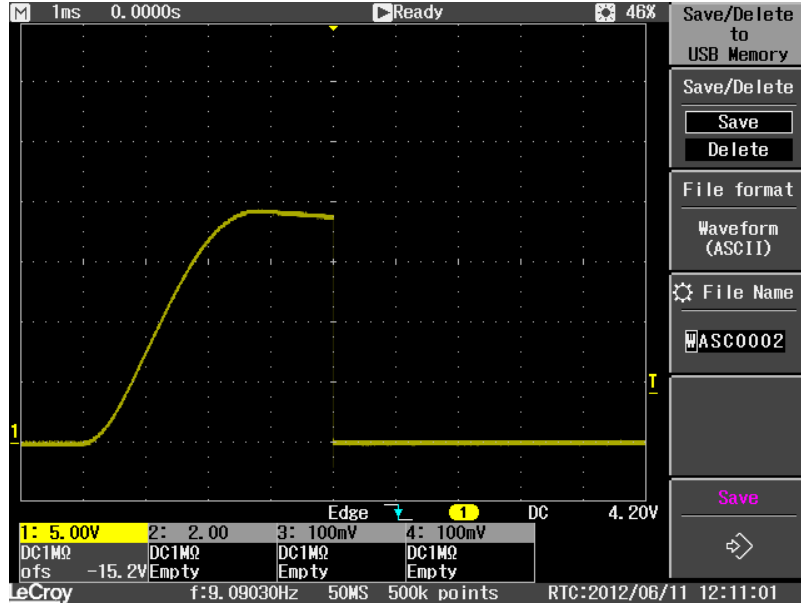
Figure 3.13: Voltage pulse on the ES Kicker high voltage electrode.

(SI-Thy MA) switch has been developed and successfully applied to the KEK-DA in 2014 [15]. The switch module of the SI-Thy MA is shown in Fig. 3.14.

The reflection pulses appeared in the old Thyratron switch as well as the present SI-Thy MA SW caused micro-bunch structure formation due to the longitudinal momentum modulation in the beam pulse. The simulation work including the longitudinal space charge force was carried out as described in [16].

3.5 Ring

The KEK-DA main ring consists of eight combined function magnets and eight straight sections where other equipment like the vacuum pump and diagnostic devices can be installed.

3.5.1 Combined function type magnet

Each combined function type magnet is a FDF type as shown in Fig. 3.16. The red color stands for the excitation coils. The right picture in Fig. 3.16 shows the pole shape in the F-section giving focusing effects for the horizontal direction on both sides
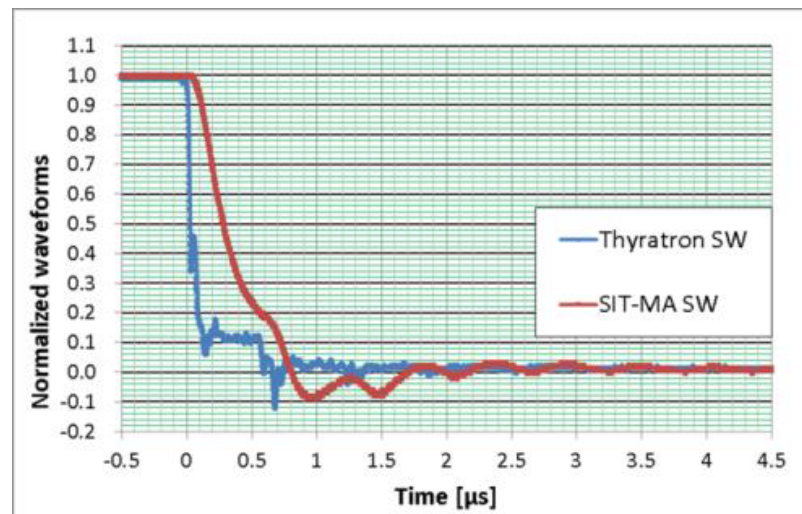
Figure 3.14: The SI-Thy MA SW.

Figure 3.15: Comparison of the Thyratron SW and the SI-Thy MA SW: reflection pulses after switching-off.

and D-section giving defocusing effects for the horizontal direction) in the middle. Fig. 3.17 is the photograph of one of the bending magnet in the main ring.
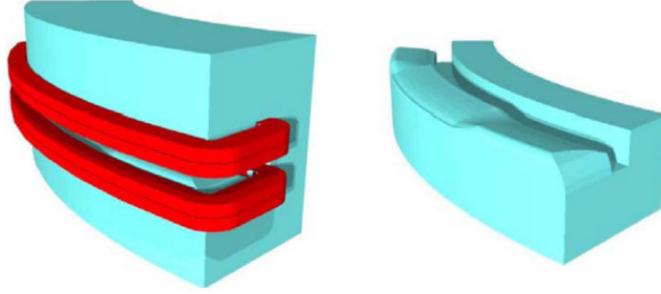

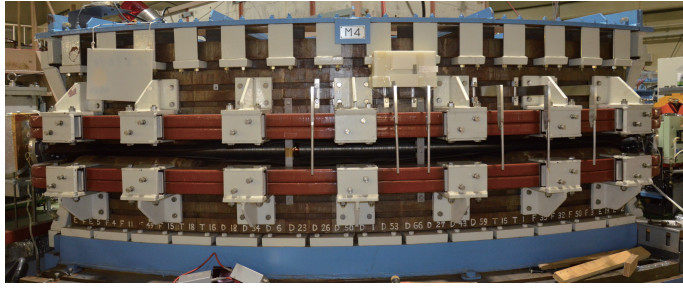Figure 3.16: Combined function magnet (FDF type).

Figure 3.17: Bending magnets of KEK-DA(BM4).

Table 3.2 shows some of the parameters of the bending magnet.

These magnets are labeled from M1 to M8 in Fig. 3.1. The lattice for the main ring is eight periods of FDFO. Fig. 3.18 shows the beta function and the dispersion function in such a FDFO period.

Table 3.3 shows other parameters of the main ring lattice.

3.5.2 Vacuum

In order to reduce the beam loss due to the beam particle's interaction with the residual gas, the vacuum condition in the ring should be increased. For this purpose, two extraction kicker originally located in S7 Section has been relocated to S2 Section. The old S8 Section has been replaced with a new thinner chamber.

47

Table 3.2: Parameters of the combined function type magnet KEK-DA ring.

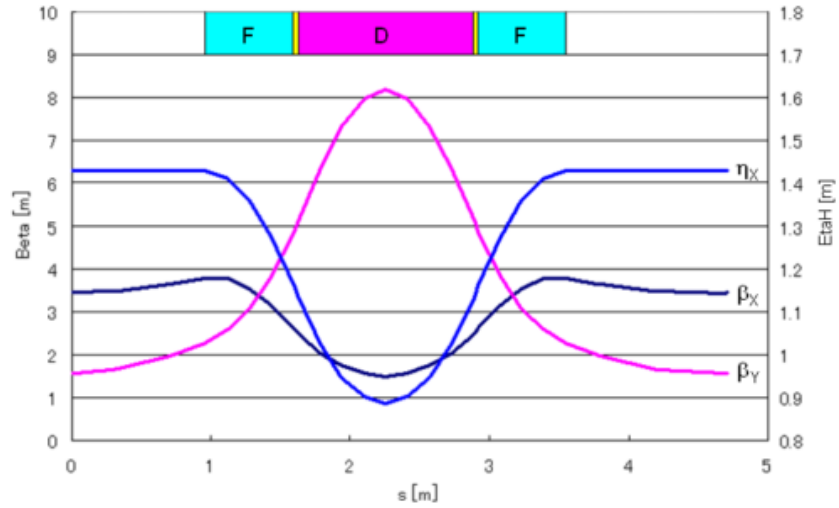|	
Thickness of steel sheets	0.35 mm
Gap height at pole center	75 mm
Pole width	300 mm
Number of turns (per pole)	20
B_{max} (present)	1.1 T (0.84 T)
Quadruple component B'/B(F/D)	3.664/-3.664 m^{-1}
Length of F section	0.6313 m
Length of D section	1.2588 m
Length of H section	0.0352 m

Figure 3.18: Beta function(x and y direction, left vertical axis) and dispersion function (x direction, right axis) for one period for the KEK-DA main ring.

Table 3.3: Parameters of main ring Lattice.

total length	37.7 m
Bending radius	6 m
Magnet length	2.5918 m
Drift length	2.1206 m
Q_x(injection)	2.17
Q_y(injection)	2.30
Chromaticity(X/Y)	-1.06/-5.73
γ_t	2.25

3.5.3 Diagnostics in the ring

There is an electrostatic bunch monitor installed in the middle of S5 Section for measuring turn-by-turn intensity profile of the beam. Besides, there are four beam position monitors installed at S2, S4, S5 and S8, as marked in Fig. 3.1. Fig. 3.19 and Fig. 3.20 show pictures of two types of beam position monitor used in the KEK-DA. In addition, a single screen monitor is set in S1 to observe the full profile in the transverse direction.
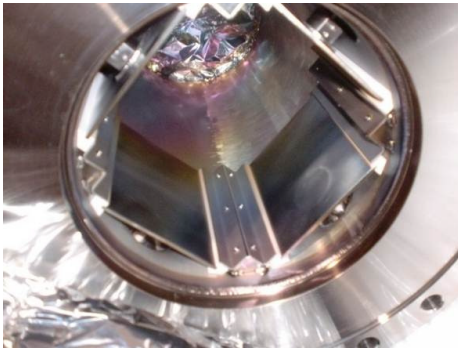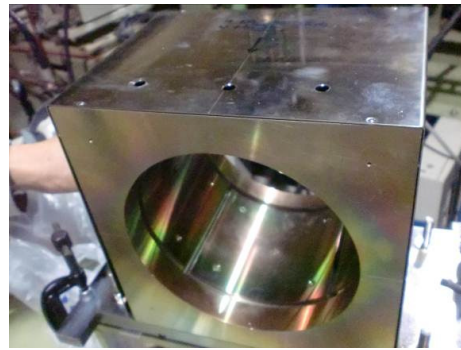

Figure 3.19: Beam position monitor, type A.

Figure 3.20: Beam position monitor, type B.

3.6 Induction cells and switching power supplies

3.6.1 Induction cells

The most important feature of induction synchrotron is that the acceleration and confinement of the beam are done by induction cells instead of RF cavities. The schematic view of the induction cells is shown in Fig. 3.21.
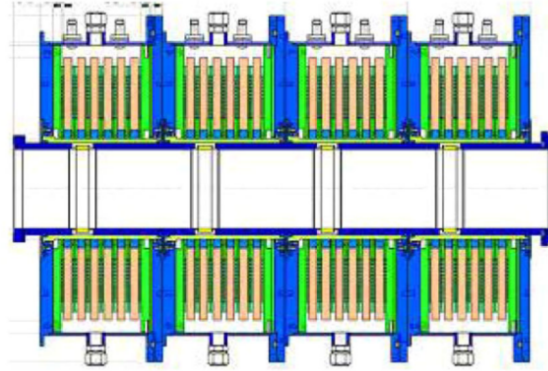

Figure 3.21: Schematic view of induction cells.

Fig. 3.22 shows three induction cells installed in S6 Section (Fig. 3.1). Fig. 3.23 shows six induction cells installed in S7 Section.

One of the characteristics of the induction cell is that it has to be reset before the magnetic material saturates. Fig. 3.24 shows when the ion beam bunch is passing through the induction cell, the polarity of the pulse voltage from the Switching Power Supply (SPS) is set for accelerating the beam. This is called *set state*. Fig. 3.25 shows that when the beam is not affected by the induction cell, the polarity is reversed to reset the magnetization. This time period is called *reset state*.

3.6.2 Switching power supplies

Above process implies that Switching Power Supply (SPS), which is powered by DC power supply, is a key device to realize set and reset voltages for induction cells. In Fig. 3.26, the 1st generation of SPS, which is still in use is shown at the down side. There are seven MOSFETs in each arm and one SPS has four arms (two in the picture and another two on the back in Fig. 3.26). The 2nd generation of SPS is also shown in Fig. 3.26 (on the top of 1st generation). The top view of the 2nd generation is shown in Fig. 3.27. From Fig. 3.26 and Fig. 3.27, one can see that the 2nd generation
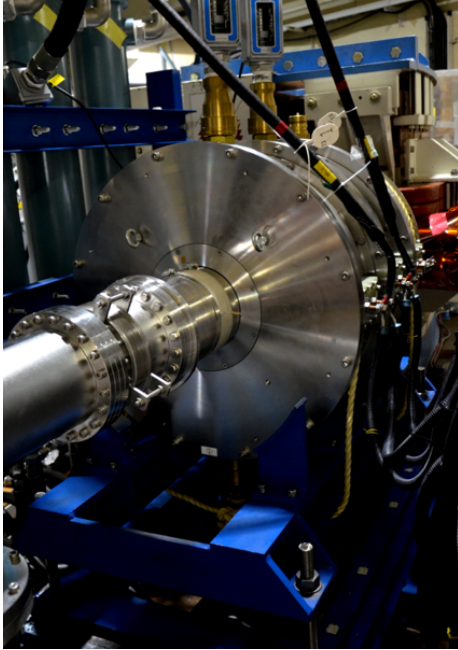
Figure 3.22: Induction cells in S6.
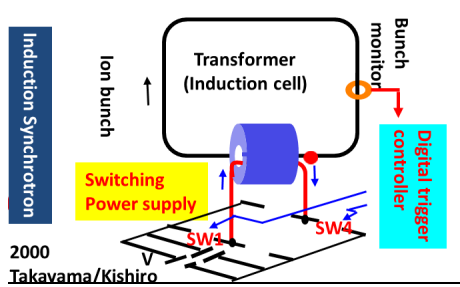

Figure 3.23: Induction cells in S7.
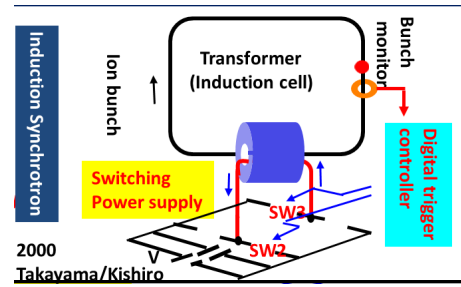

Figure 3.24: Set state.

Figure 3.25: Reset state.

SPS takes only 1/5 of the space as the 1st generation. The 2nd generation has been successfully tested with beam commissioning [17]. Fig. 3.28 is an equivalent circuit
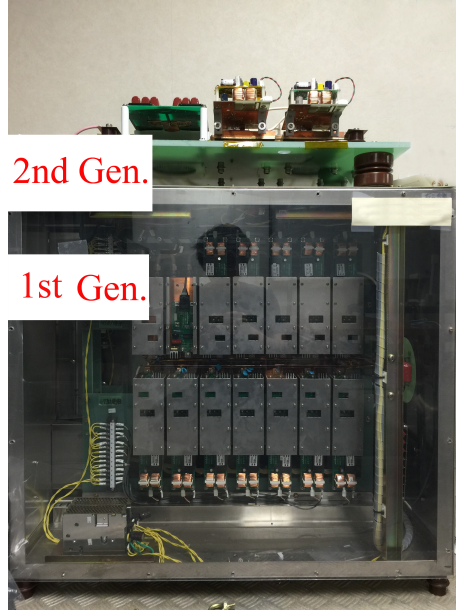

Figure 3.26: 1st and 2nd generations of Switching Power Supply for KEK-DA.

for the induction acceleration system which consists of DC power supply, SPS and induction cells. This figure also shows the relationship among the three.

3.7 Trigger control system

A trigger control system is necessary to organize each sub-system discussed above. The signal from the monitor is processed by a DSP and the FPGA system generates the trigger of the SPS according to the pre-defined pattern through out the acceleration period. Fig. 3.29 shows such a system used for the KEK-DA.

It is worth to summarize the solid state switch devices in the KEK-DA. From upstream, they are,

1). Solid state Marx generator for the Einzel Lens Chopper;

2). SI-Thy MA SW for the Injection Kicker;
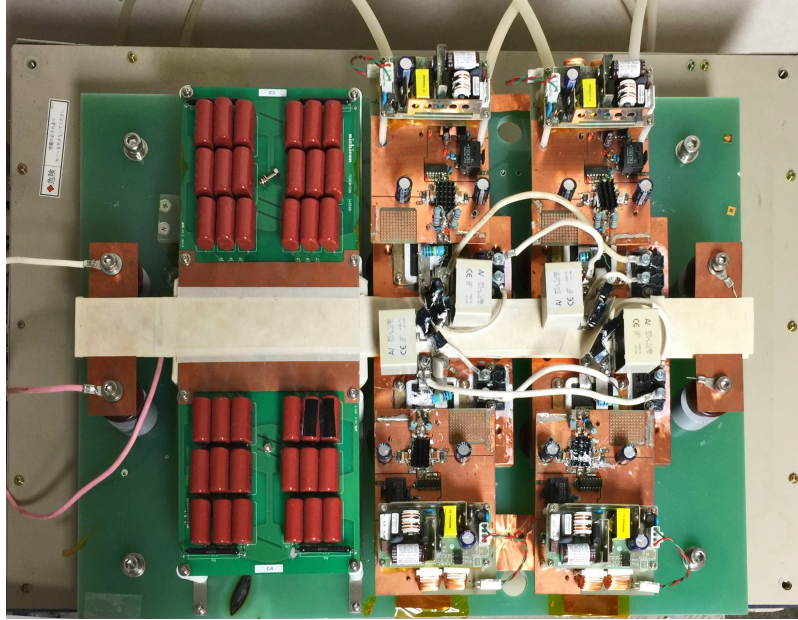
3). SPS to drive the induction cells.

Figure 3.27: Top view of the 2nd generation SPS.
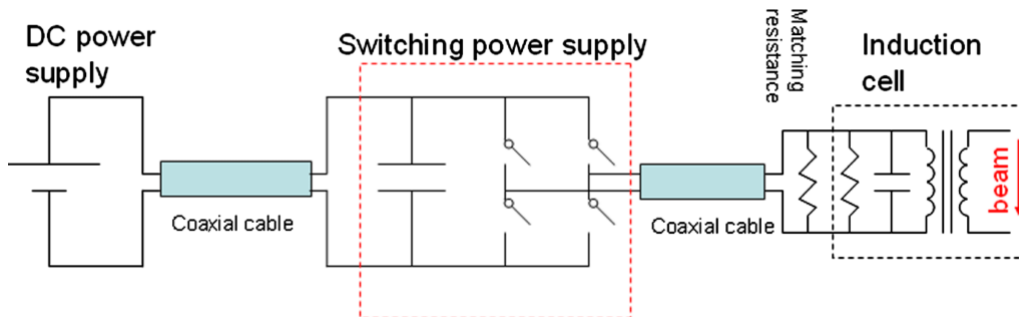
Figure 3.28: Equivalent circuit for the induction acceleration system.
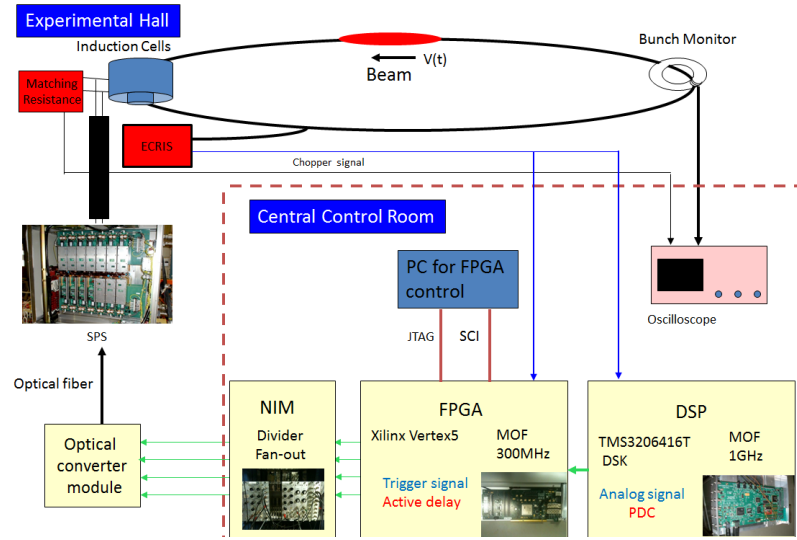
Figure 3.29: Trigger control system for the KEK-DA.

These devices are highly reliable and very small in size. Moreover, they can be easily controlled by digital signals from the FPGA and the PC in the trigger control system.

3.8 Summary

In this chapter, sub-systems of the KEK-DA have been introduced with the latest development. Even though the KEK-DA was built upon the former fast cycling Booster for the KEK-PS. Several original works have been done to realize such a compact and cost-effective machine with enough flexibility as a demonstration induction synchrotron. Especially, the solid state devices developed here can be easily adopted in other compact accelerators.

Chapter 4

Beam Production: ECR Ion Source and the Operational Optimization

As we will see in the following chapters, when dealing with the beam behaviors in the downstream, the discussion on the beam production here turns out to be very essential. For example, the long beam (several ms) are observed to have longitudinal momentum modulations. The quasi-3D profile monitor discussed in Chapter 5, which has been newly developed, observed that the front part of the beam notably deviates from the center of the beam line. The reason resulting in this phenomena was found to be the beam loading effect at the extraction region of the ECRIS and the post-acceleration column in the High Voltage Terminal in which the ECRIS is installed.

In this chapter, after briefly reviewing the operation principle of an ECRIS, the main parameters related to the KEK-DA ECRIS are given. The discharge problem observed at the extraction region of the ECRIS is discussed with the redesign works to suppress this problem. After the ECRIS was confirmed to be stable in operation, the operation optimization works were performed. These are also discussed.

4.1 Operation principle

From the late 1960s when the Geller Group started the ECRIS study for fusion plasma research, the ECRIS has been widely used in producing highly charge state ion beams [18]. Its operational principle is to generate the plasma by microwave heating. Electrons efficiently obtain the energy from microwaves when the frequency of the cyclotron motion of the electron in the magnetic field is equal to the microwave
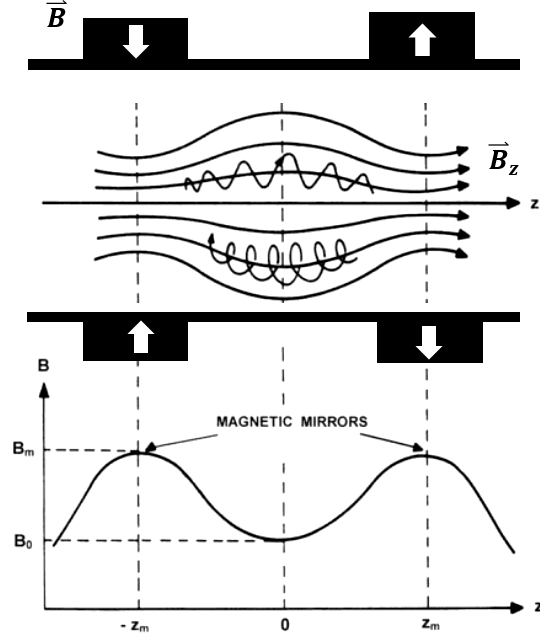
Figure 4.1: Plasma confined by the mirror field.

frequency.

$$f_e = \frac{eB_{ECR}}{2\pi m_e} = f_{rf} \tag{4.1}$$

The microwave heating process will generate the plasma. A fraction of the ion particles of the plasma can be extracted to the downstream. In Eq. (4.1), f_e is the cyclotron frequency, B_{ECR} is called ECR magnetic flux density, e is the electron charge and m_e is the electron mass and f_{rf} is the microwave frequency. Generally, the plasma will be generated through the microwave heating of some target gas, which is supplied to the plasma chamber. The plasma should be confined with a mirror field as shown in Fig. 4.1 [19]. When the ECRIS is elevated to a high potential, the ion particles can be extracted from the plasma. The extraction current density J is limited by the Child-Langmuir law as,

$$J = \frac{4}{9}\varepsilon_0 \sqrt{\frac{2Qe}{Am}} \frac{V^{1.5}}{d^2} \tag{4.2}$$

where A is the mass number, Q is the charge stage of the ion particle, e is the unit charge and m is the proton mass, ε_0 is the electric constant, V is the extraction

voltage, d is the gap size between the anode (on the plasma side) and the cathode (downstream side).

4.2 KEK-DA ECRIS

The KEK-DA ECRIS is a 9.4 GHz with permanent magnets. With Eq. (4.1), the B_{ECR} of the KEK-DA ECRIS is,

$$B_{ECR} = \frac{2\pi m_e f_{rf}}{e} = 0.336\,\text{T} \qquad (4.3)$$

The ECIRS with the extraction region is shown in (Fig. 4.2). The ECRIS parameters are listed in Table 4.1.
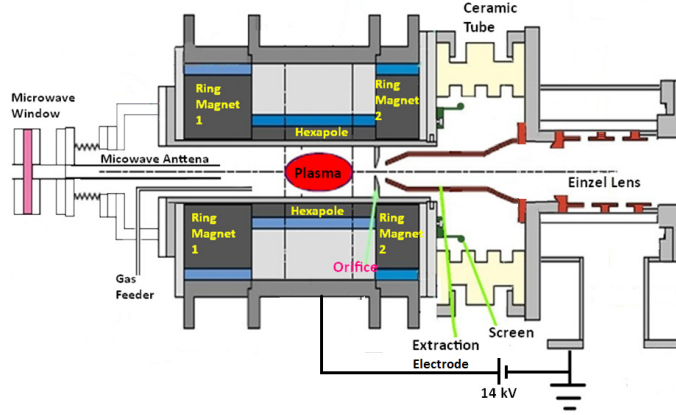

Figure 4.2: Schematic view of the ECR ion source for the KEK-DA.

As shown in Table 4.1, the maximum microwave power from the TWT Amplifier is around 700 W, usually ECRIS operated in CW mode will need cooling system. Nonetheless, in the KEK-DA ECRIS, the ECRIS is operated in the pulse mode so that the energy deposited to the ECRIS is ignorable. The amplitude of the pulse to trigger the TWT Amplifier is also used to control the output power. The cooling-free ECRIS is achieved. This change greatly reduced the size and relaxed the complexity of the ECRIS that must be embedded in the high voltage platform.

The mirror field is produced by a batch of permanent magnets as shown in Fig. 4.3 and the axial magnetic flux density was shown in Fig. 4.4.

Since the ECRIS has been used so widely and studied for a long time, the optimum magnetic field ratios suggested for high performance ECR ion source are listed in

Table 4.1: Parameters of the KEK-DA ECRIS.

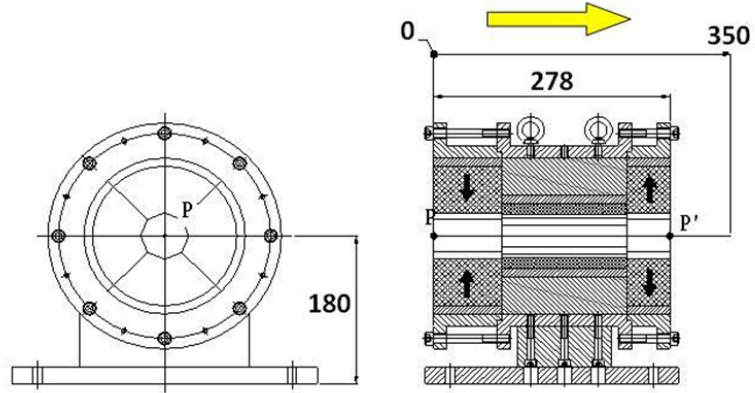|	
Frequency	$\sim 9.4\,\mathrm{GHz}$
Microwave Power	$\sim 700\,\mathrm{W}(max)$
Plasma chamber diameter	30 mm
Hexapole length	148 mm
B_{inj}	0.710 T
B_{ext}	0.565 T
B_{min}	0.178 T
B_{surf}	0.597 T
Orifice diameter	2 mm

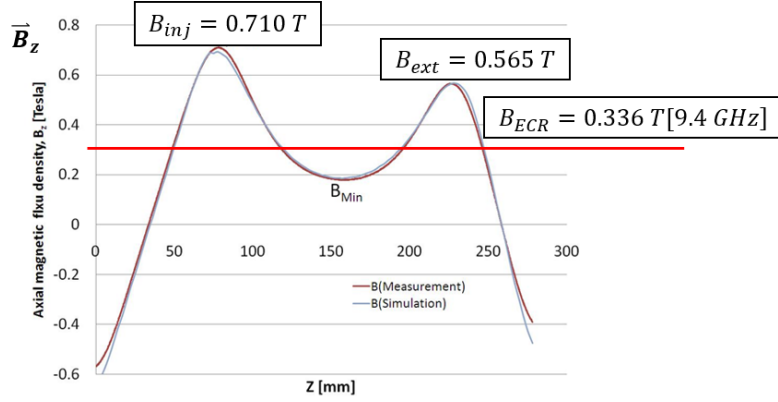Figure 4.3: The KEK-DA ECRIS with permanent magnets.

Figure 4.4: The axial magnetic field measured and compared with the simulation [20].

Table 4.2 [21]. From Eq. (4.3) and Table 4.1, these ratios for the KEK-DA ECRIS are also listed in Table 4.2 for comparison. These ratios suggest that the KEK-DA should operate with higher axial magnetic field.

Table 4.2: Optimum ratios for high performance ECRIS.

Ratio	Optimum	DA ECRIS
B_{inj}/B_{ECR}	~ 4	2.11
B_{ext}/B_{ECR}	~ 2	1.68
B_{min}/B_{ECR}	~ 0.8	0.53
B_{surf}/B_{ECR}	≥ 2	1.78
B_{ext}/B_{surf}	≤ 0.9	0.95

4.3 Dealing with the discharge problem

In order to obtain high intensity heavy ion beams, a higher extraction voltage is preferred. Of course this extraction voltage has to be optimized with the extraction structure design. In the case of the KEK-DA, a DC Cut with capability of $20\,\mathrm{kV}$ insulation has been used to insulate the ECRIS body to the microwave system which is

at the ground potential. However, even after several years of operation, the discharge problem often occurred in the extraction region between the extraction electrode and the plasma chamber. For example, Fig. 4.5 shows the damage made by discharge to the plasma chamber and Fig. 4.6 shows the damage on the extraction electrode. Besides, the plasma chamber was made of aluminum which is very vulnerable to the discharge damage. In return, the discharge problem happened more easily on such a damaged surface. As a result, the extraction voltage could not be over 10 kV due to the discharge.
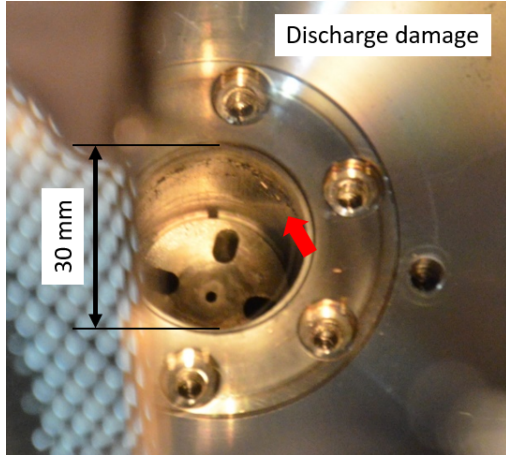
Figure 4.5: Discharge damage: plasma chamber.
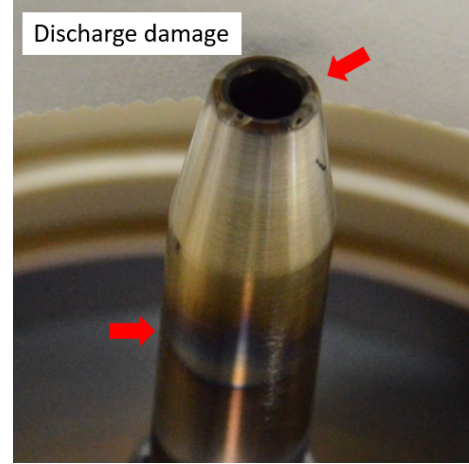
Figure 4.6: Discharge damage: extraction electrode.

The discharge problem can be solved with basically two methods: (1) increase the distance between the electrodes; (2) provide a better vacuum. Therefore, the following works have been done through the engineering consideration. After all these works, the ECRIS now can be stably operated at 14 kV.

4.3.1 Thinner extraction electrode

The present diameter of the plasma chamber is 30 mm, this size is limited by the permanent magnets and cannot be changed any further. To increase the distance between the plasma chamber and the extraction electrode, the only way left is to reduce the diameter of the latter. Thus, the inner diameter of the extraction electrode has been decreased from 14 mm to 10 mm.

4.3.2 Orifice without extra holes

In the old design of the orifice, there are four large extra holes to improve the gas conduction in the vacuum. However, the gas coming from the plasma chamber will pass through the extraction region deteriorates the local vacuum condition. The solution is a new orifice design with no holes. The vacuum in the plasma chamber is tuned through the gas control system. After the replacement, the gas flow required by the ECRIS has been reduced. The old and the new design of the orifice are compared in Fig. 4.7 and Fig. 4.8. Fig. 4.7 also shows the orifice after discharge. In Fig. 4.8 there are four small shallow screw holes reserved for installation.
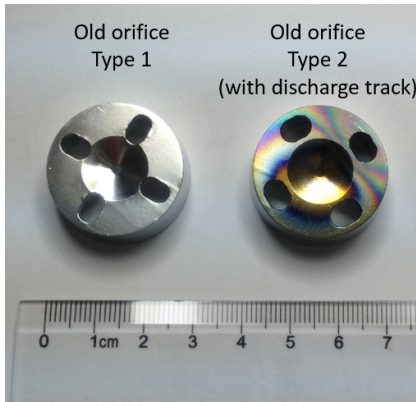
Figure 4.7: Old orifice.
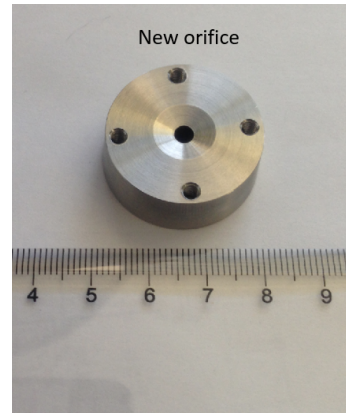
Figure 4.8: New orifice.

4.3.3 Replacement of plasma chamber

As mentioned, the plasma chamber was made of aluminum (*Al*). *Al* has a high yield of generating secondary electron which will benefit the production of high charge state ion. Thus it is often used in the plasma chamber by coating to the inner surface around the plasma generation region. In the KEK-DA case, the plasma chamber is made by *Al* so no coating is required. The problem is the aluminum part extended to the extraction region where discharge may occur. So in the extraction region, it is better to use other metal materials. With this consideration, a new plasma chamber made of stainless steel (SUS316), has replaced the original *Al* chamber.

61

4.3.4 Replacement of gas supply system

In the old system, plastic pipes are used to transport the gas to the plasma chamber. With a reasonable length, it can sustain the high voltage between the ECRIS body and the upstream devices of the gas supply system. However, the degassing process in the inner surface of the plastic pipe will mix the target gas with unnecessary gas molecules. This process also increase the possibility of the high voltage breakdown on the inner surface of the plastic pipe. In fact, we have observed damages due to the high voltage breakdown on the surface of the plastic pipe. In the present system, flexible SUS pipes have been adopted. The high voltage insulation is realized with short ceramic pipes.

4.3.5 Vacuum pump

To further increase the vacuum condition in the extraction region, the Turbo Molecular Pump(TMP) in the Einzel Lens Chopper region has been replaced with a larger one(from $300\,\mathrm{L}$ to $500\,\mathrm{L}$), which has also been installed closer to the extraction region.

4.4 Einzel Lens Chopper

It should be pointed out that the KEK-DA is a single turn injection machine, the typical acceptable beam length is several microseconds, for example, in case of He^{1+}, the revolution period is about $12\,\mathrm{\mu s}$ at $200\,\mathrm{keV}$ injection. Given the fact that induction cells have to be excited with a pair of pulses with opposite polarity to prevent the magnetic cores of the induction cells from saturation, at present, the acceptable length is less than a half of the revolution period. Therefore, a chopper is required.

The chopper is installed just after the extraction region of the ECRIS. Fig. 4.9 shows a schematic view of the Einzel Lens Chopper, where the middle electrode is a high voltage while both sides are connected to the ground. When the particle enters the first half of the Einzel Lens Chopper ("slow down" region inFig. 4.9), it will be decelerated and lose energy. When it passes through the second half ("speed up" region) and leaves the Einzel Lens, it will be accelerated and gain energy. When the Einzel Lens works as a focusing device, the voltage on the middle electrode stays constant, so there is no net gain or loss of the particle energy.

When it works as a longitudinal chopper as well as the focusing device in the transverse direction, a voltage pulse is used to control whether the particles can pass though it or not. The voltage pulse is shown in Fig. 4.10. When this voltage on the middle electrode is high enough ("Blocking V"), the particle will lose all its kinetic
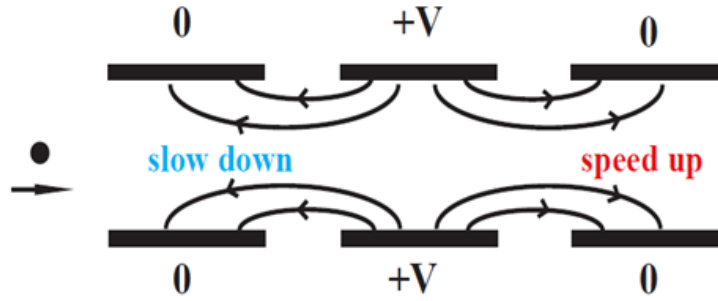
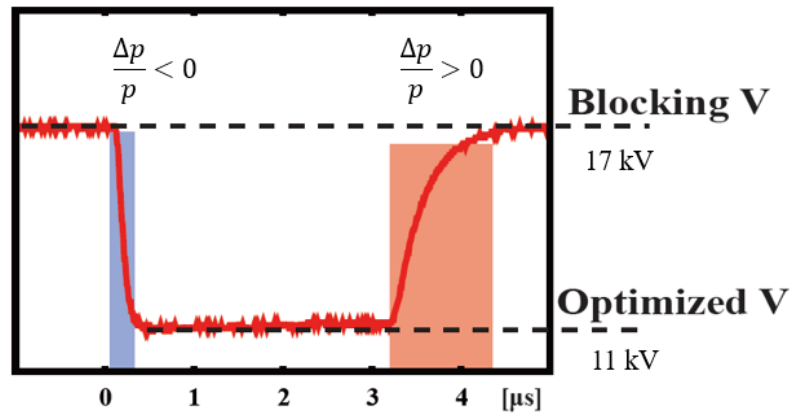Figure 4.9: schematic view of the Einzel Lens Chopper.

Figure 4.10: Pulse voltage on the middle electrode used to chop the beam.

63

energy and cannot pass through, even be kicked back by the Einzel Lens Chopper. When this voltage drops to an appropriate amplitude ("Optimized V") the particle can pass through the Einzel Lens Chopper and the beam will be well focused.

However, during the transitional process when the particle passes through the "speed up" region at a different voltage when it passes through the "slow down" region, the net energy gain or loss will not be zero. During the voltage drop region in the voltage pulse profile, particles enter the Einzel lens at a higher voltage and leaves the Einzel lens at a lower voltage, so the momentum deviation of these particles will be negative. Similarly, during the voltage rise region, the momentum deviation will be positive.

This momentum deviation has been extensively discussed in [22]. This mechanism creates a chopped beam pulse with the momentum deviation along the pulse.

4.5 Optimization of the operation parameters

4.5.1 Extraction voltage

The Child-Langmuir law in Eq. (4.2), which indicates that for high current intensity suggests that the extraction voltage should be set as high as possible and the extraction gap (Fig. 4.2) should reach a minimum.

However, in the practical design and operation, avoiding vacuum breakdown and confirming the beam transportation to the downstream is much more important. For example, Fig. 4.11 shows the results of the He^{1+} extracted at different voltage. The gas flow rate was set as 0.06 sccm and the microwave power is fixed at about 600 W (1.1 V for the power control of the TWT Amplifier)

As shown in Fig. 4.11 that, the obtainable beam current is increasing with the extraction voltage, from 10 kV to 16 kV. However, the risk of discharge also increases, especially for much higher extraction voltage.

This experiment has been done with the same configuration of the extraction region. We did not change the extraction gap size or the shape of the extraction electrode. This indicates that for a given configuration of the extraction region, considering the transport efficiency, higher voltage does not always yield anticipated larger output as shown in this figure. It also implies the capability of the ECRIS at the given gas flow rate and microwave power.

It is worth to mention that this work has been done after removing the discharge problem as mentioned in previous chapter. Otherwise the extraction voltage could not have been applied to as high as 16 kV for present ECRIS.
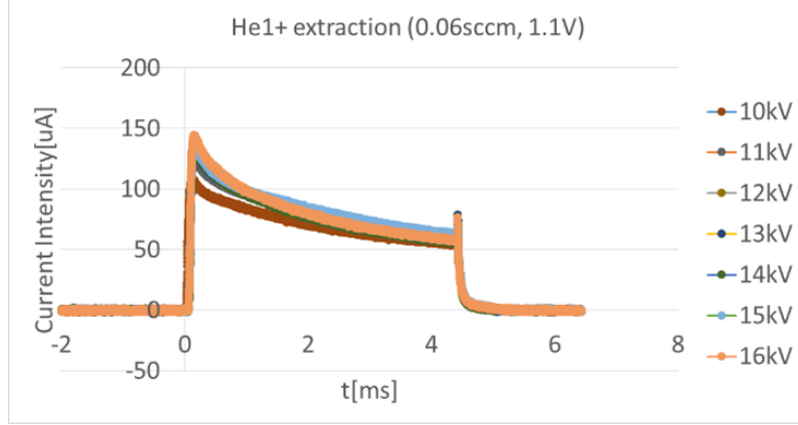
Figure 4.11: Extraction Voltage dependence: He^{1+} measured at FC1(Fig. 3.1).

4.5.2 Einzel Lens Chopper voltage optimization

As discussed, the Einzel Lens can be chosen to work as just a focusing device or at the same time as a chopper by controlling the voltage on the middle electrode. Specifically, when only working as a focusing device, the "Opitmized V" should be found, while when working as a chopper, the "Blocking V" should be found. This can also be done with the IGUN simulation. Supposed that the beam from the extraction region stays the same, by changing the voltage on the middle electrode of the Einzel Lens Chopper, the simulation results with IGUN for He are shown in Fig. 4.12.

In this case, the He is extracted at 10 kV and the "Optimized V" and "Blocking V" are found to be 8 kV and 13 kV, respectively.

4.5.3 Gas flow rate

The vacuum pressure in the plasma chamber also plays an important role in determining the extractable current intensity. The direct way to change the vacuum inside the plasma chamber is by controlling the gas flow rate.Fig. 4.13 shows the results at different gas flow rates, where higher gas flow indicates worse vacuum pressure, resulting in more target gas particles in the plasma chamber.

Fig. 4.13 shows an interesting phenomena which is directly related to the plasma generation process inside the plasma chamber. Lower gas flow rate yields not only lower current intensity but also slower plasma production. In other words, the microwave heating takes more time to build up the plasma before the ions can be extracted.
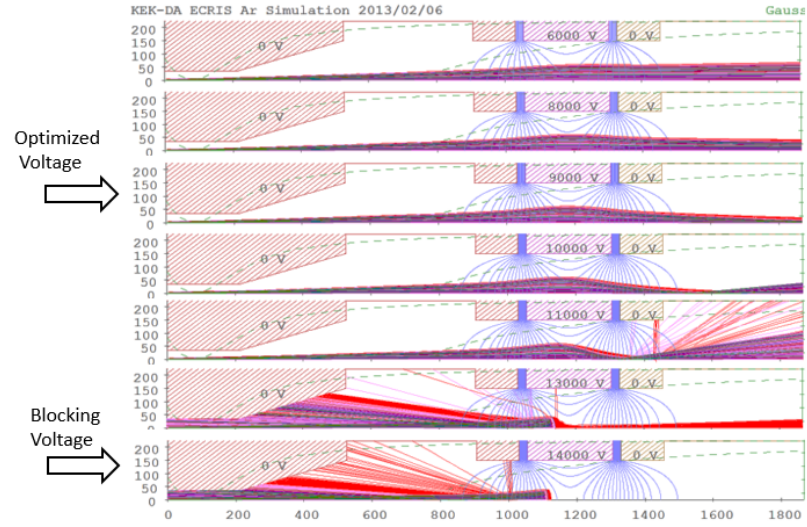
65

Figure 4.12: *He* transport simulation in the Einzel Lens Chopper region.
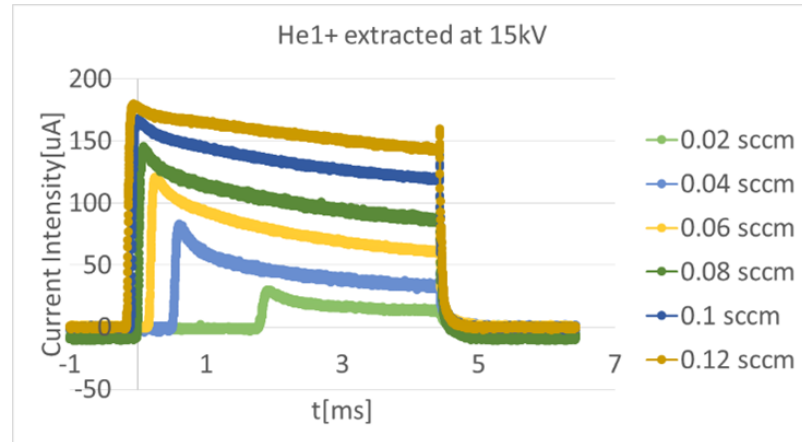

Figure 4.13: Gas flowrate dependence: He^{1+} at 15 kV.

As more gas particles are available in the plasma chamber, the plasma build-up process becomes faster and more gas molecules are ionized. Thus the ion particles can be extracted faster than in the case of lower gas flow rate.

Meanwhile, Fig. 4.13 also shows that there is a saturation on the extractable beam current intensity. This may come from the reason that when there are more gas particles inside the plasma chamber, the recombination process of the free electrons and the ions is more likely to happen.

Though the simple explanation is given here, it is usually complicated when studying the plasma generation process inside the plasma chamber.

4.5.4 Chopping position

As can be seen from Fig. 4.11 and Fig. 4.13, the beam from the ECRIS is typically in *ms* order. As mentioned in Sec. 4.4, the KEK-DA ring takes a beam in µs. The Einzel Lens Chopper is used to chop the beam. The beam length can be easily adjusted by controlling the pulse width in Fig. 4.10. In addition, the short beam of µs can be chopped from any selected position from the long beam. As an example, Fig. 4.14 shows the results chopped at different positions inside the long beam.
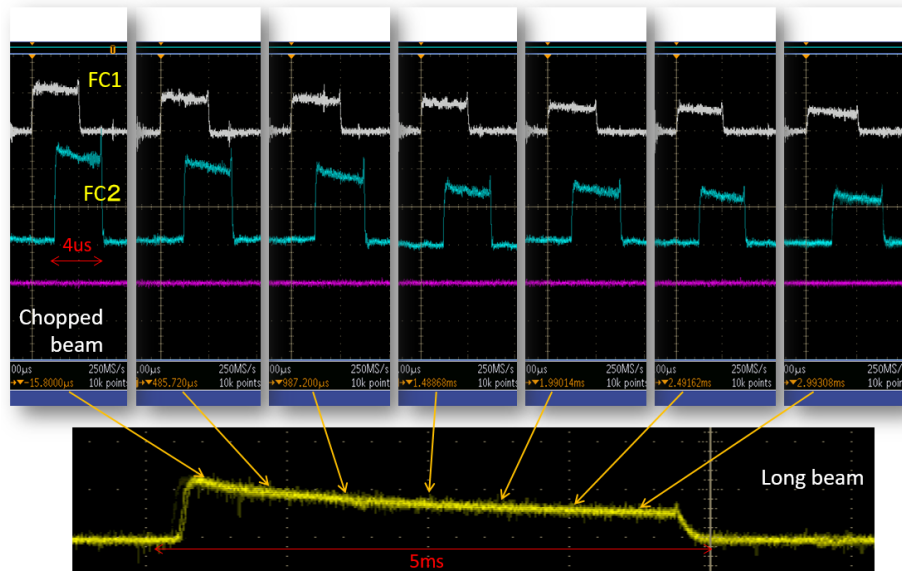

Figure 4.14: Four µs beam chopped from the five ms at different positions.

Fig. 4.14 also shows that at the head of the long beam the current intensity is usually higher than the beam end. So through the beam commissioning, usually the

beam is chopped at the very head to get higher current intensity.

4.5.5 Frequently used beam in KEK-DA

In KEK-DA, Helium is often used in the KEK-DA ECRIS because it provides high current intensity He^{1+} beam. Argon is also frequently used because it has a wide A/Q range which is necessary to show the capability of induction synchrotron in accommodating all ion species with different charge states.

At present, the typical beam current intensity obtained for Helium and Argon are listed in Table 4.3, which were measured at FC1 in Fig. 3.1. Note that these figures were tested at different settings of the ECRIS and for stable operation, they are slightly lower than the maximum capability of the ECRIS for each ion species. In this table, the Ar^{1+} is not available due to the limited range of the excitation current of the BM1 (Fig. 3.1)

Table 4.3: Typical beam current intensity obtained in the KEK-DA ECRIS (in µA).

Charge State	He	Ar
1+	240	-
2+	25	40
3+	N/A	13

As shown in Table 4.3, the KEK-DA ECRIS can not provide high current intensity beams like Ar. In fact, the current intensity turned out to be the limiting factor in the beam commissioning as in [8]. In addition, in the study of intensity dependent effects like space charge, the capability of generating higher current intensity beam is required. Further upgrade on the KEK-DA ECRIS to generate higher beam intensity by adopting proved techniques [23] such as biased voltage or mixing gas is possible.

4.6 Summary

In this chapter, the principle of ECRIS has been briefly reviewed with the discussion on the KEK-DA ECRIS. More importantly, after the modification works in previous chapter, the KEK-DA ECRIS can be operated very stable at 16 kV extraction voltage (as shown in Fig. 4.11), compared with less than 10 kV operation voltage at the late of previous ECRIS after several years operation.

After the configuration is fixed, the operation parameters like the extraction voltage, pulse settings of the Einzel Lens Chopper and the gas flow rate have been discussed. These works helped us to get the best performance of this ECRIS at present status.

The discussion of this chapter, especially the extraction region and the Einzel Lens Chopper, will help to explain the experimental studies on the LEBT line.

Chapter 5

Beam Transportation: Experimental Studies on the LEBT Line

In order to understand the beam distribution in the phase space in both of the transverse and the longitudinal direction before injection to the ring, which are the prerequisites of the discussion on the beam behavior in the ring, two experimental studies on the LEBT line will be discussed in this chapter. In the first study, the Courant-Snyder parameters, also known as Twiss parameters, will be evaluated experimentally with the multi-wire grid profile monitors. In the second one, the multi-wire grid profile monitor were modified to be able to capture the quasi-3D profile of the beam. With this modification, the longitudinal momentum deviations has been evaluated for the long beam (four ms) and the short beam (four µs). At the same time, the mechanisms for the different momentum deviation in the long beam and the short beam were also successfully identified.
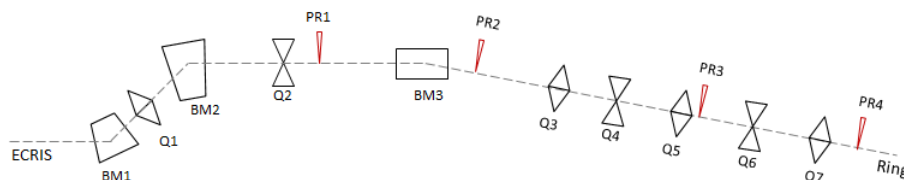

Figure 5.1: LEBT line layout and the Profile Monitors online.

5.1 Beam parameters fitted with profile monitor results

As mentioned in Chapter 3, there are four profile monitors (PR) available on the LEBT line. A photo of these monitors can also be seen in Chapter 3 Fig. 3.8. Here the layout of LEBT is simply sketched in Fig. 5.1.

A typical beam profile measurement results on the LEBT is shown as in Fig. 5.2,
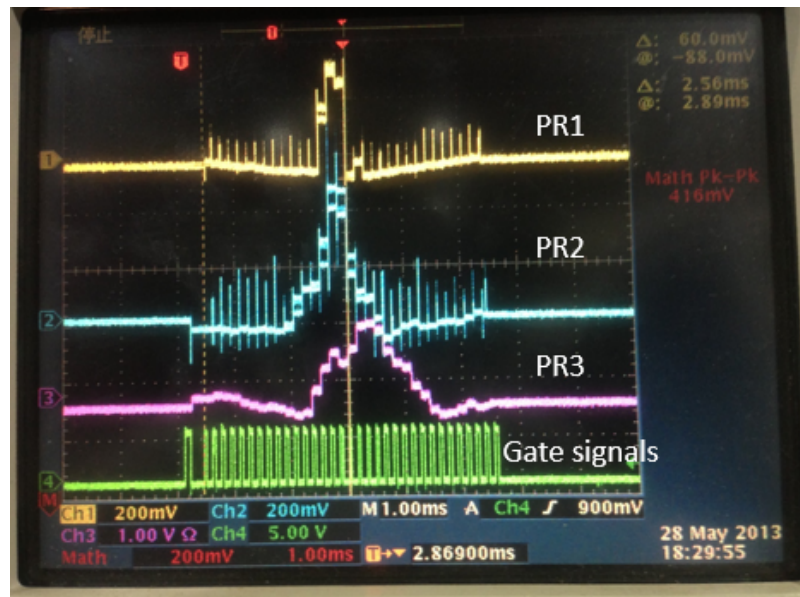
Figure 5.2: Typical profile monitor results (horizontal) as measured in PR1, PR2 and PR3.

PR2 and PR4 are used for the experiment here due to the reason that between the two, there are only five quadrupole magnets. Because PR3 is originally designed for polarized beam, it has a very large vertical wire width (more like a plate rather than a wire), so it will block the almost all the beam when it is inserted in the beam line. As a result, it is not an option in this experiment.

In addition, the long beam is chosen in this experiment because it has a larger signal on the beam profile monitor which makes the data fitting easier.

5.1.1 Background of the method

As described in Chapter 2 Sec. 2.1.3 the Courant-Snyder parameters can be transported through the beam line as Eq. (2.109). From s_0 to s_1, it can be written as,

$$
\begin{pmatrix} \beta_1 \\ \alpha_1 \\ \gamma_1 \end{pmatrix} = \begin{pmatrix} a_{11}^2 & -2a_{11}a_{12} & a_{12}^2 \\ -a_{11}a_{21} & a_{11}a_{22} + a_{21}a_{12} & -a_{12}a_{22} \\ a_{21}^2 & -2a_{21}a_{22} & a_{22}^2 \end{pmatrix} \begin{pmatrix} \beta_0 \\ \alpha_0 \\ \gamma_0 \end{pmatrix}
\tag{5.1}
$$

where a_{ij} is the elements in the transfer matrix for the particle coordinates as,

$$
\begin{pmatrix} x_1 \\ x_1' \end{pmatrix} = \begin{pmatrix} a_{11} & a_{12} \\ a_{21} & a_{22} \end{pmatrix} \begin{pmatrix} x_0 \\ x_0' \end{pmatrix}
\tag{5.2}
$$

The transfer matrix of different type element in an beam line can be found in Sec. 2.1.2.

In addition, the relationship between the beam size (denoted as 2σ, where we assume the transverse beam distribution is normal and choose 2σ as the beam size) and the beta function is,

$$
2\sigma = \sqrt{\varepsilon\beta}
\tag{5.3}
$$

where ε is the beam emittance. If both sides of Eq. (5.1) are multiplied by ε,

$$
\begin{pmatrix} \varepsilon\beta_1 \\ \varepsilon\alpha_1 \\ \varepsilon\gamma_1 \end{pmatrix} = \begin{pmatrix} a_{11}^2 & -2a_{11}a_{12} & a_{12}^2 \\ -a_{11}a_{21} & a_{11}a_{22} + a_{21}a_{12} & -a_{12}a_{22} \\ a_{21}^2 & -2a_{21}a_{22} & a_{22}^2 \end{pmatrix} \begin{pmatrix} \varepsilon\beta_0 \\ \varepsilon\alpha_0 \\ \varepsilon\gamma_0 \end{pmatrix}
\tag{5.4}
$$

The following relationship can be selected from Eq. (5.4),

$$
\varepsilon\beta_1 = a_{11}^2\varepsilon\beta_0 - 2a_{11}a_{12}\varepsilon\alpha_0 + a_{12}^2\varepsilon\gamma_0
\tag{5.5}
$$

In Eq. (5.5), the following observations are helpful,

1). The emittance ε is assumed constant here

2). $(\beta_0, \alpha_0, \gamma_0)$ are Courant-Snyder parameters at the start point

3). a_{11} and a_{22} are elements of transfer matrix as in Eq. (5.2).

4). $\varepsilon\beta_0$ and $\varepsilon\beta_1$ are beam sizes at start and end which can be measured with two profile monitors

Therefore, by measuring the beam size at two locations with profile monitors, the Courant-Snyder parameters and the emittance can be obtained. Given that the transfer matrix is known, in total there are three unknown variables: $\varepsilon, \varepsilon\alpha_0, \varepsilon\gamma_0$. Thus at least three independent equations are necessary to solve these unknown variables. In addition, the ε is always stick with the Courant-Snyder parameters, so it is easier to solve for $\varepsilon\alpha_0, \varepsilon\gamma_0$ as two variables and the emittance can be obtained with the relationship between the Courant-Snyder parameters in Eq. (2.102),

$$\varepsilon = \sqrt{\varepsilon\beta_0\varepsilon\gamma_0 - \varepsilon\alpha_0} \tag{5.6}$$

In order to build independent equations, by changing the focusing strength of the quadrupole magnets, the transfer matrix Eq. (5.2) will change accordingly. In case that the lattice setting before the chosen start point does not change, by changing the lattice between start point s_0 and the end point s_1, the beam size measured with profile monitor at s_1 will change.

Suppose that n cases of the lattice setting between s_0 and s_1 have been chosen, then from Eq. (5.5),

$$[\varepsilon\beta_1]^i = [a_{11}^2]^i\varepsilon\beta_0 - 2[a_{11}a_{12}]^i\varepsilon\alpha_0 + [a_{12}^2]^i\varepsilon\gamma_0$$
$$i = 1, 2, 3, 4, 5, \cdots, n \tag{5.7}$$

then $(\varepsilon\beta_0, \varepsilon\alpha_0, \varepsilon\gamma_0)$ can be obtained from fitting all the data for these equations. Here $(\varepsilon\beta_0$ is actual know beam size measured with the profile monitor at s_0. But the measured beam size can be used as an approximation in the fitting process which makes the fitted results more reliable.

5.1.2 Experimental results

multi-wire grid profile monitors

In Fig. 5.1,odd numberings of Q-magnet are focusing quadrupole magnets and even ones are defocusing for the horizontal direction (inverse for the vertical direction). In this experiment, Q3 and Q7 are excited in series with the same current and Q4 and Q6 are excited in series with another independent current.

The core part of the profile monitor is a multi-wire grid which consists of 32 wires in each direction. Given the spacing between adjacent wires is 2.5 mm, the range can be measured with these profile monitors are $(-4\,\text{cm}, 4\,\text{cm})$. A photo of the wire-grid

is shown in Fig. 5.3 and the parameters for it is listed in Table 5.1. These wires are so thin (diameters 30 μm) that they have little impact on the beam in operation.

Table 5.1: Parameters of the wire grid.

Diameter of wires	30 μm
Wire spacing	2.5 mm
Number of wires	32 wires for X/Y
Measurable range	-4 to 4 cm for X/Y
Material	Au-plated W
Frame insulation	Ceramic

Signals generated by the wire grid are taken to the signal processing unit (Fig. 3.10). A series of gate signals are used to control the delay module in the signal processing unit to display all the signals on the oscilloscope as shown in Fig. 5.2 and Fig. 5.4.

Fig. 5.4 also shows that except for the beam profile, the profile monitor also give the information that how much the beam center deviates from the reference trajectory which is assumed at the chamber center.

Fitting method

Assume that the beam profile is of normal distribution, Eq. (5.8) could be used to fit the profile, in which μ indicates the deviation of the fitted center and σ reflects the beam size. For normal distribution (Gaussian distribution), the area between $\mu - 2\sigma$ to $\mu + 2\sigma$ is about 95% of the whole area is used to stands for beam size(but in fact, it is only half width of the total beam size). For example, Fig. 5.5 is a fitting result for Fig. 5.4, which shows that the deviation from the orbit center is very small, less than 1 mm, and the beam size in is about 0.6 mm.

$$Ae^{-\frac{(x-\mu)^2}{2\sigma^2}} + C \tag{5.8}$$

Fitted results

In this experiment, for simplicity, PR2 (s_0) and PR4(s_1) (Fig. 5.1) are used to take the experimental data while changing the excitation currents for Q3 to Q7. PR3 is not used because it is originally made for polarized beam profile measurement so its
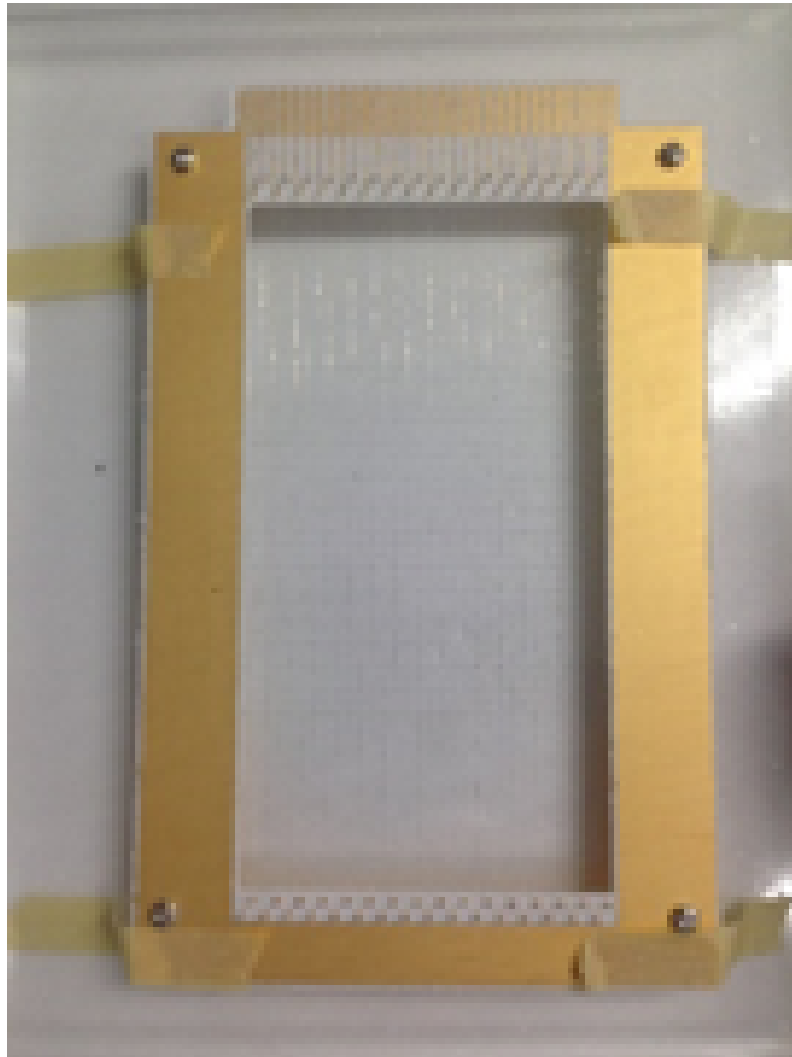
75

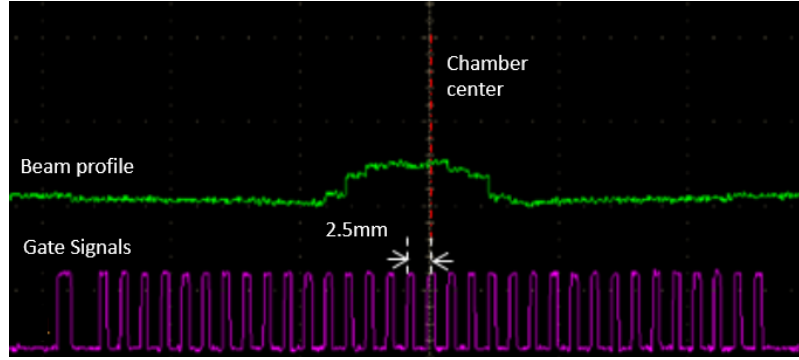Figure 5.3: The wire grid used in the profiel monitor.
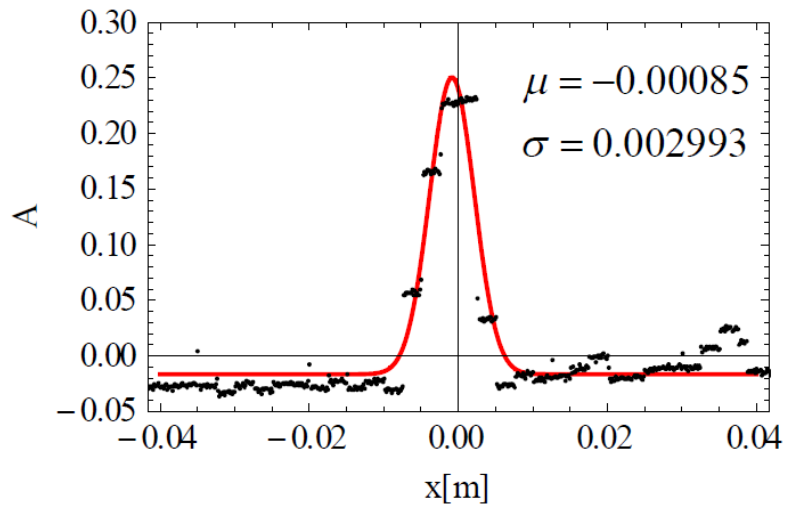
Figure 5.4: Beam profile and the gate signals.

Figure 5.5: Fitted results for Fig. 5.4.

vertical wires are different from other monitors. Settings for the quadrupole magnets used in the experiment are listed in Table 5.2.

Table 5.2: Excitation current for Q3 to Q5.

	Excitation Current[A]
$I_{Q3/Q7}$	7.8, 8.2, 8.7, 9.2
$I_{Q4/Q6}$	5.8, 6.4, 7.0, 7.6, 8.2
I_{Q5}	1.44, 1.96, 2.43

In Table 5.2, there are four values of Q3/Q7, five values of Q4/Q6, and three values of Q5. This results a total possibility of 60 variations of the focusing strength between PR2 and PR4. All the beam profiles measured at PR4 under different settings of Q3 to Q7 are shown in Fig. 5.6 and Fig. 5.7, horizontal and vertical direction, respectively.
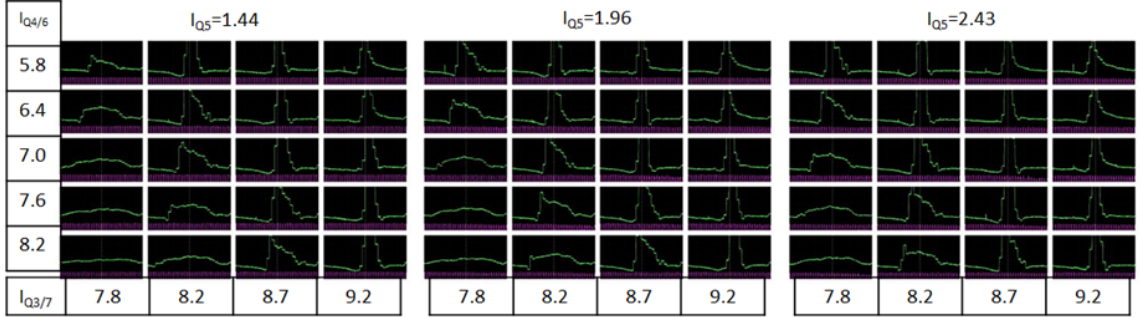

Figure 5.6: Experimental observation at PR4 iin terms of excitation current: horizontal.

$(\varepsilon\beta_0, \varepsilon\alpha_0, \varepsilon\gamma_0)$ in Eq. (5.7) are constants because the settings for upstream magnets were never changed through the experiment. The results from PR4 (beam size in 2σ) corresponds to $[\varepsilon\beta_1]^i$, where the case ID i starts from one to 60. The transfer matrix for Twiss parameters from PR2 to PR4 is calculated by using the excitation currents $(I_{Q3/Q7}, I_{Q4/Q6}, I_{Q5})$. All quadruple magnets are assumed the same type here. Field measurement results for one of the quadruple magnets is available [24] so it has been used for all the quadruples here. The k-value is related to the excitation current by,
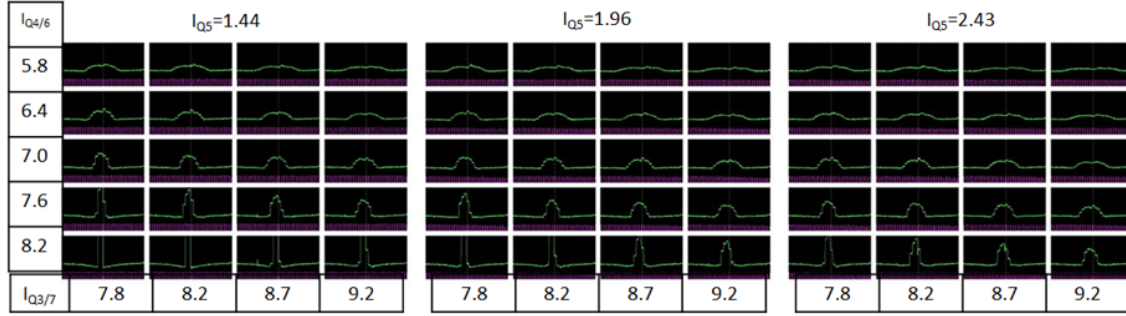
$$k = \frac{B'}{B\rho} \tag{5.9}$$

Figure 5.7: Experimental observation at PR4 in terms of excitation current: vertical.

where B' is given by the excitation current as,

$$B' = g \times I[A] + b \tag{5.10}$$

where $g = 0.0408$ and $b = 0.0207$ according to the field measurement. Strictly speaking, each quadruple magnet should have different excitation characteristics. All the quadruples on the present LEBT line had been used as magnets of the original KEK PS 40 MeV beam transport line and had been excited with much higher electrical currents. The gradient part, g, could be reasonably applied to all the quadruples while the remnant part, b, might vary due to their long time operation at different excitation currents. In this experiment, the beam has to be placed along the orbit center so that the variation of focusing strength changes only the beam profile, but not the beam's position. Thus we have done the orbit centering by optimizing the settings for upstream magnets (in front of PR2) before doing the experiment.

Though in total, there are 60 data sets, $(I_{Q3/Q7}, I_{Q4/Q6}, I_{Q5}, \varepsilon\beta_1[or 2\sigma])$ for each direction could be used for fitting for $(\varepsilon\beta_0, \varepsilon\alpha_0, \varepsilon\gamma_0)$, considering that the precision of the wire monitors, to reduce the ambiguity, those data points with small beam size should be used with cautions. Thus, in the fitting process, only part of the data points is used. Especially for the horizontal direction data, those data with too small beam size was excluded in the fitting. With $g=0.0408$ and $b=0.0207$ and proper initial constraints, fitting was made as shown in Table 5.3.

The fitted beam size in the horizontal direction at PR2 is almost the same as observed value (1.2 cm). The fitted beam size in the vertical direction at PR2 is slightly larger than the observed one (0.6 cm). Another point worth mentioning here is that the horizontal emittance is larger than the vertical one, which is in accordance with our operation experience on LEBT line.

Table 5.3: Fitted beam parameters at PR2.

$\beta_x[\mathrm{m}]$	α_x	γ_x	$\varepsilon_x[\mathrm{mm.mrad}]$	$2\sigma_x[\mathrm{cm}]$
3.32	-3.51	4.02	44.98	1.22
$\beta_y[\mathrm{m}]$	α_y	γ_y	$\varepsilon_y[\mathrm{mm.mrad}]$	$2\sigma_y[\mathrm{cm}]$
2.48	1.44	1.24	24.78	0.78

Fitting goodness

Once we get the beam parameters like the Courant-Snyder parameters and emittance at PR2. They can be transported down to the PR4 position using the same settings as in the experiment. The obtained results are compared with the measurement results in Fig. 5.8 for horizontal direction and Fig. 5.9 for vertical direction. The residual errors of the difference between the fitted results and the measurement are plotted in Fig. 5.10.
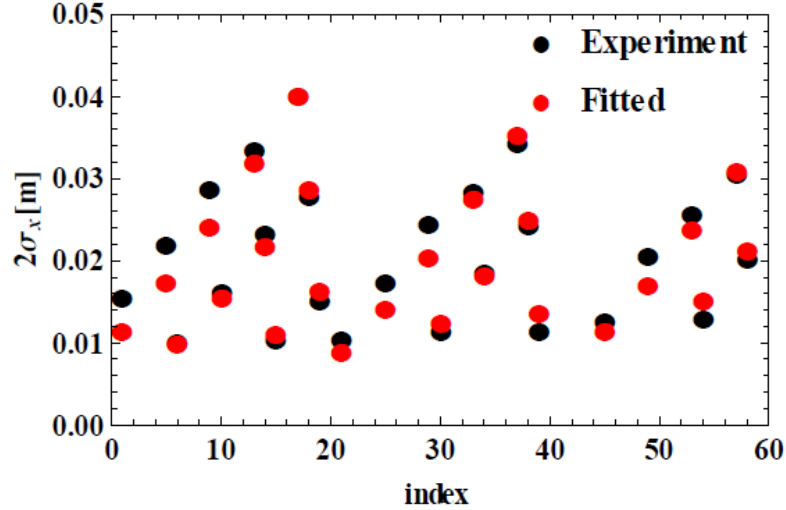

Figure 5.8: Comparison between fitted beam size and experimental results: horizontal.

From Figs. 5.8 and 5.9 we see that the over all fitting results are good. But the residual errors shown in Fig. 5.10 follow a pattern related to the excitation current for the quadrupole magnets.

At first it was doubted that the different b in Eq. (5.10). As a result, we arbitrarily
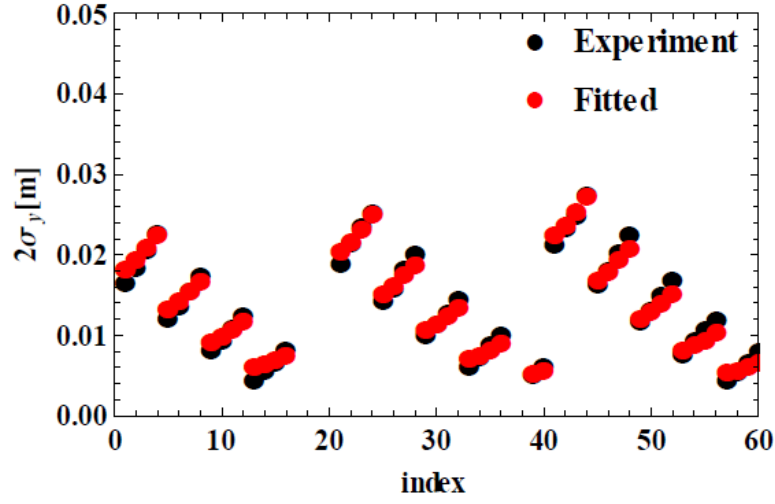
Figure 5.9: Comparison between fitted beam size and experimental results: vertical.
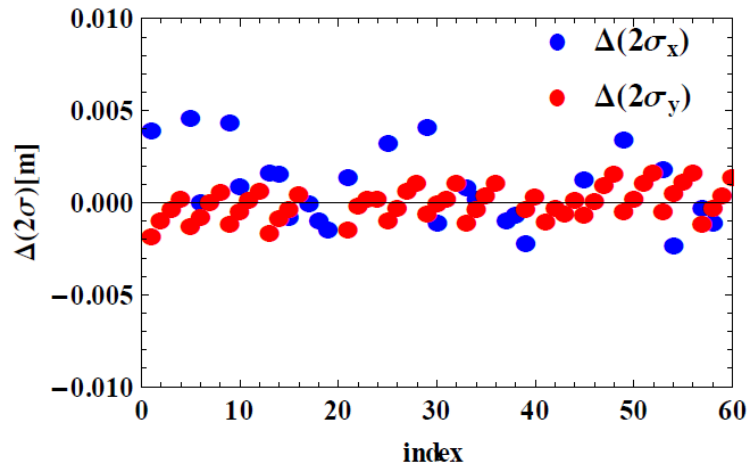

Figure 5.10: Fitting residual errors.

chosen the b to see its effect on the fitting results. The Root-Mean-Squre (RMS) value of the errors in Fig. 5.10 can be calculated. In Fig. 5.11, different cases of b are used in the fitting process to calculated the residual errors and the RMS values of each case is plotted. It indicates that the b term which stands for the remaining field of the quadrupole has little effects on the beam size measurement. It is obvious that the vertical measurement results have less error than the horizontal ones.
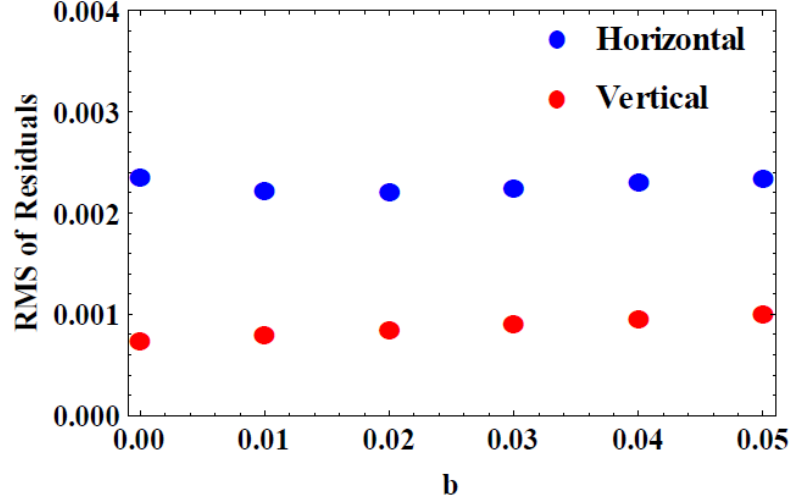

Figure 5.11: RMS residuals for various cases of b.

5.1.3 Difficulties in the beam parameters with this method

The LEBT lattice should be tuned to match the lattice in the ring. However, it turns out that it is a difficult task in the case of KEK-DA due to the following reasons.

1). Same equation to represent different quadrupole magnets. At the momentum only one measurement on the field distribution of the quadrupole had been done and the results are applied to all the magnets used here.

2). The beam shape deviated largely from normal distributions as can be seen in Fig. 5.6 and Fig. 5.7. This is due to the momentum deviation within the beam pulse which will be discussed in the next section.

3). The precision of the profile monitor, as discussed, the precision level of the profile monitor is 2.5mm, which means that typical beam size around 2 4 cm will have an error around 10%.

4). The dispersive system. As will be shown in next section and the in Chapter 8, in the downstream of the LEBT where the experiment is conducted, the dispersion function exists. It is ignored in this study to simplify the process. However, as indicated by Eq. (2.119), the measured beam size includes the dispersion effect from the momentum deviation.

Though the lattice on the LEBT needs further work, the fitted results obtained in Table 5.3 still give us useful information of the beam transport at the LEBT line. Specifically, the emittance in the horizontal and vertical directions are measured to be 45 mm.mrad and 25 mm.mrad at one sigma beam size. The measurement results by the Pepper Pot at test bench shows that at FC1, the emittance is 100 mm.mrad for horizontal and 70 mm.mrad for vertical [22]. Though these beam parameters depend highly on the beam condition in the upstream starting from the ECRIS, if we take this as the emittance corresponding to two sigma beam size, the emittance would be 25 mm.mrad for horizontal and 18 mm.mrad, we could see that the vertical emittance obtained here is not too far from the pepper port result while the horizontal result shows large difference due to the dispersion function and other reasons listed above.

5.2 Quasi-3D profile monitor development and longitudinal evaluation of the momentum deviation

5.2.1 Quasi-3D profile monitor

Configuration

As discussed in previous section, the existing profile monitor can only take horizontal or vertical beam profile without longitudinal information. In order to make it capable of capturing longitudinally dependent horizontal or vertical beam profile, a new data capture unit has been made. The data processing unit used in previous section (see Fig. 3.10) has been replaced by a new "Signal Capture" unit. The configuration of the "Signal Capture" unit and its connection to the monitor unit is illustrated in Fig. 5.12.

As mentioned in previous section, there are 32 channels (wires) in the horizontal or the vertical direction, corresponding to a measurement range (-4 cm, 4 cm) in both direction. These channels are well insulated from each other and are bundled into four groups (H1, H2, V1, and V2) to be connected easily with multi-pin connectors (Fig. 5.12). However, due to the limited number of channels available to the present
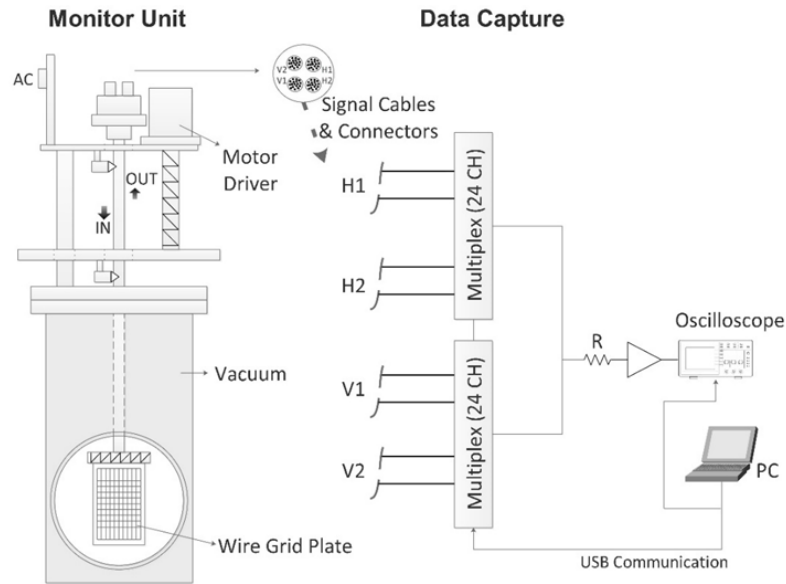
Figure 5.12: : Schematic view of the monitor unit and the data-handling diagram.

multiplexers used for selecting signal, only 24 of the 32 channels can be used for each direction, reducing the measurable range to (-2.5 cm, 2.5 cm) for each direction.

The "Signal Capture" unit can be simply connected to each Monitor Unit of the available profile monitor to measure the quasi-3D beam profile at different locations. In this experiment, PR1 and PR2 (Fig. 5.1) will be used.

Single Wire Signal

Electrical current signals generated on the wires when the beam hits the multi-wire grid are transferred to the two multiplexers, which select only a single channel's signal at a time and pass it to the oscilloscope. All channels are scanned in sequence. A resistor (R in Fig. 5.12) is used here to convert the electrical current into voltage which can be amplified with an amplifier then recorded by the oscilloscope.

Fig. 5.13 shows two measured signals from a single wire (yellow) for a $100\,k\Omega$ and a $1\,k\Omega$ resistor. Comparing them with the measurement results from the FC (purple) for the same beam, a larger resistance ($1\,k\Omega$) results showed a higher signal strength, but the longitudinal profile is distorted. As a result, we choose the smaller resistance ($100\,\Omega$) to prevent signal distortion.

The measurement results by FC2 (Fig. 3.1) are also shown in Fig. 5.13 for comparison.
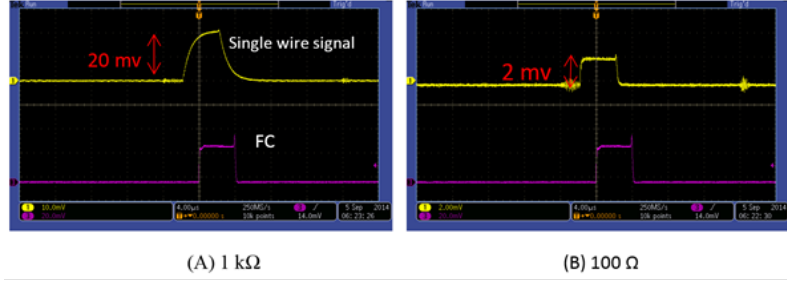
84

Figure 5.13: Single wire signal for different resistances.

From single wire signal to the Quasi-3D beam profile

After obtaining all the signals from the wire grid, the beam profile is reconstructed in accordance with the wire positions. For example, (a) in Fig. 5.14 shows a signal from one of the wires taken with the oscilloscope. With (b) in Fig. 5.14, all the wires in the horizontal vertical direction (each direction have 24 channels as discussed, horizontal direction for a short beam in this example) are plotted in sequence according to their physical layout. Finally, (c) in Fig. 5.14 shows the normalized intensity projection of (b) to the horizontal-longitudinal (x-t) plane or vertical-longitudinal (y-t) plane. Due to the fact that the Monitor Unit is the same as the existing multi-wire grid profile monitor which is intrinsically a quasi-2D profile monitor, the modified profile monitor, with additional profile in the longitudinal profile, is a quasi-3D profile monitor.
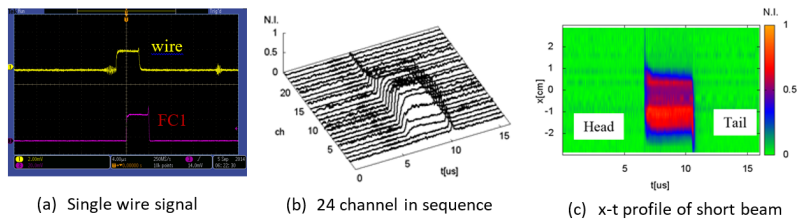

(a) Single wire signal   (b) 24 channel in sequence   (c) x-t profile of short beam

Figure 5.14: From single wire signal to the quasi-3D profile: (x-t) plane.

5.2.2 Longitudinal momentum deviation measurement

Theoretical background

From the viewpoint of the linear single particle motion described in Chapter 2, the transverse excursion from the referential orbit of a particle is (Eq. (2.119)):

$$x = x_\beta + D\frac{\Delta p}{p} \tag{5.11}$$

It is separated into two parts: the first part is the betatron oscillation as in Eq. (2.115); the second part is the deflection due to the dispersion, where D is the dispersion function and $\delta p/p$ is the momentum deviation from the referential particle.

For a beam containing many particles, the second part can be seen as the excursion of the beam center which can be measured with profile monitor. However, in order to experimentally obtain the longitudinal momentum deviation within the beam, longitudinally dependent beam profile is needed. The quasi-3D profile monitor meets this requirement by providing longitudinally dependent transverse profile.

LEBT dispersion function

In order to evaluate the momentum with Eq. (5.11), dispersion function along the beam line is required. Because the dispersion is resulted from the bending magnets, the dispersion function and its derivative are assumed to be zero at the entrance of the LEBT line. The dispersion function for this region is plotted as in Fig. 5.15, in which horizontal axes s is the distance along the referential orbit.

Tested beam

An $A/Q = 4$ ion beam is used in this experiment, where A is the mass number of the particle and Q is the charge state. When the Einzel Lens works just as a focusing device, the long beam is transported to the LEBT line. When the Einzel Lens works also as a longitudinal chopper, the short beam is transported to the LEBT line. The beam intensity profiles of the long beam and short beam measured with FC1 and FC2 as shown in Fig. 5.16 and Fig. 5.16. The beam parameters are listed in Table 5.4.

In the next two subsections, the longitudinal momentum deviation for the long beam (4 ms) and the short beam (4 µs) will be evaluated with the results of the profile monitors. Our study shows that the momentum deviation comes from different sources for the long beam and the short beam. Specifically, the longitudinal momentum deviation of the long beam is caused by the beam loading effects and for the short beam, it comes from the chopping process of the Einzel Lens Chopper (Sec. 3.2.3)
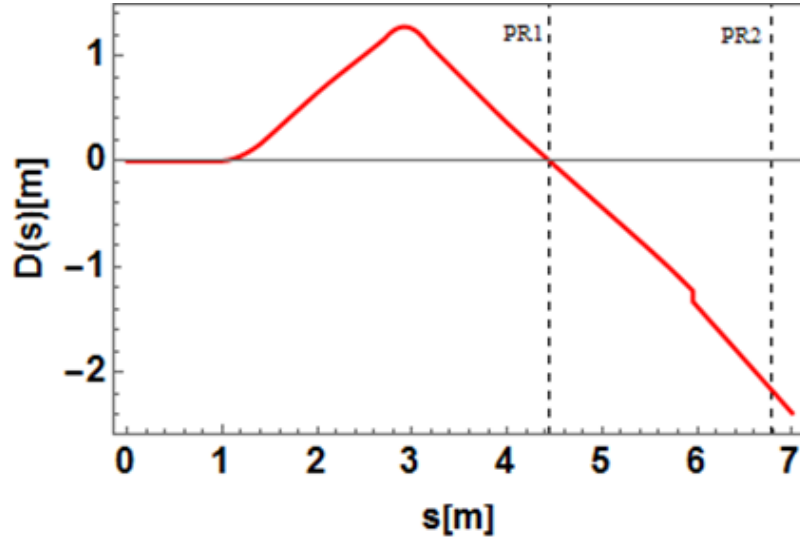
Figure 5.15: Dispersion function of the LEBT upstream.
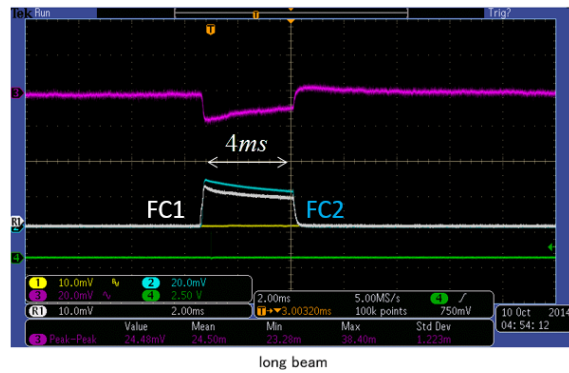
Figure 5.16: Long beam (4 ms) measured with FC.
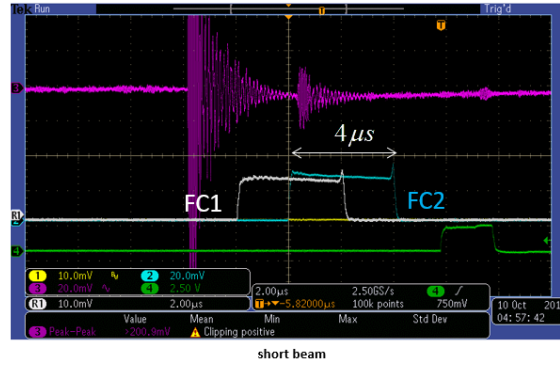
Figure 5.17: Short beam (4 µs) measured with FC.

Table 5.4: Beam parameters.

	Long beam	Short beam
Beam length	4 ms	4 µs
Energy	200 keV	
A/Q	4	
Intensity	$\sim 130\,\mu$A	
β	0.01	

used to chop the beam. Experimental results and simulation results will be given to confirm these sources and their contributions.

5.2.3 Long beam and beam loading effects

Results from the profile monitors

The results of the quasi-3D beam profile measured with the new system at PR1 are shown in Fig. 5.18 and Fig. 5.19.
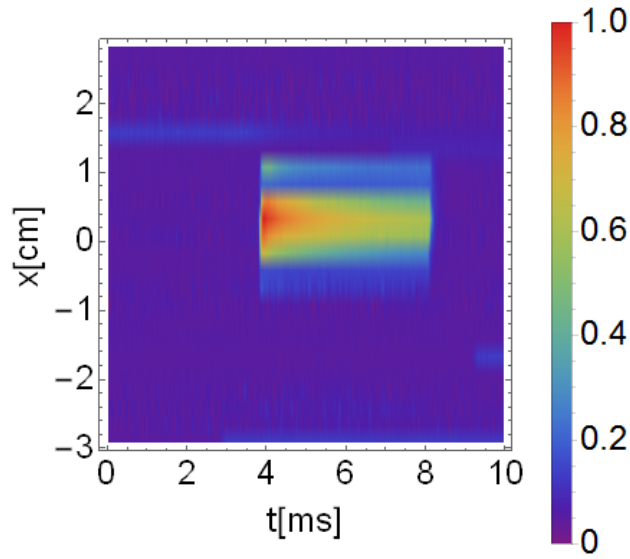

Figure 5.18: Beam profile measured at PR1: x-t plane.

At the position of PR1, where the dispersion function is almost zero (Fig. 5.15), it is impossible to obtain the longitudinal momentum deviation. This is confirmed by the experimental results of PR1 as shown in Fig. 5.18 in which the beam center along the longitudinal direction stays the same.

However, at the position of PR2, the dispersion function is more than $2\ m$, which indicates that 1% difference in momentum deviation will results in a 2 cm excursion of the beam center. The results of the quasi-3D beam profile measured with the new system at PR2 are shown in Fig. 5.20 and Fig. 5.21.

Fig. 5.20 shows that the front of the beam is bending towards the $-x$ direction while in the y-t plane, there exists no such observation because there is no dispersion for the vertical direction.
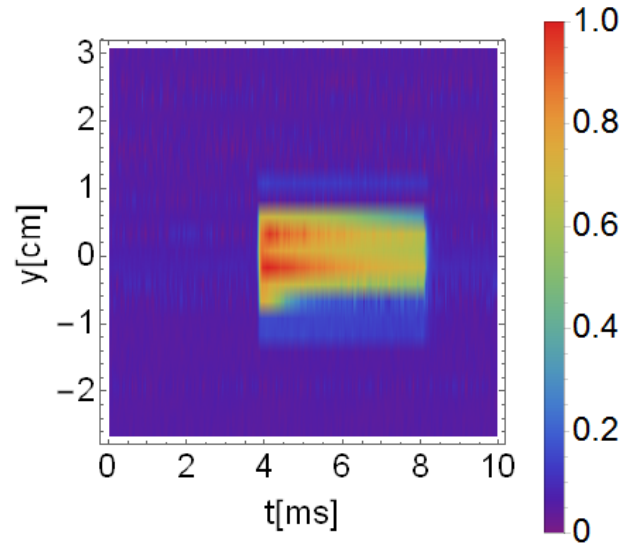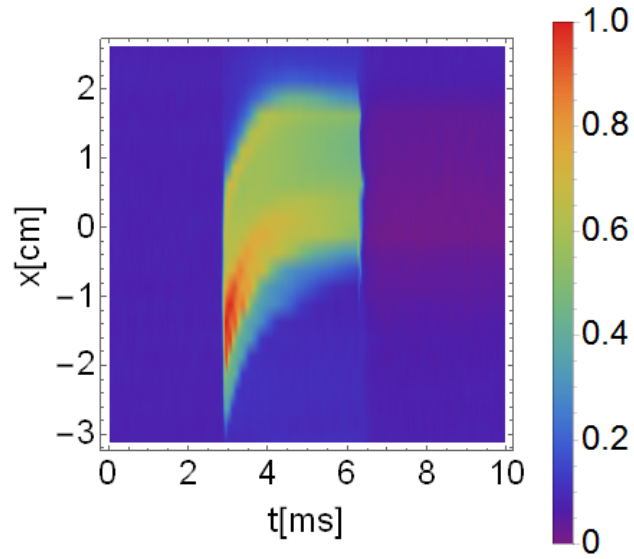
Figure 5.19: Beam profile measured at PR1: y-t plane.

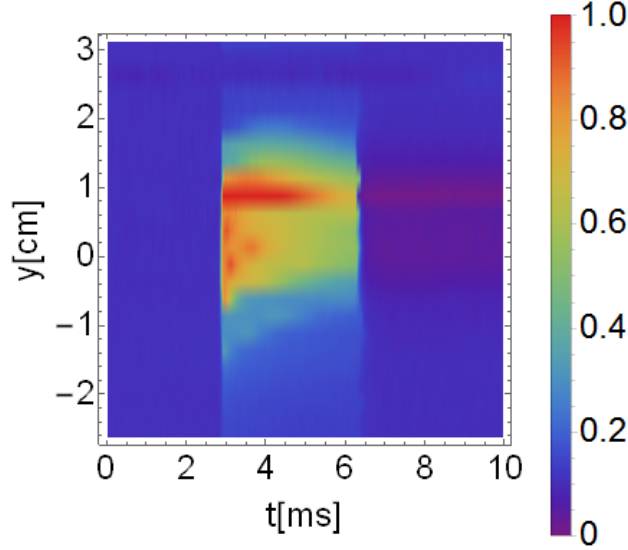Figure 5.20: Beam profile measured at PR2: x-t plane.

Figure 5.21: Beam profile measured at PR2: y-t plane.

In previous section, we measured the beam profiles at PR2 and PR4 to calculate the beam parameters at PR2. Fig. 5.20 shows that at PR2 and PR4 where dispersion function is relatively large, the beam profiles turn out to be strange in the horizontal direction (as can be seen in Fig. 5.6). Therefore, for experiment in previous study, it is better to be done in a dispersion free beam line.

Fig. 5.20 suggests that the front part of the beam has a larger momentum deviation, or higher energy than the beam rear part. The beam gains energy at two places before entering the LEBT line. The first one is the extraction gap of the ECRIS (see Fig. 3.4). The second one is the post-acceleration column (see Fig. 3.2).

From Figs. 5.18 to 5.21 in both horizontal and vertical directions, the beam size measured at PR2 is larger than that measured at PR1. Assume that the beam emittance is constant from PR1 to PR2, the beam size difference comes from the difference of the beta function at different locations, as suggested by Eq. (2.115).

Extraction region and its compensation

If the voltage between the cathode and anode changes during the process when the beam passes this gap, it will result in longitudinal energy difference of the beam. High voltage probe has been used to directly measure the voltage trend during the beam extraction process. The results are shown as in Fig. 5.22. The extraction voltage is

14 kV, when no beam generated from the ECRIS, this voltage is constant. However, when the beam is generated and extracted through the gap, this voltage will drop about 0.4 kV as shown in the figure. This phenomenon is called "beam loading effect".
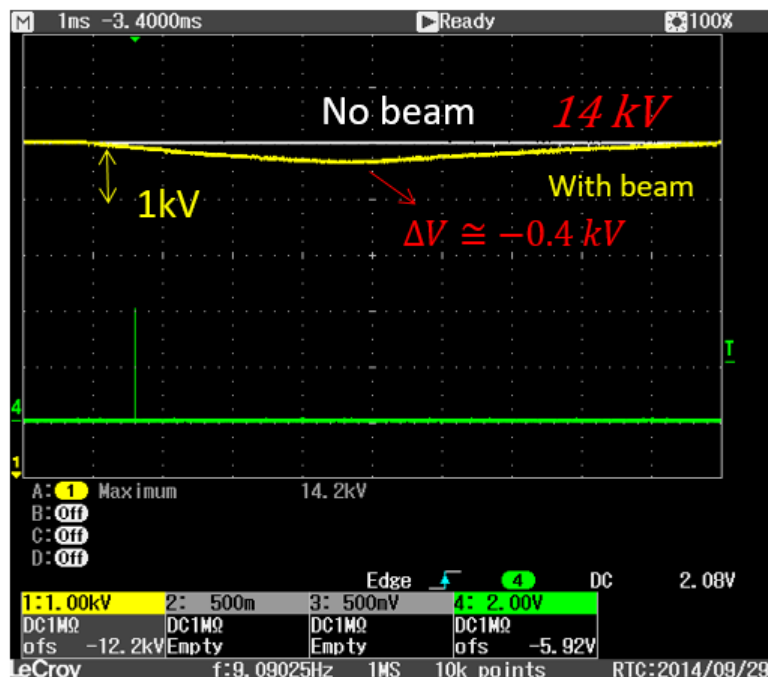

Figure 5.22: Beam loading effect in the extraction region of the ECRIS.

In order to compensate this effect, a simple circuit featuring capacitance has been added to stabilize the extraction voltage. We call this circuit a "stabilizer". After adding the stabilizer for the ECRIS, the beam loading effect has become negligible as shown in Fig. 5.23.

The equivalent circuit for ECRIS including the stabilizer is shown in Fig. 5.24. The simulation results with and without stabilizer are shown in Fig. 5.25. In the simulation the beam current intensity profile has been assumed to be the same as measured with FC1, which is also plotted.

With the stabilizer, the voltage drop is negligible as shown in the simulation result in Fig. 5.25. Even without the stabilizer, the energy difference is about 0.4 kV at most. However in Fig. 5.26, after adding the stabilizer, the front part of the beam still bends towards the $-x$ direction, though compared with Fig. 5.20, the bending amplitude is smaller. As discussed, the excursion of the center can be used
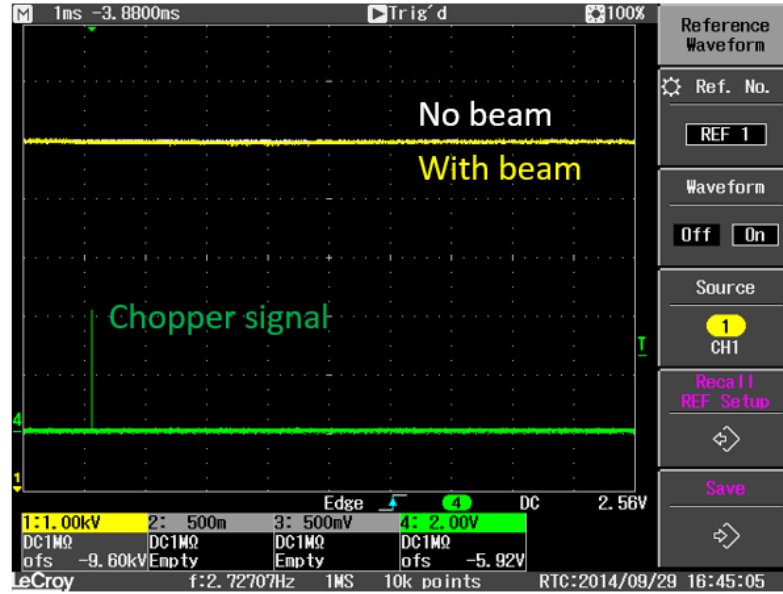
Figure 5.23: Beam loading effect compensated with the stabilizer.
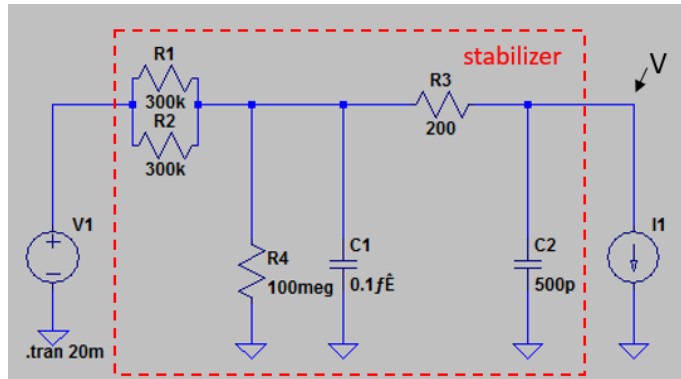
Figure 5.24: Equivalent circuit of ECRIS including stabilizer.
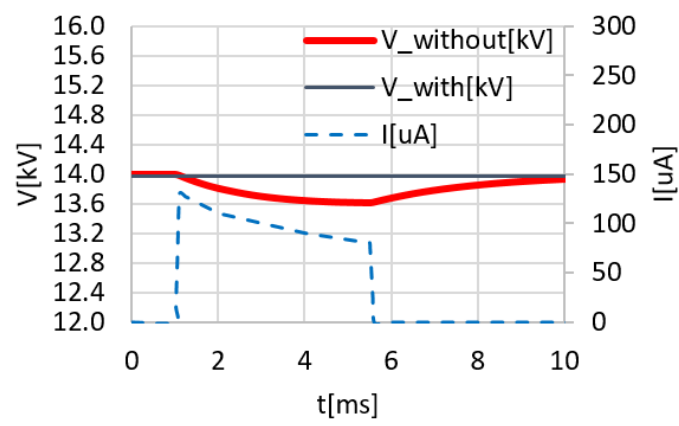
Figure 5.25: Simulation results of the ECRIS extraction region.

to evaluate the energy difference. A comparison of the beam center in Fig. 5.20 and Fig. 5.26 is compared in Fig. 5.27, in which the secondary vertical axis indicates the corresponding momentum deviation if we take the longitudinal middle of the beam as reference. Fig. 5.27 suggests that there exists another source and it contributes more to the longitudinal beam energy difference.
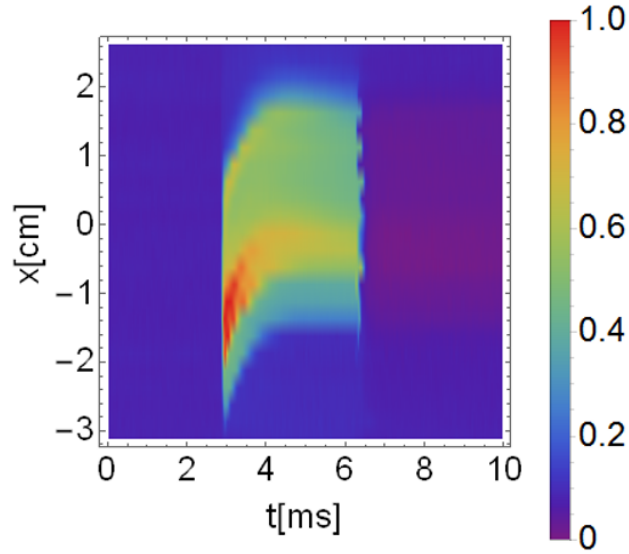
Figure 5.26: Beam profile measured at PR2, ECRIS with stabilizer.
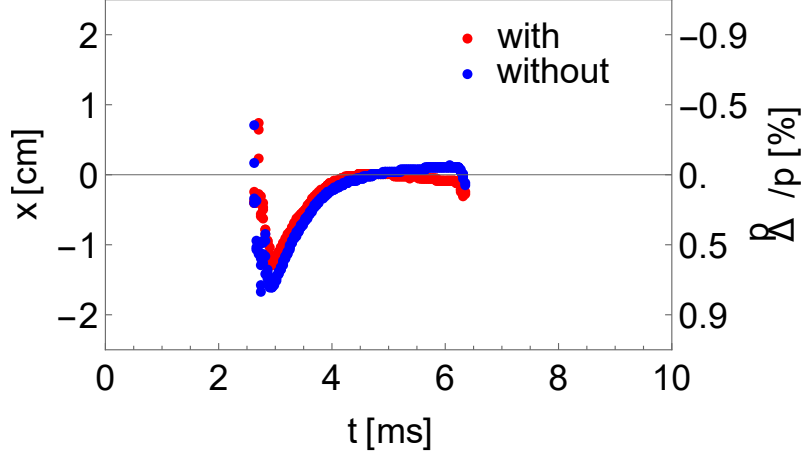
Figure 5.27: Comparison of the beam center in Fig. 5.20 (without stabilizer) and Fig. 5.26 (with stabilizer).

Post-acceleration region

Unfortunately, it is difficult to directly measure the voltage trend for the 186 kV high voltage on the post acceleration column as we did for the extraction voltage. But the beam loading effect at this region can be studied through electrical circuit simulation. From the discussion of the beam loading effect at the extraction region, the simulation results have a good agreement with the experimental results. Fig. 5.28 shows the equivalent circuit of the HVT. Fig. 5.29 shows the simulation result, which indicates that the voltage drop when the beam pass this region is about 1 kV.
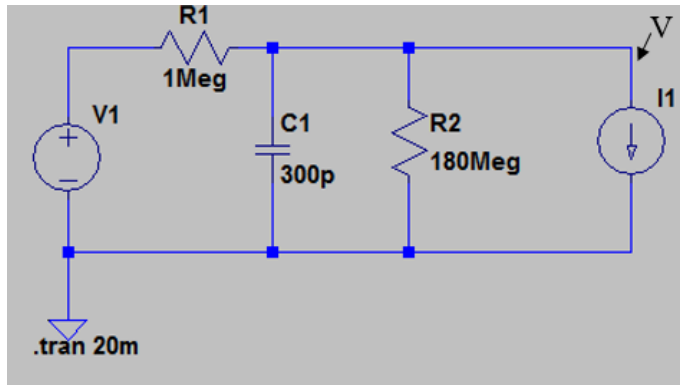
Figure 5.28: Equivalent circuit for the present HVT.
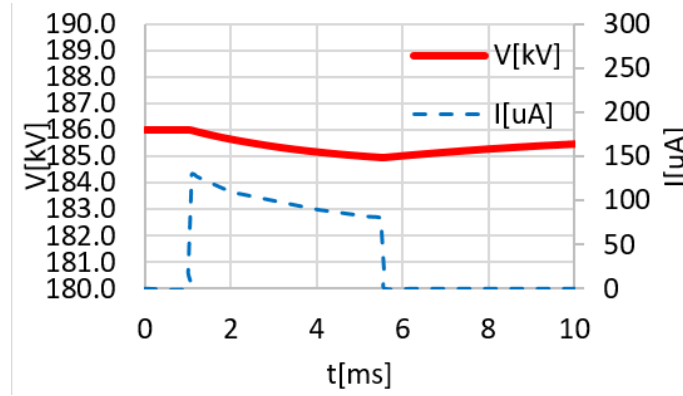
Figure 5.29: Voltage drop in the post-acceleration column region with simulation.

A stabilizer circuit has been used to compensate the beam loading effect in the ECRIS extraction region. Fig. 5.30 gives a possible solution for the same purpose and its simulation result shows that it can suppress the voltage drop to less than 20 V, which is negligible.
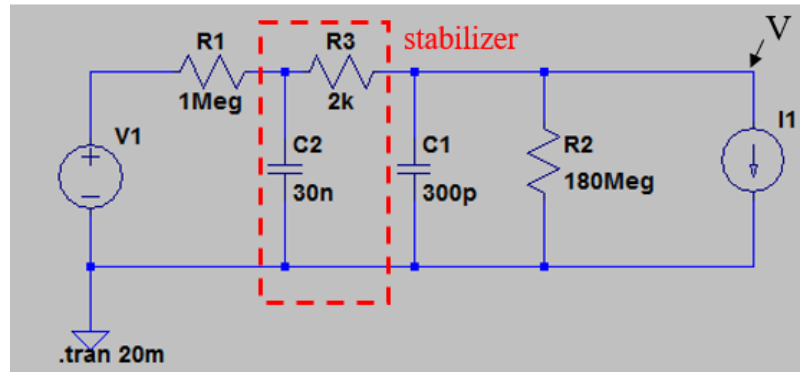
Figure 5.30: Possiple circuit for the post-acceleration column.

With beam parameters from Table 5.4, the relationship between voltage difference and the resulted momentum deviation can be calculated. The calculation result is compared with the experimental results in Fig. 5.31. Two experimental data points are plotted in this figure, the momentum deviations are taken from Fig. 5.27 and the voltages are 1.05 kV and 1.45 kV respectively, corresponding to the two cases with and without stabilizer.
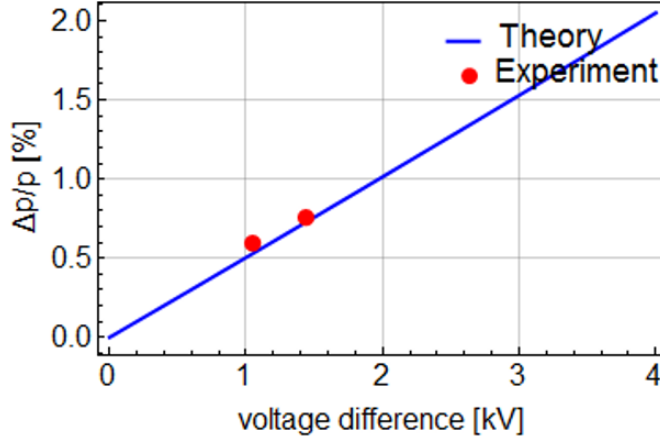
Figure 5.31: Momentum deviation in terms of the voltage difference.

5.2.4   Short beam and Einzel Lens Chopper

Results from the profile monitors

The short beam, which is 4 µs long, was also measured with the profile monitors. Fig. 5.32 and Fig. 5.33 show the measurement results at PR2 for the x-t plane and y-t plane, respectively.

Fig. 5.32 shows that the beam head shifts towards the $+x$ direction and the beam tail the $-x$ direction. This observation indicates that beam head and beam tail have inversed momentum deviations to the main body of the beam. Fig. 5.34 is a plot of the center and momentum deviation for the x-t plane in Fig. 5.32, which shows that the beam head has a momentum deviation larger than 0.5% and the beam tail has one less than 0.5%.

It has to be pointed out that the momentum deviations obtained here are smaller in absolute amplitude than the actual values. This is because that the peaks appearing at the beam head and beam tail are very sharp, so the calculation for center may not be so accurate. Especially for the peak at the beam head, the signals at its end are very low because of the small beam intensity there.

Einzel Lens Chopper

For the long beam of several milliseconds long, the beam loading effects in the extraction region and the post-acceleration column have caused the momentum deviation along the longitudinal direction within the beam. Notice that the short
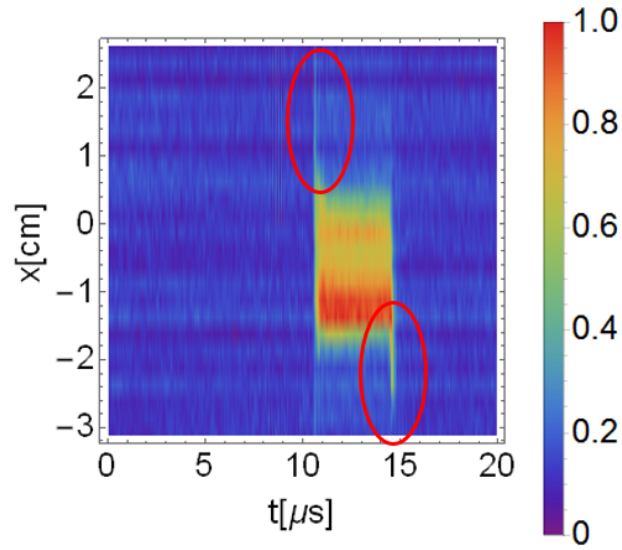
Figure 5.32: Beam profile measured at PR2: horizontal, peaks at the beam head and tail.

.
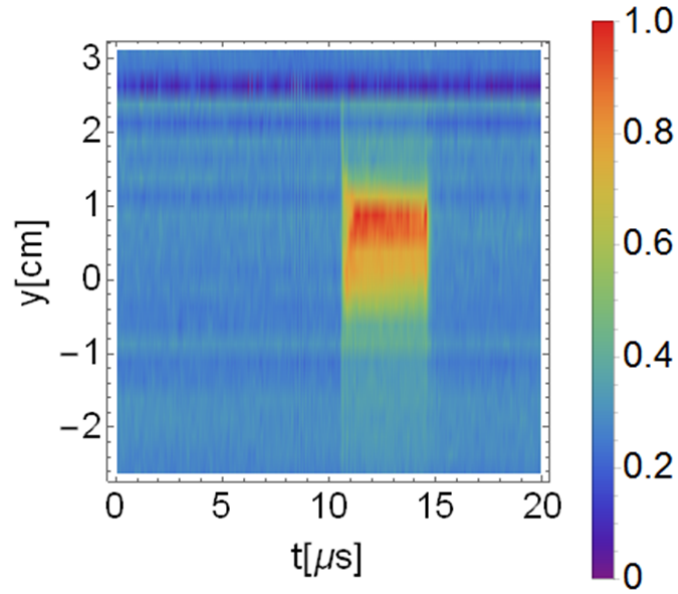
Figure 5.33: Beam profile measured at PR2: vertical.
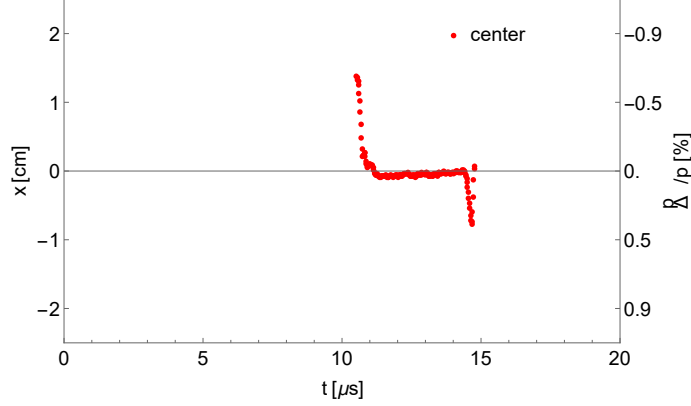
Figure 5.34: Center and the corresponding momentum deviation for the short beam.

beam is chopped out from the long beam by the Einzel Lens Chopper working as a longitudinal chopper, which is installed after the ECRIS (Fig. 3.4). The stabilizer has been added to compensate the beam loading effect at the extraction gap. Even without the compensation, voltage difference within several microseconds is negligible. As a result, the beam loading effects at the extraction region and the post-acceleration are not the source of the momentum deviation here. Moreover, the shift direction at the beam head in Fig. 5.32 is different from the bending direction in Fig. 5.20 or Fig. 5.26.

In fact, the momentum deviations at the beam head and beam tail are due to the Einzel Lens Chopper (Sec. 3.2.3) which has been discussed in Chapter 4. The behavior of the Einzel Lens Chopper working as a chopper has been well studied by Leo [20, 22]. They are resulted from the chopping process of the Einzel Lens Chopper.

A particle tracking simulation including the transitional processes have been done by Leo [22] and its result of the momentum deviation within the beam at the end of the LEBT line is shown in Fig. 5.35. In terms of the momentum deviations of the beam head and tail, the simulation is in good agreement with the experimental result in Fig. 5.34, where the momentum deviation is on the secondary axis and has inversed axis labels).

5.2.5   Further discussion

For the long beam, the beam loading effects at the ECRIS extraction region and the post-acceleration column contribute to the longitudinal momentum deviation. The high voltage measurement and electrical circuit simulation both confirmed the beam loading effect at the ECRIS extraction region. A stabilizer have been used
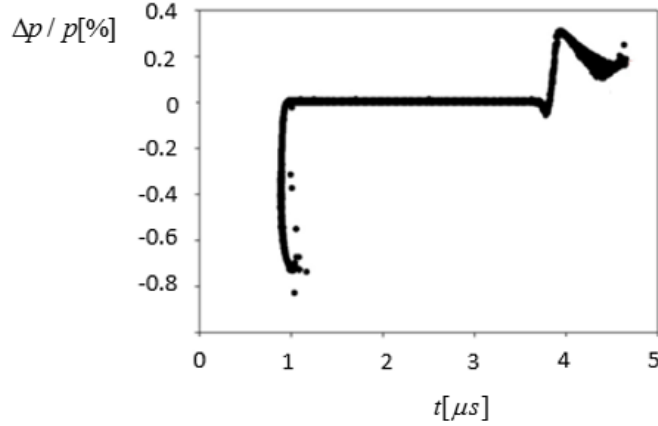
Figure 5.35: Longitudinal phase space distribution at the end of LEBT line by simulation.

to compensate the beam loading effect at this region. The beam loading effect on the post-acceleration column have also been confirmed with simulation and a compensation circuit design was provided. For the short beam, the momentum deviation is caused by the Einzel Lens Chopper when it is used to chop the beam, the momentum deviation evaluated from the results of the profile monitor is well consistent with the result of the particle tracking simulation.

With the quasi-3D profile monitor located at a position with a proper dispersion function value, it was shown that the longitudinal momentum deviation can be evaluated experimentally. But the lack of single shot capture ability caused difficulty. The data acquisition time was very long. For a single quasi-3D profile, it takes two minutes. Although, the stability of the ECRIS and the LEBT is not a problem in this experiment. The best way to capture the beam profile is to measure all the channel signals at the same time to take a single shot beam profile. This can be realized with a signal-processing unit that consists of a sufficient number of analog-to-digital converters (ADC) to convert all the signals to digital signals and transfer them to the PC for further processing.

5.3 Summary

In this chapter, two experimental studies on the beam parameters have been discussed. The profile monitor played a key role in both the studies.

100

In th firs study, the experimental method to measure the beam parameters like Courant-Snyder parameters and beam emittance by changing the focusing strength of the quadruple magnets has been conducted. In addition to the present experimental conditions, such as the lack of the excitation characteristics of individual magnets and the precision of the profile monitor, the coupled motion in such a dispersive system makes it difficult to fitting the beam profile. Due to these reasons, the original motivation to obtain optics matched to the main ring was found not easy to achieve. However, the results obtained here, especially the beam emittance in both directions, are important parameters to analyze the beam at the LEBT region. More experimental work based on these techniques and results needs to be done on this region.

In the second study, the longitudinal momentum deviations within the beam for a 4 ms long beam and a 4 µs short beam has been evaluated with the measurement results of the quasi-3D profile monitor, which has been newly developed based on the multi-wire grid profile monitor. The reasons for the momentum modulations have been successfully identified and confirmed through the experimental observations and simulations.

Chapter 6

3D Tracking Simulation for Induction Synchrotron and Space Charge Solver

6.1   Brief review and motivation

Many beam commissioning studies have been conducted in the KEK-DA. However, the simulation work for various purposes stayed mainly in the longitudinal beam motion. For example, Shimosaki developed a code to study the effects of the droop observed in an induction pulse [25]; Dixit wrote one to propose the "pulse density control" scheme which is still adopted at presen as described in Chapter 2, t. These simulation works are very helpful and important in the early studies for the induction synchrotron.

   With the results from the beam commissioning, more precise simulation work was necessary to understand the beam behavior, even for the study of the longitudinal motion. Leo has developed a particle tracking code to understand the peak formation at the bunch head and tail including space charge effects [20, 22]. I have also developed a code with longitudinal space charge effect with an FFT method to study the beam evolution in the ring [26, 27]. These simulation studies was found useful to explain their specific phenomena.

   The injection energy for the induction synchrotron is very low. In case of He^{1+}, the relativistic β is as low as 0.01. In case of Ar^{3+}, $\beta \approx 0.006$. Though, the latter case has a mass-charge-ratio $A/Q \approx 13$, which makes it suffer less from the space charge compared to the former one which has $A/Q = 4$.

   In order to completely understand the beam behavior, especially the beam loss in

the KEK-DA ring, a more complete particle code is necessary. For this purpose, an exclusive 3D tracking code (6D in phase space) with space charge for an induction synchrotron has been developed. This is the first time that a particle tracking code has been developed for the induction synchrotron. It is not only meaningful to understand the beam motion in the KEK-DA from the view point of the fundamental beam dynamics, but also helpful to study the beam behavior under different commissioning conditions. Specifically, identifying the beam loss mechanism with simulation in present KEK-DA will help for the design of the future induction synchrotrons.

In this chapter, the simulation code will be described. A sub-3D space charge solver with boundary matrix and iterative method will also be described and justified.

6.2 3D tracking simulation

6.2.1 Tracking scheme with space charge

In Chapter 2, the transfer matrices for various common component in a beam line has been introduced. In the simulation, the 6D phase space of the particle distribution is updated with the transfer matrices for a small step ds. The dynamical variables for the particle has been chosen as,

$$\mathbf{x} = (x, xp, y, yp, z, \Delta p/p) \tag{6.1}$$

Where (x, xp) and (y, yp) are the horizontal and vertical phase space respectively. $(z, \Delta p/p)$ is the longitudinal phase space, where $z = s - \beta_0 c \cdot dt$,($\beta = \frac{v_0}{c}$ is the velocity of referential particle and c is the light speed) is the particle's longitudinal distance from the referential particle and $\Delta p/p$ is the momentum deviation from the referential particle. In the calculation of space charge force with particle-in-cell method, (x, y, z) which is the position of a macro particle, $(z, \Delta p/p)$ is chosen instead of $(dt, \Delta p/p)$ for the longitudinal coordinates. Another reason to choose z instead of dt is that the transfer matrix in z is simpler than in terms of dt.

The transfer matrix in Eq. (2.76) is used for the drift space, Eq. (2.93) is used for combined function type bending magnets, and Eq. (2.96) is used for the quadrupole magnets.

For particle tracking without space charge from s_1 to s_2, the change of particle's information defined in Eq. (6.1) is given by,

$$x_{s_2} = M_{s_1 \to s_2}.x_{s_1} \tag{6.2}$$

where M is a 6×6 transfer matrix from s_1 to s_2 . In order to include the space charge as non-linear effects and keep the simplicity of Eq. (6.2), the one kick approximation

is used [28],

$$\mathbf{x}(s)\xrightarrow{K_{sc}}\mathbf{x}(s)'\xrightarrow{M}\mathbf{x}(s+\Delta s) \tag{6.3}$$

Where K_{sc} is the kick due to space charge and $\Delta s = s_2 - s_1$. K_{sc} can be expressed with the space charge field as [29],

$$\vec{x}_{sc} = (0, \frac{\Delta s \cdot Qe}{\gamma_0{}^2 p_0 \beta_0 c}E_x, 0, \frac{\Delta s \cdot Qe}{\gamma_0{}^2 p_0 \beta_0 c}E_y, 0, \frac{\Delta s \cdot Qe}{\beta_0{}^2 E_{total}}E_z) \tag{6.4}$$

This process can be illustrated as shown in Fig. 6.1.
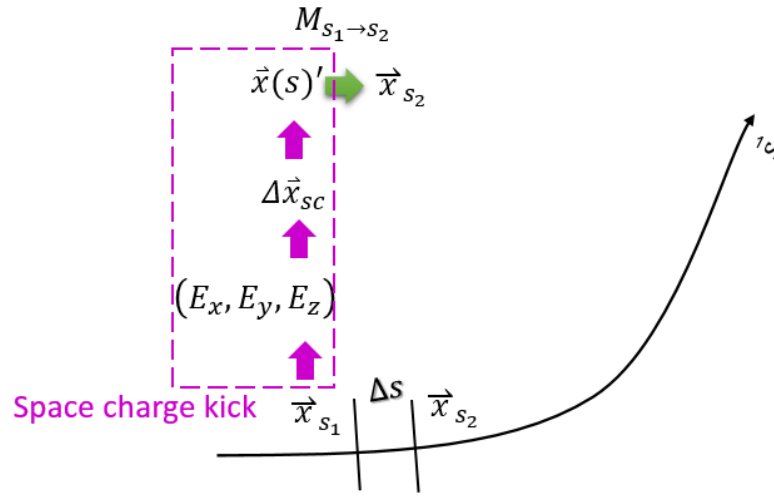
Figure 6.1: Particle tracking for a small step size ds.

It is assumed that during a very small step size of Δs , the change of the space charge field from the beam distribution is ignorable. In Eq. (6.4), (E_x, E_y, E_z) is the electric field in beam frame, Q is the charge state of the particle, e is the electron charge, $\gamma_0 = 1/\sqrt{1-\beta_0^2}$, p_0 is the referential momentum and E_{total} is the total energy of the referential particle. The magnetic field due to moving beam has been considered by including $1/\gamma_0^2$.

6.2.2 Simulation mode

The definition of the simulation mode is expressed in Table 6.1 based on the settings of the induction cells and the magnetic field. "Mode 0" is used for lattice calculation without particle tracking, which calculates the Courant-Snyder parameters in the ring.

"Mode 1" corresponds to the beam free run or barrier bucket confinement under the static magnetic field ("DC" for "Magnetic Field"). Usually, the barrier bucket voltage pulses (V_{bb}) are applied every turn and their settings don't change from turn to turn. "Mode 2" corresponds to the particle tracking under the ramping magnetic field, in which both the V_{bb} and V_{acc} are required. Considering that the revolution period of the reference particle will change for every turn under this mode, the settings for the V_{bb} and V_{acc} are different for each turn. In addition, "pulse density control" has to be considered at present so additional table files including these turn-by-turn information are necessary.

Table 6.1: Simulation mode.

Mode	Induction Cell	ON/OFF	Table ON/OFF	Magnetic Field
0	V_{bb}	0	0	None
	V_{ac}	0	0	
1	V_{bb}	0/1	0	DC
	V_{ac}	0	0	
2	V_{bb}	1	1	AC
	V_{ac}	1	1	

Notice that the beam distribution is unnecessary in the Mode 0, so only in Simulation Mode 1 and Simulation Mode 2 the beam distribution will be imported.

6.2.3 Element-wisely tracking

The beam evolution in the ring is simulated in an element-wisely way. At the very beginning, an element list is imported by the program. At present, the following element types are considered in the simulation.

1). *Drift*: with length, strait section where no magnetic field exists.

2). *Bend*: with length, including pure dipole magnet and combined function type as used in the KEK-DA ring. The dipole coefficient(k_0) and quadrupole coefficient(k_1) are required to define such a magnet.

3). *Quad*: with length, quadrupole magnet. k_1 is required to define such a magnet.

4). *Inductioncell*: special element without length, used to kick the particle distribution with pre-defined voltage pulse. External table with pulse density control can be imported in Simulation Mode 2.

5). *Monitor*: used to record the beam information when particle pass through it.

In a general sense, the element concept is designed to stand for the real object used in an accelerator system. However, there are several cases a real object should be treated as a collection of several elements in the simulation.

For example, the injection kicker and extraction kicker, which are usually installed in a strait section, are not supported in the present simulation code so that they are treated simply as *Drift* element. However, as they have different shapes of the cross section apart from other straight sections, they should be treated as individual elements in the simulation. Namely, *Drift* element with different shapes.

Another special case is the combined function type magnets used in the KEK-DA ring. The boundary shape of the vacuum pipe in the magnet stays the same. However, the combined function type magnets are separated into different sections due to the different magnetic field configuration, as can be seen in Fig. 3.16. Specifically, the k-value for the dipole coefficient (usually noted as k_0) and quadrupole coefficient (k_1) are different in each section. As a result, these sections should be treated as different element with different k-values.

The real object like the *Inductioncell* and *Monitor* are assumed to be zero length. Thus they will separate the straight section into several elements when adopted.

In general, whenever the magnetic field configuration or the boundary shape is different or a special purpose element is introduced, they should be treated as individual elements in the simulation.

Details of the element definition can be found in Appendix A.

6.2.4   Structure of the simulation

The flow chart of the simulation program is shown in Fig. 6.2. All the external files with varies settings are imported at the beginning. The simulation then will be continued based on the simulation mode (*Mode* in Fig. 6.2) specified in imported setting file.

For each turn, the beam is tracked through every element, which is divided into small segments based on the specified step size (ds). Note that the ds does not have to be the integer divisions of the element length, so the remnant part rs is calculated

107

separately. In case the element length is less than ds, the element length will be used. After finishing the tracking, the simulation comes to the end.
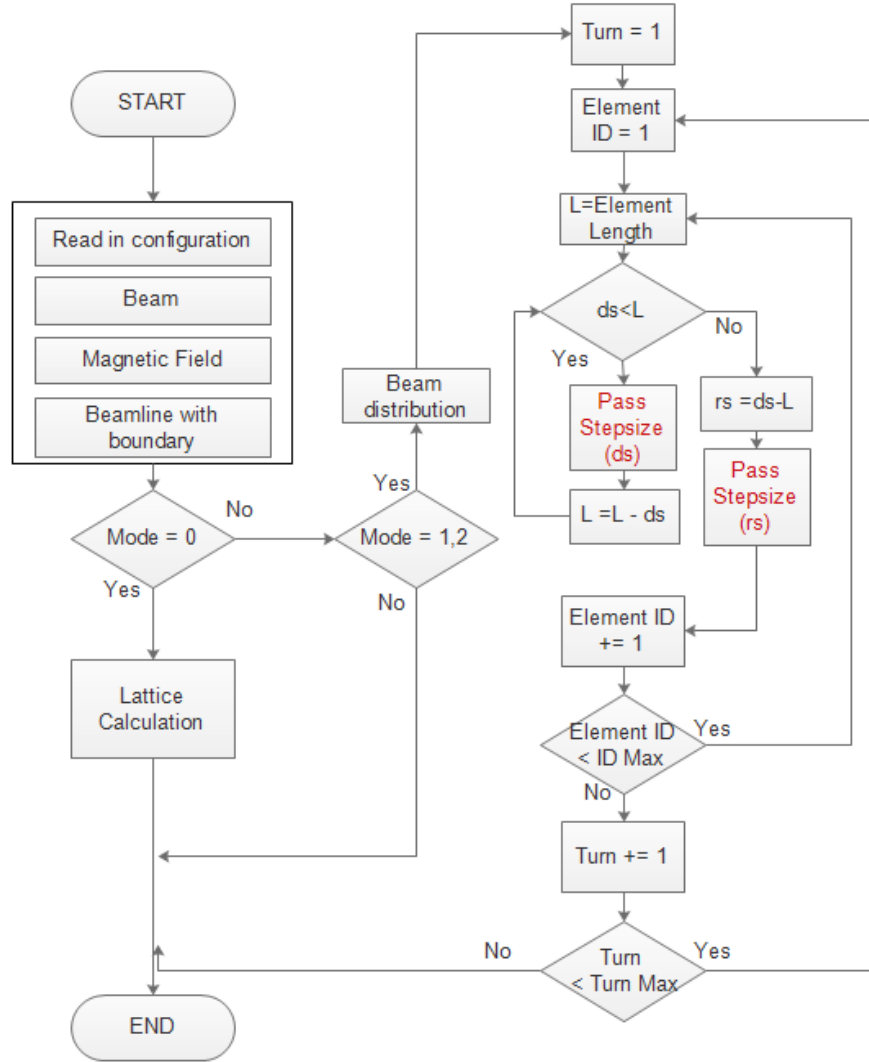

Figure 6.2: Flow chart of the simulation.

The flow chart for a small step size (ds or rs) is shown in Fig. 6.3
In Fig. 6.3, the three subroutines correspond to:

1). "Synchronize with magnetic field": In Simulation Mode 2, where the magnetic field is changing, the information of the referential particle and
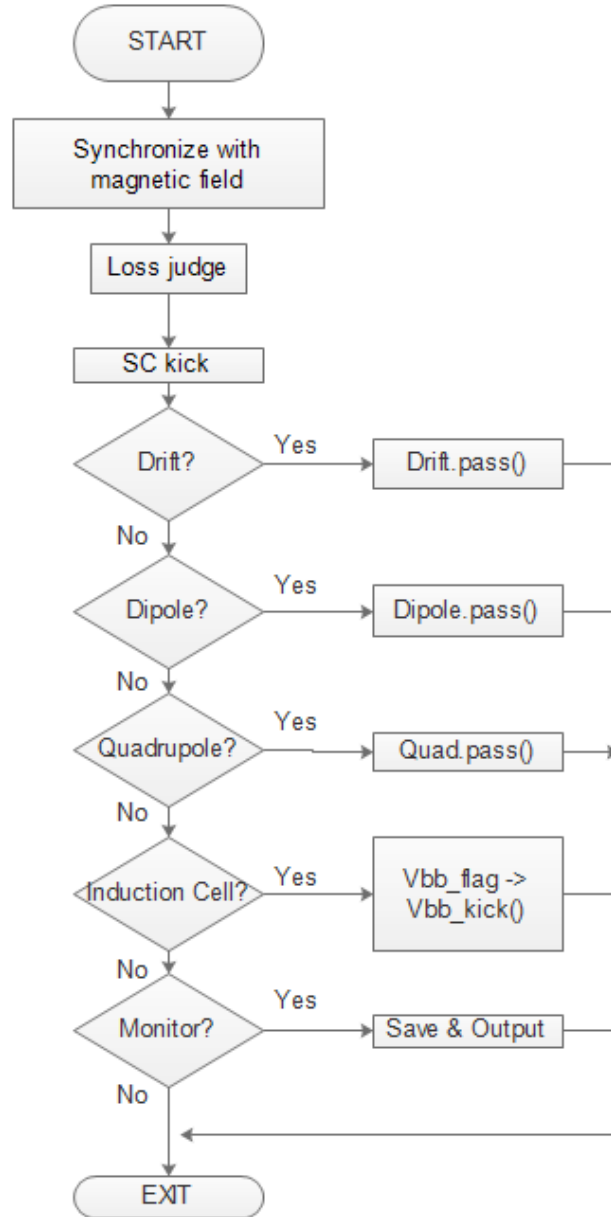
Figure 6.3: Flow chart of "Pass Stepsize" in Fig. 6.3, ds or rs.

thus the distribution of the beam should be changed accordingly. As the magnetic field is increasing, the momentum of the reference particle should be increased to synchronize with the magnetic field.

2). "Loss judge": Before each step, update the particle survival information with the local boundary.

3). "SC kick". Calculate the potential distribution with present beam distribution then apply the space charge kick to the beam distribution.

For each step, the action applied on the beam will depend on what type of the element is. For example, if the element is $Drift$ or magnets such as $Bend$ and $Quadrupole$, corresponding functions will be called to calculate the transfer matrix then to update the beam distribution. The transfer matrices for common components have been given in Eqs (2.76), (2.93) and (2.96). If the element is a special element such as induction cell where the beam are affected by a voltage pulse, then the beam distribution will be updated with this voltage pulse. The beam information is stored in the $Monitor$ element for output as mentioned.

6.3 Space charge solver

The goal of a space charge solver is to simulate the particle interaction between particles inside a beam. In the free space, this is a $N - body$ problem which can be directly solved by the particle to particle interaction for all the particles.

Simulation of the interaction between each particle in a beam due to Coulomb force is such a typical N-body problem similar to the interaction between different planets due to the gravitational force in astronomy. If we assume a bunch of charged particles are distributed in a free space, the interaction between particles due to the coulomb force can be calculated directly with Coulomb's Law. This is usually very time-consuming given that its computation complexity is N^2, assuming N is the number of the particles. Typically, in the accelerator field, for a beam bunch, the number of the particles can range from 10^8 to 10^{12}.

Of course the macro particle method which uses a single macro particle to represent a group of particles are widely adopted in modern simulation. Even so, the number of macro particles should be 10^4 to 10^6, greatly reduced from the actual number but still time consuming. Parallel computing can be applied to this problem to reduce the computation time.

The more effective way is to reduce the computation complexity. For this purpose, techniques like tree code method (complexity $O(N \log N)$) and the fast multipole

method (FMM, with complexity $O(N)$) are developed [30]. As an example, Shimosaki has adopted the idea of tree code method for his simulation work [31]. As a general rule, these methods reduce the computation complexity by increasing the code complexity. Furthermore, method with multipole expansion such as the tree code method and FMM requires additional handling on the boundary or image charge [32]. In a system like in accelerator where the beam distribution has to be updated for a small step size along a beam line or most of the cases, in a ring where the beam is tracked for many turns, the speed of the solver is crucial for an applicable simulation.

In case that the beam size is much smaller than the size of the cross section, due to the fact that the electric potential will drop quickly outsize of the beam, the potential induced by the beam has little difference with or without boundary. However, in the case of the induction synchrotron which features low energy injection and wide band acceleration as discussed in Chapter 2, the beam size is comparable to the vacuum chamber's cross section. For example, in the KEK-DA ring, the beam size is typically several centimeters and some at some locations, the aperture size is rather limited). As a result, the space charge solver for the simulation of an induction synchrotron should consider the shape of the vacuum chamber.

Another reason to include the boundary is that it can be used to judge the particle loss. With the module in the simulation code to record the position and time when the particle get lost by hitting the boundary, it is easy to identify the reasons of the beam loss.

In this simulation, we adopted a slice scheme and iterative method to solve for the potential induced by the beam with arbitrary boundary shape.

6.3.1 Finite difference method for Poisson's equation

In general, Poisson's equation is,

$$\nabla \phi = -\frac{\rho}{\varepsilon_0} \tag{6.5}$$

where ϕ is the potential induced by the particle distribution, ρ is the charge density and ε_0 is the electric constant. In 3D Cartesian coordinates, explicitly, it looks like,

$$\frac{\partial^2 \phi(x,y,z)}{\partial x^2} + \frac{\partial^2 \phi(x,y,z)}{\partial y^2} = -\frac{\rho(x,y,z)}{\varepsilon_0} - \frac{\partial^2 \phi(x,y,z)}{\partial z^2} \tag{6.6}$$

where the z-component is moved to the right hand side (r.h.s) in Eq. (6.6).

Finite difference method can be applied as a numerical way to solve the Poisson's equation. For example, by applying the central difference approximation of the second derivative of the potential $\phi(x,y,z)$, individual items related to the potential are,

111

$$\frac{\partial^2 \phi(x,y,z)}{\partial x^2} \approx \frac{\phi(\mathrm{x}+\Delta \mathrm{x}, \mathrm{y}, \mathrm{z}) - 2\phi(x,y,z) + \phi(x - \Delta \mathrm{x}, \mathrm{y}, \mathrm{z})}{(\Delta \mathrm{x})^2}$$

$$\frac{\partial^2 \phi(x,y,z)}{\partial y^2} \approx \frac{\phi(x, \mathrm{y}+\Delta \mathrm{y}, z) - 2\phi(x,y,z) + \phi(x, y - \Delta \mathrm{y}, \mathrm{z})}{(\Delta y)^2} \qquad (6.7)$$

$$\frac{\partial^2 \phi(x,y,z)}{\partial z^2} \approx \frac{\phi(x, \mathrm{y}, \mathrm{z}+\Delta z) - 2\phi(x,y,z) + \phi(x, \mathrm{y}, \mathrm{z}-\Delta z)}{(\Delta z)^2}$$

where Δx and Δy are the horizontal and vertical grid size in Fig. 6.4, respectively. They depend on the boundary size and grid number m and n. Δz is the longitudinal grid size which should be determined by the beam length and the grid number k.

In addition, when $\Delta x = \Delta y = \Delta$, Eq. (6.7) can be expressed as,

$$\phi(x + \Delta, y, z) + \phi(x, y + \Delta, z) - 4\phi(x,y,z) + \phi(x - \Delta, y, z) + \phi(x, y - \Delta, z)$$
$$= -\frac{\rho(x,y,z)}{\varepsilon_0}\Delta^2 - \rho^*(x,y,z)$$

$$(6.8)$$

where $\rho^*(x,y,z)$ can be treated as a modification term,

$$\rho^*(x,y,z) = (\phi(x, \mathrm{y}, \mathrm{z}+\Delta z) - 2\phi(x, \mathrm{y}, \mathrm{z}) + \phi(x, \mathrm{y}, \mathrm{z}-\Delta z))(\frac{\Delta}{\Delta z})^2 \qquad (6.9)$$

This modification term is related to the potential change in the z direction and proportional to $\frac{\Delta}{\Delta z}$. In the case of the bunch in an induction synchrotron, the longitudinal beam size is much larger than the transverse. As a result, Δ is usually much less than Δz.

After getting the potential profile, the electric field can be simply calculated as,

$$E_x = -\frac{\partial \phi(x,y,z)}{\partial x}$$
$$E_y = -\frac{\partial \phi(x,y,z)}{\partial y} \qquad (6.10)$$
$$E_z = -\frac{\partial \phi(x,y,z)}{\partial z}$$

6.3.2 Charge density: Particle-In-Cell method

In order to solve for the potential $\phi(x,y,z)$ in Eq. (6.8), the charge density has to be calculated. Particle-In-Cell(PIC) method has been adopted to obtain the charge

density on the 3D grid. The charge of the macro particle will be assigned to its closest grid points (eight points/vertices for each macro particle) with the Particle-In-Cell method, where the distances from the particle's position to the grid points are treated as weighting coefficients. For example, a macro particle with at position (x, y, z) with charge q will be assigned to the closest eight grid points as shown in Eq. (6.11).

$$
\begin{cases}
q(i, j, k)+ = (1 - \xi_x)(1 - \xi_y)(1 - \xi_z) \cdot q(x, y, z) \\
q(i + 1, j, k)+ = \xi_x \cdot (1 - \xi_y)(1 - \xi_z) \cdot q(x, y, z) \\
q(i, j + 1, k)+ = (1 - \xi_x) \cdot \xi_y \cdot (1 - \xi_z) \cdot q(x, y, z) \\
q(i + 1, j + 1, k)+ = \xi_x \cdot \xi_y \cdot (1 - \xi_z) \cdot q(x, y, z) \\
q(i, j, k + 1)+ = (1 - \xi_x)(1 - \xi_y) \cdot \xi_z \cdot q(x, y, z) \\
q(i + 1, j, k + 1)+ = \xi_x \cdot (1 - \xi_y) \cdot \xi_z \cdot q(x, y, z) \\
q(i, j + 1, k + 1)+ = (1 - \xi_x) \cdot \xi_y \cdot \xi_z \cdot q(x, y, z) \\
q(i + 1, j + 1, k + 1)+ = \xi_x \cdot \xi_y \cdot \xi_z \cdot q(x, y, z)
\end{cases}
\tag{6.11}
$$

in which the weighting coefficient for horizontal direction is defined as,

$$
\xi_x = (x - x_i)/\Delta x
\tag{6.12}
$$

where x_i is the grid point's horizontal coordinate and Δx is the box size. ξ_y and ξ_z can be defined similarly.

6.3.3 Slice scheme

A slice scheme, as shown in Fig. 6.4 is chosen to solve the space charge potential induced by the beam. In this scheme, the particle distribution is longitudinally divided into k slices as in Fig. 6.4. Each slice is meshed into $m \times n$ squares. Thus, there are $m \times n \times k$ boxes in 3D space. The charge density on each grid point is obtained with the 3D PIC method described in previous section.

For the time being, let's assume that the modification term $\rho^*(x, y, z) = 0$, then at each slice shown in Fig. 6.5, Eq. (6.8) is reduced to be a 2D case, namely(with notation of z omitted for clearance),

$$
\begin{aligned}
&\phi(x + \Delta, y) + \phi(x, y + \Delta) - 4\phi(x, y) + \phi(x - \Delta, y) + \phi(x, y - \Delta) \\
&= - \frac{\rho(x,y)}{\varepsilon_0} \Delta^2
\end{aligned}
\tag{6.13}
$$

By solving the potential profile on each slice, we get a 3D potential distribution of the beam.
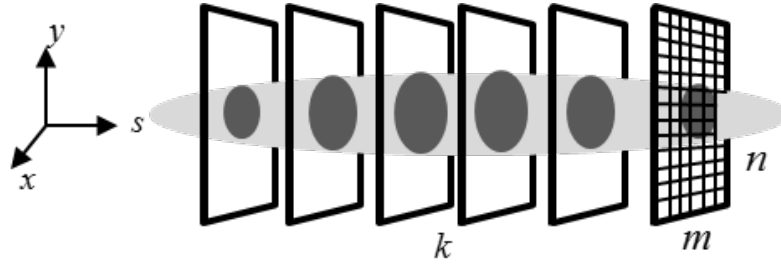
Figure 6.4: Slice scheme for solving beam induced space charge potential.

6.3.4   Boundary matrix method for a single slice

For a single point on the 2D grid, Eq. (6.13) can be seen clearly in Fig. 6.5.
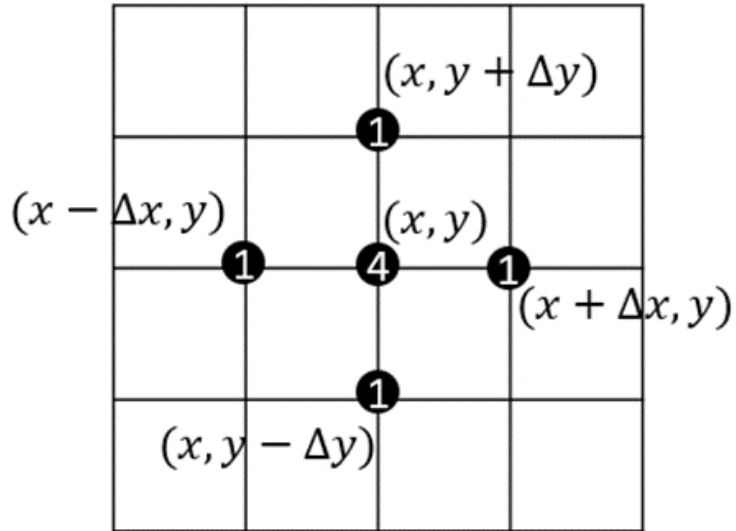

Figure 6.5: Finite method for Poisson's equation.

If the equations similar to Eq. (6.13) are written down for all points in Fig. 6.5, these equations will form a linear system with the left hand side (l.h.s) to be the potential on each grid point and the r.h.s to be the charge density, as shown below.

114

$$
\begin{pmatrix}
-4 & 1 & & & 1 & & & & & \\
1 & -4 & 1 & & & 1 & & & & \\
& 1 & -4 & 1 & & & 1 & & & \\
& & 1 & -4 & & & & 1 & & \\
& \vdots & & & \ddots & & & & \vdots & \\
& & & & & -4 & 1 & & & \\
& & & & & 1 & -4 & 1 & & \\
& \cdots & & \cdots & & & 1 & -4 & 1 & \\
& & & & & & & 1 & -4 & \\
\end{pmatrix}
\begin{pmatrix}
\phi_1 \\
\phi_2 \\
\\
\vdots \\
\\
\\
\phi_{n-1} \\
\phi_n
\end{pmatrix}
=
\begin{pmatrix}
\rho_1 \\
\rho_2 \\
\\
\vdots \\
\\
\\
\rho_{n-1} \\
\rho_n
\end{pmatrix}
\cdot \frac{\Delta^2}{\varepsilon_0}
$$

$$(6.14)$$

In the case of the perfect conducting boundary, the potential on the chamber surface is set to be zero. This boundary condition is included in the process of building this sparse matrix. For those points on the boundary or outside of the boundary, the corresponding terms in the matrix are simply set to be zero. As a result, the boundary matrix method can be applied to arbitrary cross section shapes.

Further observation indicates that the symmetric sparse matrix on the l.h.s of Eq. (6.14) is only related to the boundary. Thus this matrix is usually called *boundarymatrix*. The charge distribution is on the r.h.s of Eq. (6.14). Once the distribution is determined, the electrical potential can be obtained directly by solving Eq. (6.14), which can be easily solved with available numerical libraries such as Intel MKL which is used in this simulation.

A general description of the boundary matrix method can be found in details in [33].

6.3.5 Iterative method for sub-3D solution

Until now the potential on all the grid points in Fig. 6.4 obtained with the boundary matrix method for each slice is an incomplete solution as we have ignored the modification term in Fig. 6.5. It should be included in the Eq. (6.8) to give a complete solution to the Poisson's equation.

The problem is that at the very beginning we don't have any information of the potential distribution (which is exactly what we want to solve) needed to calculate this term. In such a case, an iterative method can be applied to deal with this

problem. It can be explained as:

1). Assume $\rho^{*,i}(x, y, z) = 0$, where $i = 0$;

2). Solve Eq. (6.8) including $\rho^{*,i}(x, y, z)$ with boundary matrix method;

3). $i = i + 1$, calculate new $\rho^{*,i}(x, y, z)$ from the solved potential distribution.

4). Repeat from Step 2)..

where i indicates the i-th iteration. For example, when $i = 0$, no iteration, solve only once. After i-th iteration, one could expect that the potential distribution will converge to the actual potential distribution determined by the Poisson's equation described with Eq. (6.6). Given that $(\Delta/\Delta z)^2$ is rather small, assuming $\rho^*(x, y, z) = 0$ at the beginning is reasonable. In fact, as will be shown later, the potential converges very quickly after several iterations.

A similar sub-3D space charge solver with slice scheme can be found in Ref [34] and the references there.

Another way of dealing with the longitudinal modification term is to solve the longitudinal electric field separately with charge line density model then included it as a correction term as described in details in Ref [35].

6.3.6 Justification

2D solution with boundary matrix method

In order to justify the method described in previous subsection, two ideal distributions which the space charge potential and electric field can be obtained analytically. In the first case, a round beam in a cylindrical vacuum chamber is assumed. In the transverse direction, the beam is uniformly distributed within the beam radius a. The radius of the vacuum chamber is b.

The potential in the transverse direction with a distance from the center of the beam can be obtained as,

$$E[r] = \begin{cases} \frac{\lambda}{2\pi\varepsilon_0} \frac{r}{a^2}, 0 \leq r \leq a \\ \frac{\lambda}{2\pi\varepsilon_0} \frac{1}{r}, a \leq r \leq b \end{cases} \tag{6.15}$$

Where λ is the charge line density, related to the beam current I_b as,

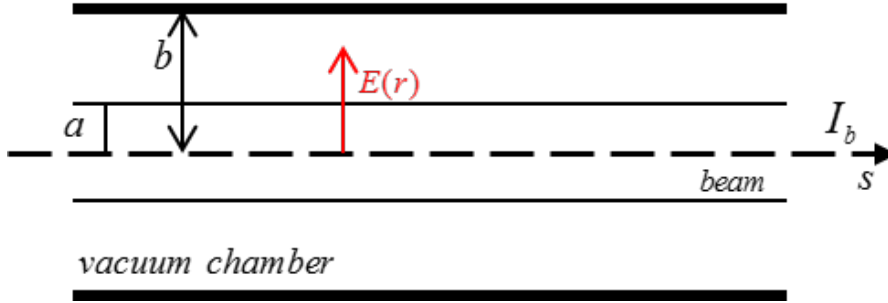$$\lambda = \frac{I_b}{\beta c} \tag{6.16}$$

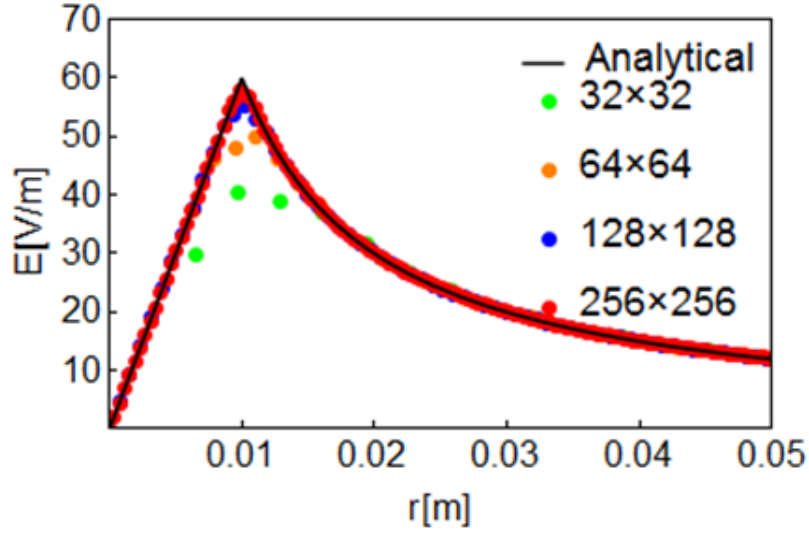Figure 6.6: Round beam in cylindrical vacuum chamber.

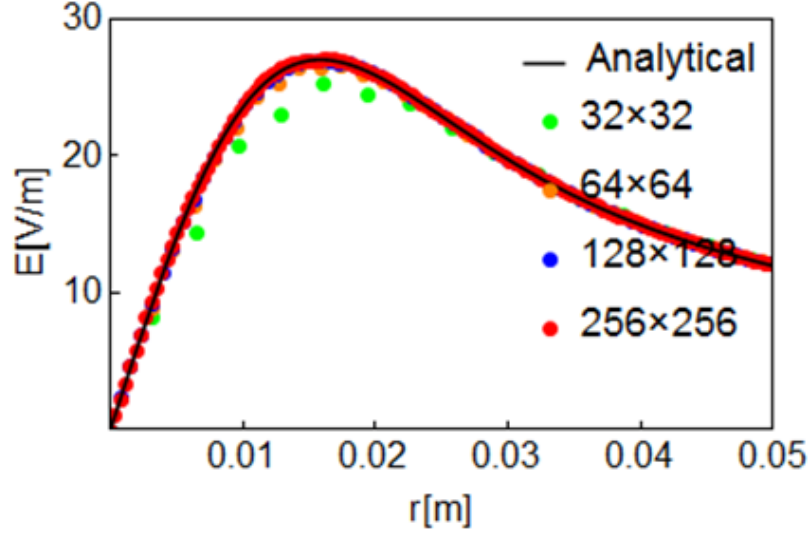Figure 6.7: Simulation results compared with analytical solution.

Figure 6.8: Simulation results for normal distribution.

Fig. 6.7 shows a comparison between the simulation results and the analytical solution given by Eq. (6.15) where $I_b = 100\,\mu\text{A}$, $a = 1\,\text{cm}$, $a = 10\,\text{cm}$, $\beta = 0.01$. In the simulation 10000 number of particles are generated uniformly within a and boundary with radius b is used to form the boundary matrix. In Fig. 6.7, solid line is the analytical solution while the other scattering points are the simulation results. Several mesh sizes have been compared as shown in this figure. Naturally as shown in this figure that in order to minimize the error for the field calculation, large mesh size is preferred. But in practical case, the beam is distributed smoothly in the transverse direction, unlike the model here where the beam has a sharp intensity drop at $r = a$. The second case tested here is a normal distribution which is much more similar to the practical case. Without fixed edge as in Fig. 6.6, the electric field for a normal distribution is,

$$E[r] = \frac{1 - e^{-\frac{r^2}{2\sigma^2}}}{2\pi r \varepsilon_0} \lambda \qquad (6.17)$$

where σ is the standard deviation for normal distribution. Similarly, the comparison between the simulation results and the analytical solution given by Eq. (6.17) is shown in Fig. 6.8, from which one can see that the result of 64×64 is better than the sharp edge case in Fig. 6.7.
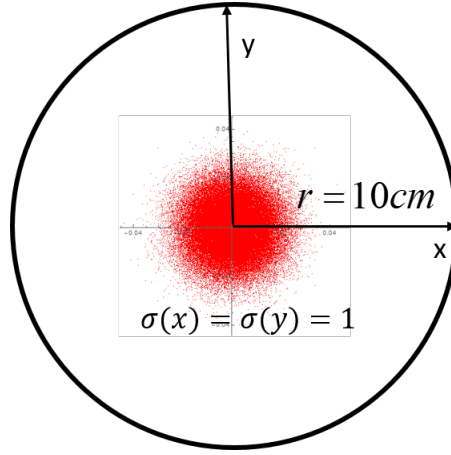
118

Figure 6.9: Test model for iterative method.

Sub-3D solution with iterative method

Just now we have shown that the boundary matrix solution provides us very good results of electrical field on each slice. In order to extend the result to the 3D case for a bunch, the iterative method should be included. In this subsection we will show the result with this method and decide how many iterations should be applied to get a proper sub-3D results.

Assuming a cylindrical chamber with a radius of 10cm as shown in Fig. 6.9. The beam is normal distribution in all directions with $\sigma_x = \sigma_y = 1$ cm. The test number of macro particle is 10^5 and the total charge is assumed 400×10^{-12}. The grid point numbers for PIC are $N_x = N_y = 128$ and $N_z = 50$.

The results of the potential along the longitudinal axis ($x = y = 0$) with various iterations are shown in Fig. 6.10, in which '0x' indicates no iteration applied, '1x' indicates after first iteration and so on. Fig. 6.10 shows that there is no significant difference among these results. However, if we scale up to see the details, for example at $z = 0$ m, with Fig. 6.11, we will notice that there is a difference after the first iteration, though no noticeable difference appear beyond that.

The difference between each iteration is shown in Fig. 6.12, where "1x" indicates the point-to-point difference in percentage between "0x" and "1x" in Fig. 6.10. We can see that with one iteration, for the most part of the beam, the difference is less than 1 percent. After the 2nd iteration, the results of the potential at most part of the beam almost stay the same. Another graph with 10^6 macro particles is shown in Fig. 6.12, which shows better results after each iteration.
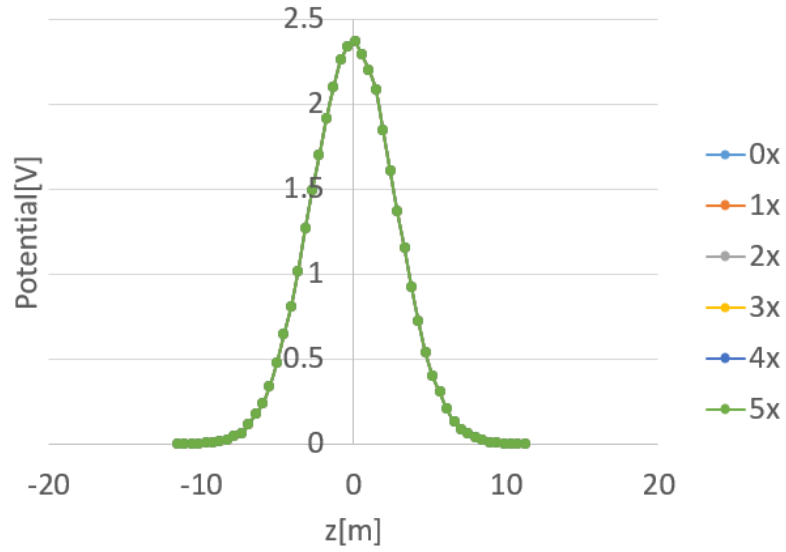
Figure 6.10: Potential along the longitudinal direction with the iterative method.
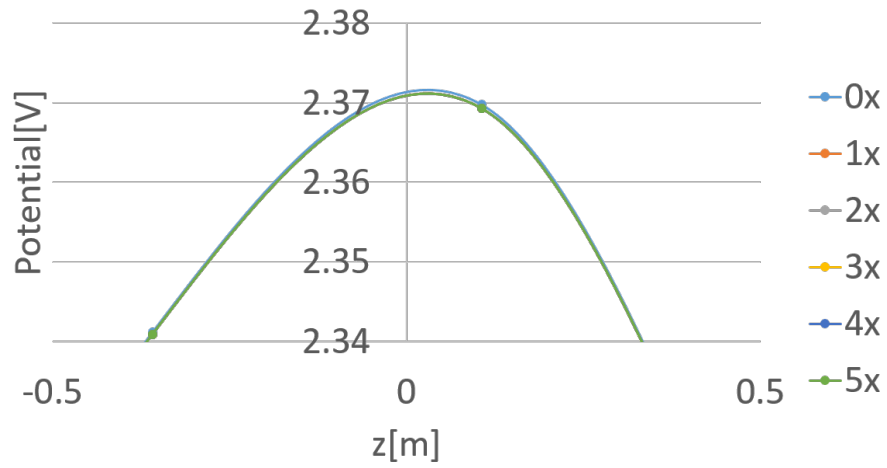

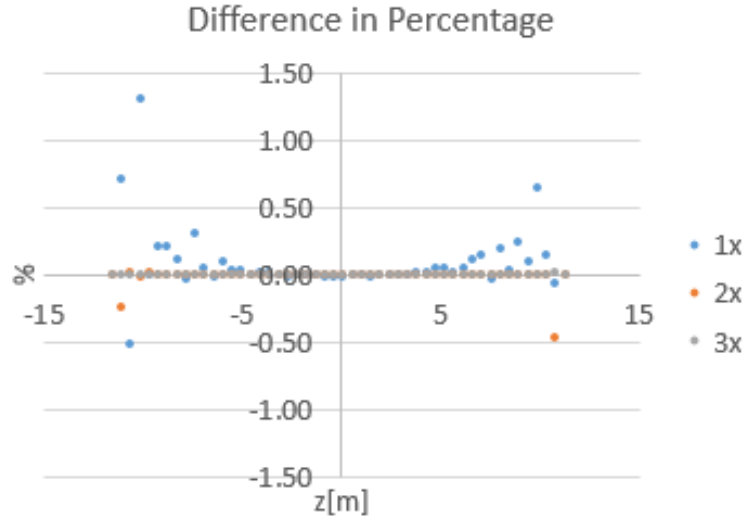Figure 6.11: Scaled view of Fig. 6.10 about $z = 0$ m.

Figure 6.12: Difference after each iteration, 10^5 macro particles.
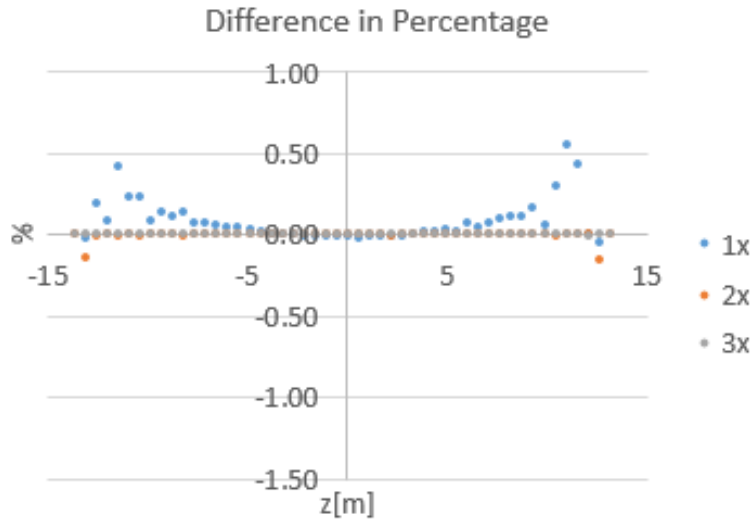

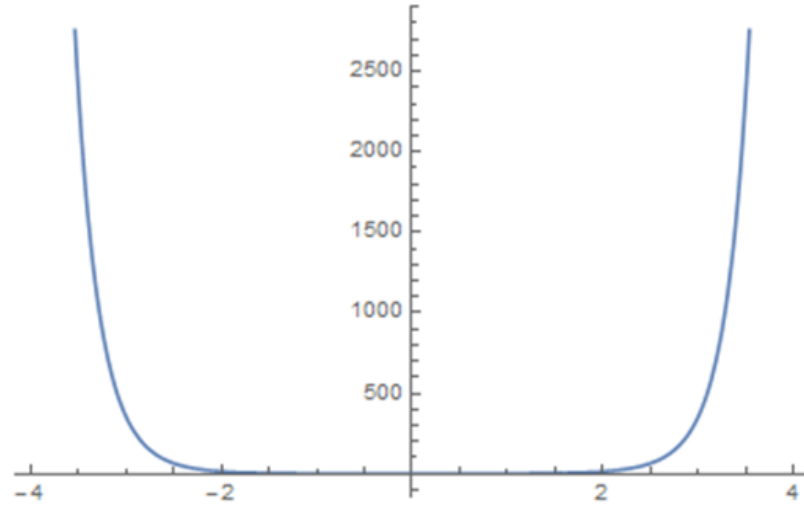Figure 6.13: Difference after each iteration, 10^6 macro particles.

Figure 6.14: Secondary derivative of a normal function ($\sigma = 1$).

Notice that the modification term in Eq. (6.8) and Eq. (6.9) is determined by the 2nd derivatives of the potential in the longitudinal direction (or the gradient of the longitudinal electric field). Here we assumed a normal distribution in the longitudinal direction. Thus in general, its second derivative has a profile as shown in Fig. 6.14.

When calculate the potential on each slice without applying the iterative method, we actually ignored this second derivative terms. With iteration method, the difference shown in Fig. 6.12 and Fig. 6.13 shares the similar profile as in Fig. 6.14. For normal distribution, its second derivative increases rapidly as the distance from its center increases. But the particle number at those places are also quite small so it has over all little affect to the beam.

Overall speaking, the iterative method will help in increasing the precision of the solver's results. The results discussed here indicate that it is not necessary to go beyond the 2nd iteration with this method.

6.4 Summary

A simulation code developed for the induction synchrotron was introduced with detailed description on the space charge solver. The particle distribution is tracked along the beam line by transfer matrix for a specified step size. The code added a simple space charge kick to the existing transfer matrix method. The simulation code has the following features:

1). Lattice calculation, including the periodic determined Courant-Snyder parameters of a ring, the bare betatron tune, the nature chromaticity, momentum compaction factor, etc.;

2). Element-wisely tracking with externally defined beam line;

3). Space charge inclusion with arbitrary boundary for each element;

4). Beam loss location and time record;

5). Simulation Mode similar to the actual beam commissioning;

6). Induction cell with external table which can contains the pulse density control scheme.

As a space charge solver, a numerical way of solving the Poisson's Equation was developed. A slice scheme and the iterative method to give the sub-3D potential was adopted for this solver. Boundary matrix method was used to solve the reduced Poisson's Equation in 2D case with arbitrary boundary shapes. This space charge solver was justified by comparing its results with the analytical calculation in the 2D case and the iterative method showed that the sub-3D potential converges very fast after only one or two iterations.

This simulation was developed in a general way to study the induction synchrotron. In next chapter, the simulation code will be applied to study the beam dynamics in the KEK-DA ring.

Chapter 7

Particle Tracking Simulation and the Beam Loss in the KEK-DA Ring

The beam commissioning for the KEK-DA has been stated since 2010. Early commissioning results have been presented in the publications [7, 8, 36].

There are three kinds of beam commissioning in the KEK-DA:

(a). Free run: with constant magnetic field, or injection field, and no barrier bucket or acceleration pulses;

(b). B_0 with V_{bb}: confinement commissioning with barrier bucket pulses, V_{bb} under constant magnetic field (B_0);

(c). B(t) with $V_{bb} + V_{acc}$: barrier bucket confinement (V_{bb}) and induction acceleration V_{acc} with ramping magnetic field starts at a B_{min} and end at B_{max} described as

$$B(t) = \frac{1}{2}(B_{\min} + B_{\max}) - \frac{1}{2}(B_{\max} - B_{\min})\cos\omega t$$

where ω is the angular frequency of the KEK-DA operation cycle.

In the simulation code, Simulation Mode 1 in Table 6.1 is used for static magnetic field, so it includes the case (a) and (b) in beam commissioning, the only difference is whether to turn on the V_{bb} or not. Simulation Mode 2 in Table 6.1 is used for ramping magnetic field, namely case (c) here. In this chapter, case (a) in Simulation Mode 1 will be discussed in details to study the beam dynamics and the beam loss in the KEK-DA ring.

7.1 The KEK-DA ring in the simulation

7.1.1 Element list

At the beginning, the element list will be imported by the simulation code to generate the beam line as described in previous chapter. In the case of the KEK-DA, part of the element list is shown in Table 7.1. For the complete element list of the KEK-DA ring, please see the Appendix.

As shown in Table 7.1, one "Monitor" is put at the middle of the $S5$ section, similar to the position of the actual Bunch Monitor (Fig. 3.1). An induction cell "IC_Vbb" is put at the middle of $S6$ section and another "IC_Vac" is put at the middle of $S7$. The induction cells are assumed to kick the beam at a single position for simplicity. "Type ID" is used to identify the element; "Shape ID" is used to specified the ID of the cross section of the boundary specified by the boundary list (Table B.2 or Table B.3); "Length" is the actual element length. Appendix A provides the definition of each element in details.

7.1.2 Calculation of lattice functions

The lattice functions can be calculated with Simulation Mode 1 (Table 6.1). With the element list of the KEK-DA ring, the results of the beta function and the dispersion function along the KEK-DA ring are shown in Fig. 7.1.
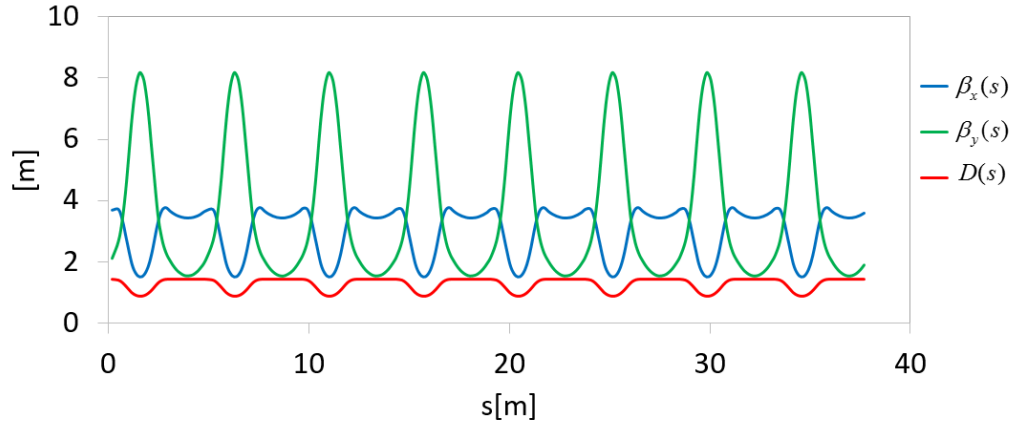

Figure 7.1: The beta function and dispersion function calculated for the KEK-DA ring.

Table 7.1: The list of the KEK-DA ring lattice parameters assumed in the simulation(part).

Type ID	Name	Shape ID	Length[m]	k0	k1
2	M4_F1	3	0.63	0.092	1.096
2	M4_H1	3	0.04	0.092	0
2	M4_D1	3	1.26	0.092	-1.103
2	M4_H2	3	0.04	0.092	0
2	M4_F2	3	0.63	0.092	1.096
1	S5_1	3	1.06	0	0
7	B_Monitor	3	0.00	0	0
1	S5_2	3	1.06	0	0
2	M5_F1	3	0.63	0.092	1.096
2	M5_H1	3	0.04	0.092	0
2	M5_D1	3	1.26	0.092	-1.103
2	M5_H2	3	0.04	0.092	0
2	M5_F2	3	0.63	0.092	1.096
1	S6_1	1	1.06	0	0
8	IC_Vbb	1	0.00	0	0
1	S6_2	1	1.06	0	0
2	M6_F1	3	0.63	0.092	1.096
2	M6_H1	3	0.04	0.092	0
2	M6_D1	3	1.26	0.092	-1.103
2	M6_H2	3	0.04	0.092	0
2	M6_F2	3	0.63	0.092	1.096
1	S7_1	1	1.06	0	0
8	IC_Vac	1	0.00	0	0
1	S7_2	1	1.06	0	0

7.2 Initial distribution

In the simulation, the initial beam distribution should be as close to the actual beam distribution as possible. For the 6D phase space, they should be reasonably comparable to the real beam. In the simulation, the exit of the injection kicker (see Fig. 3.1) is chosen as the starting point of the simulation.

Here we assume the Courant-Snyder parameters determined by the ring lattice as shown in Fig. 7.1. The parameters shown in Table 7.2 are used. The beam emittance ε_x and ε_y are assumed to be 100 $mm.mrad$ and 70 $mm.mrad$ based on the experiment measurement on the LEBT line. The code to generate such a multivariate distribution is described in Appendix B. The generated transverse phase space with

Table 7.2: Initial distribution parameters.

β_x[m]	α_x	ε_x[mm.mrad]	β_y	α_y	ε_y[mm.mrad]
3.60	-0.21	100/4	1.91	-0.48	70/4

macro particle distribution is shown in Fig. 7.2 (horizontal with 2σ region marked out as green ellipse) and Fig. 7.3 (vertical).
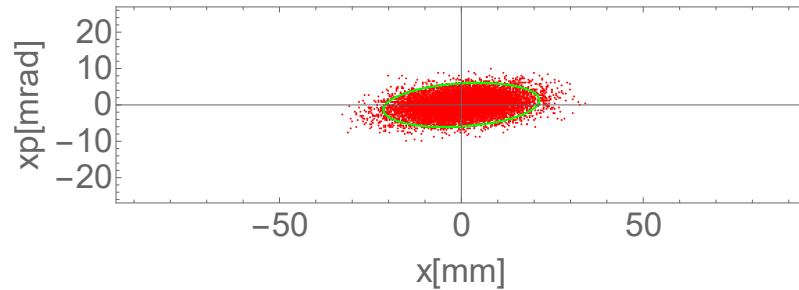

Figure 7.2: Initial distribution determined from the Courant-Snyder parameters in the ring and assumed emittance: Horizontal.

For the longitudinal direction, Einzel Lens Chopper discussed in Sec. 4.4 generates a chopped beam with very sharp edge in the longitudinal beam intensity profile (see Fig. 4.14). As a result, assumption of the uniform intensity distribution is reasonable. For the momentum spread, the confinement experiment showed that the beam in the KEK-DA has a momentum spread about 0.25% [37]. So the momentum spread is assumed to be normal distribution with $\sigma(\Delta p/p) = 0.12\%$, as shown in Fig. 7.4.
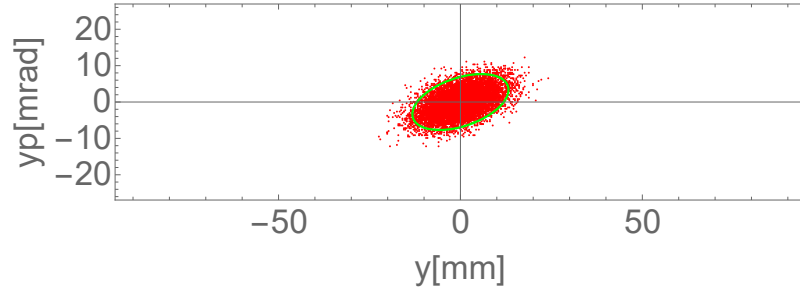
Figure 7.3: Initial distribution determined from the Courant-Snyder parameters in the ring and assumed emittance: Vertical.
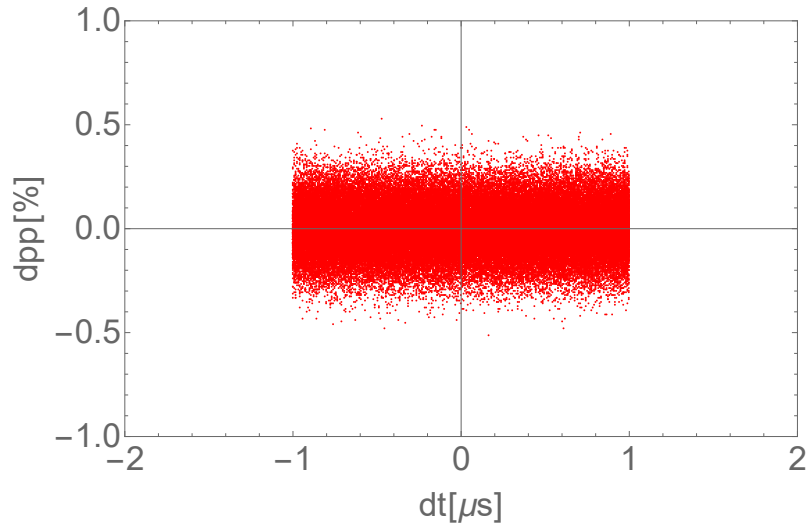

Figure 7.4: Uniform longitudinal intensity distribution and normal distributed momentum spread.

For the specific purpose to discuss the longitudinal space charge effects, a normal distributed intensity profile in the longitudinal direction is assumed as shown in Fig. 7.5.
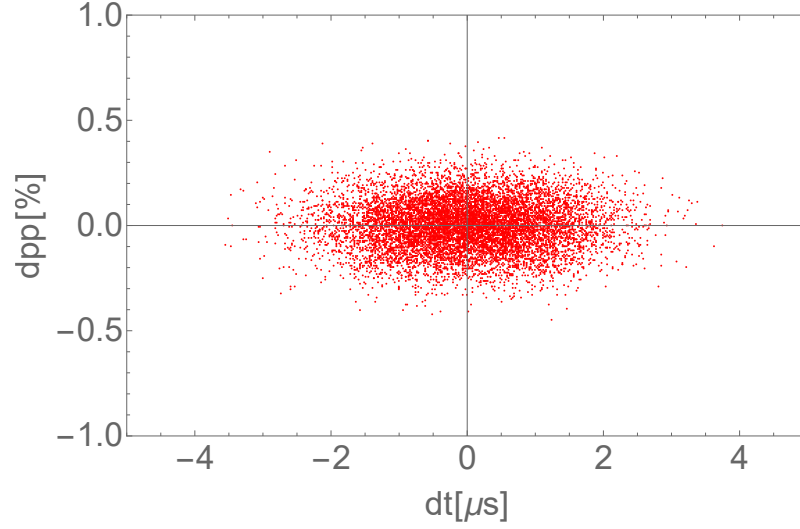

Figure 7.5: Normal longitudinal intensity distribution and normal distributed momentum spread.

7.3 Emittance blow-up due to space charge forces

To avoid the emittance reduction due to beam loss, we have assumed a large boundary as shown in Table B.3. Figs. 7.2, 7.3 and 7.5 have been used as initial distribution in this simulation.

In the simulation, the emittance are defined by Eq. (7.1) for each direction.

$$\overline{x} = \sum_{i=1}^{N} x_i$$
$$\overline{x'} = \sum_{i=1}^{N} x_i'$$
$$\overline{x^2} = \sum_{i=1}^{N} (x_i - \overline{x})^2$$
$$\overline{x'^2} = \sum_{i=1}^{N} (x_i' - \overline{x'})^2 \qquad (7.1)$$
$$\overline{xx'} = \sum_{i=1}^{N} (x_i - \overline{x})(x_i' - \overline{x'})$$
$$\varepsilon = \sqrt{\overline{x^2} \cdot \overline{x'^2} - (\overline{xx'})^2}$$

where N is the number of the macro particles. Note that here the actual particle position in the 6D phase space is used. In the horizontal direction, it includes not only the betatron oscillation of the particle but also the information of equilibrium orbit given by Eq. (2.119).

The simulation parameters are listed in Table 7.3, where a 3D (64,64,50) grid has been used and the total charge of the beam has been changed from 100×10^{-12} C to 2000×10^{-12} C to see the emittance blow-up for the different beam intensity with the same distribution. The results are shown in Figs. 7.6 to 7.8.

Table 7.3: Simulation parameters.

Nx(=Ny)	Nz	N	Total Charge[C]
64	50	10^5	$\times 10^{-12}$

It turns out from Figs. 7.6 to 7.8 that the emittance increases in all directions as the total charge (or the beam current intensity) increases.

For the horizontal direction, the emittance (Ex in Fig. 7.6) continues to increase after 20 turns. However, for the vertical direction, the emittance increases very quickly at the first several turns but the blow-up process also rapidly slows down, especially for the high intensity case. The rapid emittance blow-up at the very beginning may be explained by the strong nonlinear effects originated from the normal distribution.
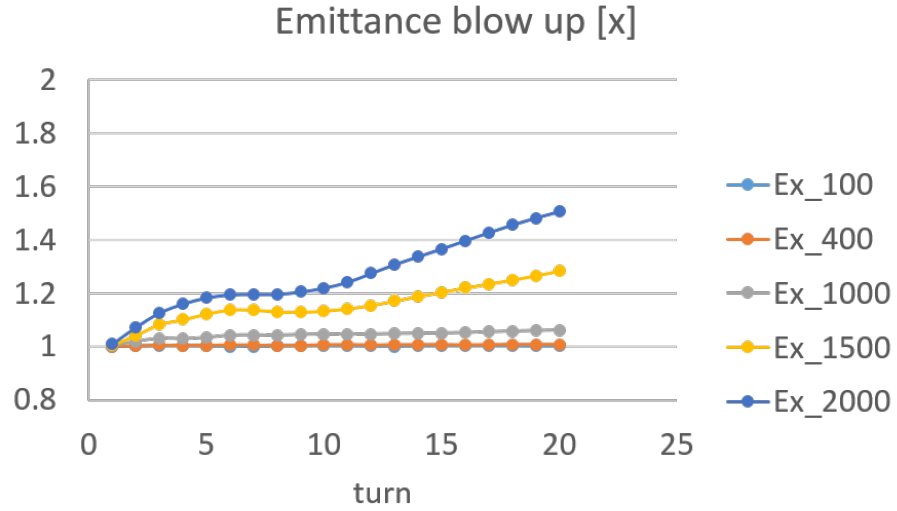
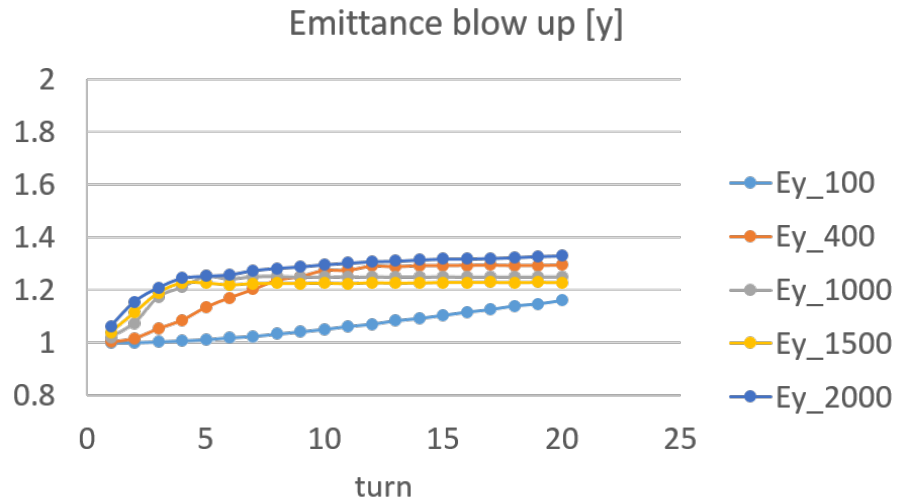Figure 7.6: Transverse emittance blow-up: Horizontal.

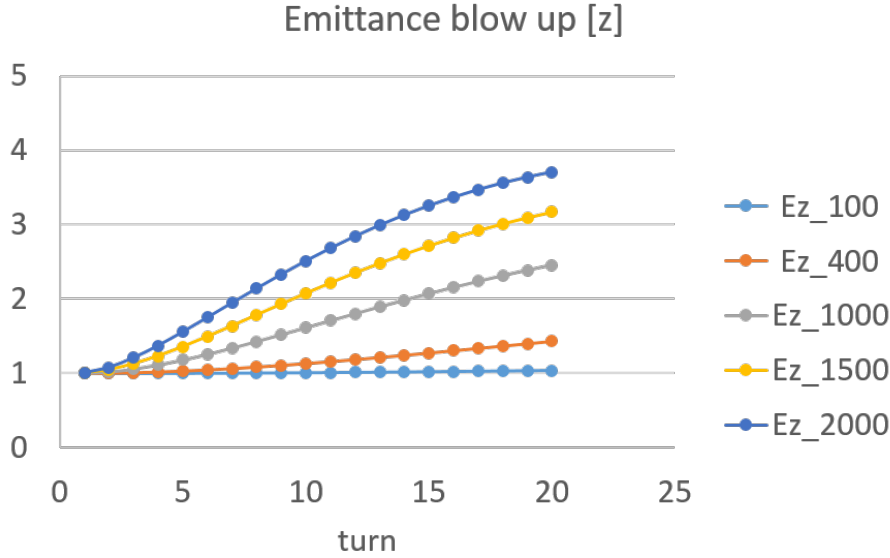Figure 7.7: Transverse emittance blow-up: Vertical.

Emittance blow up [z]

Figure 7.8: Transverse emittance blow-up: Longitudinal.

When the particle distribution redistributes due to the space charge force to achieve a kind of equilibrium state. It is speculated that the nonlinear forces originated the space-charge trigger a strong filamentation in the phase space distribution, resulting in the emittance blow-up and simultaneously reducing the space-charge effects. In addition, the transverse space charge forces gradually decrease because the beam expands due to the momentum spread in the longitudinal direction, reducing the local line density.

At Turn 20, the beam distributions for these cases in the phase space for these cases are shown in Figs. 7.9 to 7.13, where x and y are in mm, xp and yp in mrad, dt in μs and dpp in percentage. The emittance blow-up due to the space charge effects is clearly seen. Especially in the longitudinal direction, the phase space distortion due to nonlinear space charge force is clearly visible. It looks like $s-$shapes for the high intensity cases.

133

BEAM DISTRIBUTION 20

x-xp

y-yp

x-y

dt-dpp
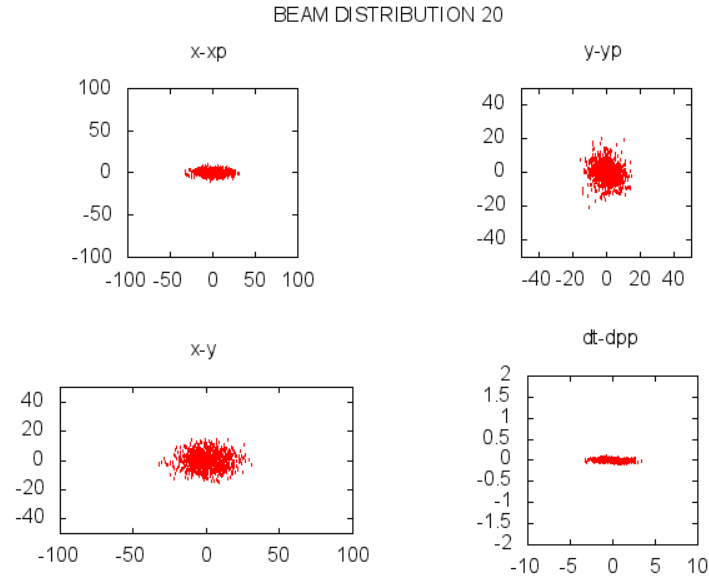
Figure 7.9: Turn 20: 100×10^{-12} C.

BEAM DISTRIBUTION 20

x-xp

y-yp

x-y

dt-dpp
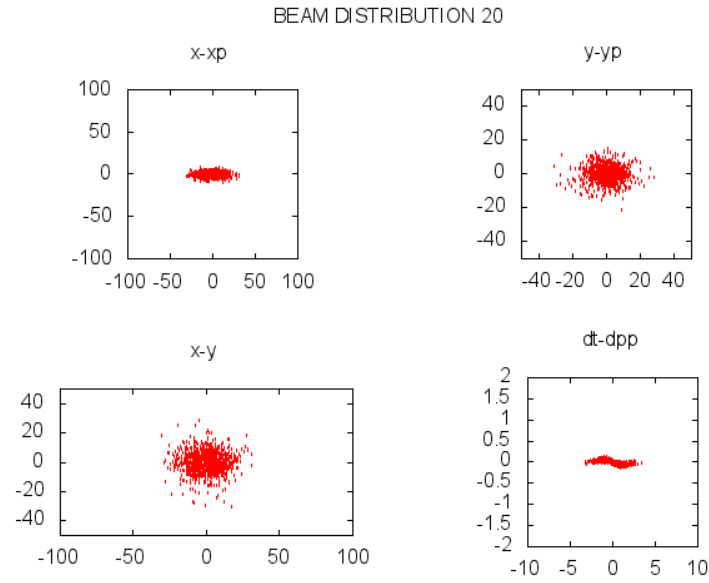
Figure 7.10: Turn 20: 400×10^{-12} C.

BEAM DISTRIBUTION 20
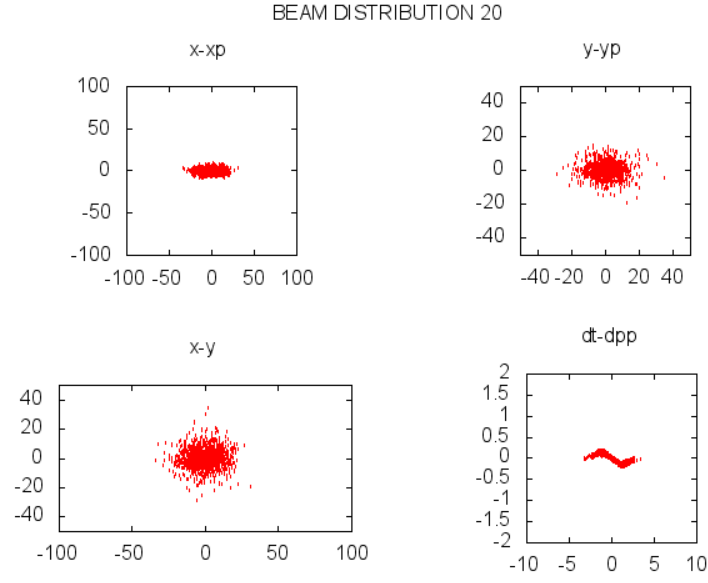
Figure 7.11: Turn 20: 1000×10^{-12} C.

BEAM DISTRIBUTION 20
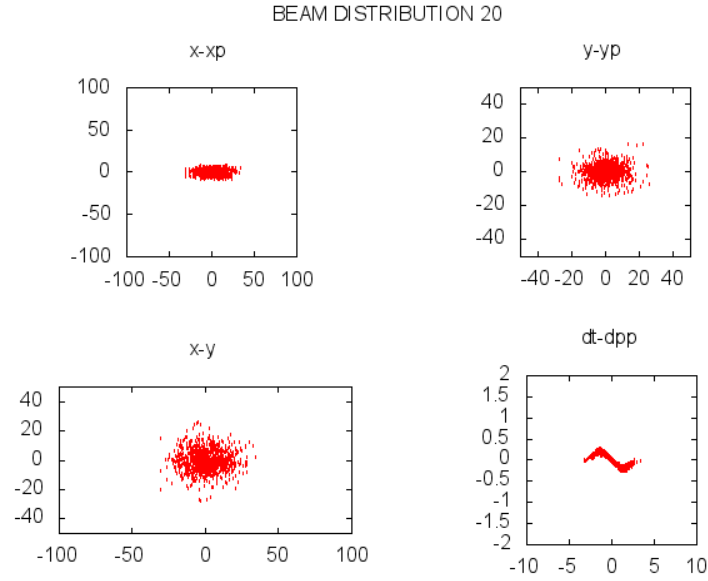
Figure 7.12: Turn 20: 1500×10^{-12} C.

BEAM DISTRIBUTION 20
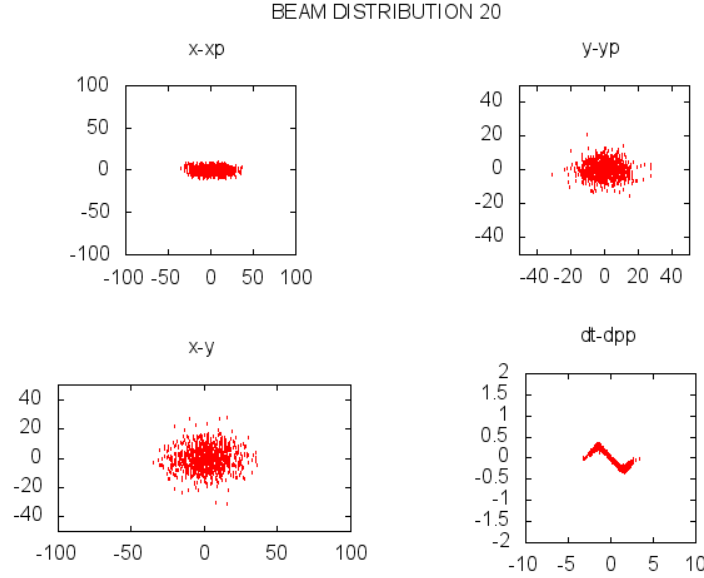
Figure 7.13: Turn 20: 2000×10^{-12} C.

7.4 Beam loss in the free circulation under the injection magnetic field

7.4.1 Typical beam loss pattern

The Bunch Monitor signal (CH2 in Fig. 7.14) shows an example of the free run mode when the beam injected into the KEK-DA ring was simply stored. The magnetic field was set to be the injection magnetic field and there was no barrier bucket confinement or acceleration.

The signals from the Bunch Monitor for each turn were integrated to reflect the total particle number in the beam. As a result, the survival rate of Fig. 7.14 can be plotted as shown in Fig. 7.15. It can be divided into three stages:

Stage I. Fast loss at the very beginning for a short time;

Stage II. Gradual slow loss;

Stage III. Decreasing to zero.

In Stage III, the signal drop does not reflect the beam loss. The beam spreads in the longitudinal direction due to the momentum spread and the beam tail will meet
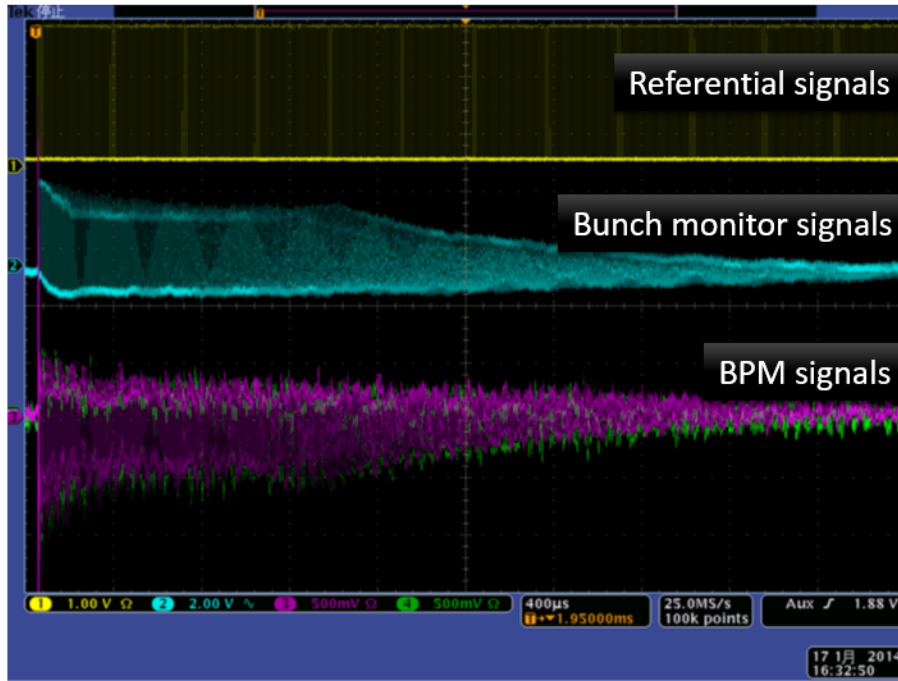
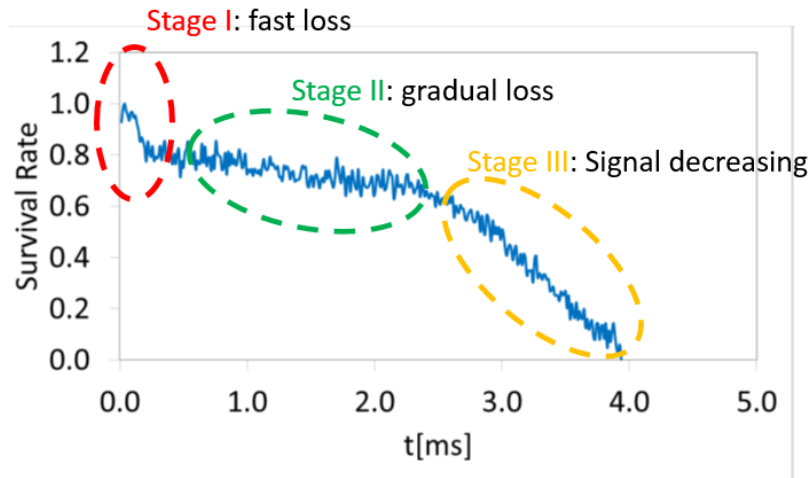Figure 7.14: Free run under the static magnetic field.

Figure 7.15: Survival rate for beam in Fig. 7.14.

with the beam head in the ring. The bunch monitor which is used to capture the beam signal in the ring will not be able to capture the DC component when the beam occupies the whole ring. Thus, the signal from Bunch Monitor drops. The discussion on the beam loss is limited in Stage I and II.

7.4.2 Beam loss in beam commissioning

In Sec. 5.1, we have discussed the beam parameters measurement with the profile monitor by changing the excitation current of the Q magnets at the downstream LEBT line.

Fig. 7.16 shows survival rate for ten cases of different downstream LEBT settings while in the upstream of LEBT Line the beam current intensity was the same. (Fig. 7.15 is $s0$ in Fig. 7.16). These results suggest that the phase space distribution strongly depends on the LEBT settings and it is very easy to create mismatched beam injection into the ring.
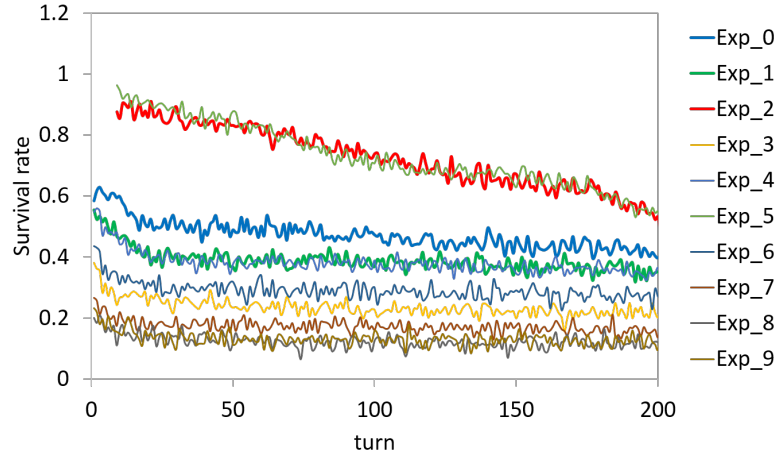
Figure 7.16: Beam survival comparison under different lattice settings in the LEBT line.

The observation for Stage I and II are summarized as follows:

Stage I. In cases of Exp_2 and Exp_5. They have higher intensity right after the injection. It may be due to a better optics match between the LEBT and the ring. Other cases suffers from immediate loss at the injection (note that in LEBT line the beam intensity is the same for all cases) or fast loss after injection. It may be due to bad optics mismatch or even

the injection error of the beam centroid because we did not confirm the injection error correction with steering magnets in the LEBT line for these cases.

Stage II. The beam has higher intensity decreases faster while with lower intensity it suffers little further loss. It is intensity dependent which may be related to the space charge effects. Unfortunately, it also suggests that for the present KEK-DA ring, assuming we can increase the beam intensity from the ECRIS and have it properly injected into the ring, the higher intensity beam will get lost faster to demerit the improvement in the ECRIS and LEBT line.

7.4.3 Discussion with simulated results

Sources for beam loss

In order to confirm the effectiveness of the developed simulation code, the experimental results of the beam loss are compared with simulation results. Unfortunately the KEK-DA ring is not equipped with any transverse beam profile monitor. Temporal evolution of the transverse beam profile is not available. Beam intensity is always monitored by the bunch monitor placed in the S5 Section (Fig. 3.1). Only the integrated bunch monitor signal can be used to measure the beam survival rate.

The following reasons for beam emittance blow-up are anticipated in general.

(A) Injection mismatch: the mismatch of the beam centroid;

(B) Injection mismatch: the mismatch in the betatron phase space;

(C) Space charge induced emittance blow-up;

(D) Nonlinear field effects intrinsic in the actual magnetic field;

(E) Ripple in the power supply of the guiding magnet;

(F) Small angle Coulomb scattering;

(G) Other collective instabilities.

There are also other fatal mechanisms resulting in instantaneous beam loss. For example, the charge exchange process (electron capture/stripping) between the heavy ion particles and the residual gas molecules. Fortunately, the life time caused by electron capture/stripping is known and the life time is much larger than the time

scale of our concern [6]. Moreover, the loss due to the charge exchange with the residual gas molecules should be independent of the intensity.

Meanwhile, the beam blow-up caused by (A) and (B) should be fast. In most of operations the mismatch of the beam centroid at the injection is observed as a coherent betaron oscillation and can be corrected with the combination of steering magnets in the LEBT downstream. Some betatron mismatching always exists. (C) depends on the injected beam intensity. (D) strongly depends on the betatron tune and it is hard to know (E). Rough estimation of (F) leading to slow beam blow-up is possible. When (G) is induced, the discrete beam loss with any specific frequency should be observed. Thus (F) and (G) can be excluded from the discussion here. It is noted that the present simulation code can include only (A),(B) and (C).

Simulation results

Particle loss from the accelerator ring takes place when a particle with a large oscillation amplitude hits the surrounding boundary. In this sense, the assumption of the realistic boundary in the simulation code is crucial.

We have simulated motions of the macro partciles in the free run mode for various cases and compared the results of beam loss with the beam commissioning results in Fig. 7.17. The default initial distribution was generated as shown in Figs. 7.2 to 7.4. The actual boundary list in Table B.2 has been used in these cases which are used to calculate the beam induced potential and judge the particle loss.
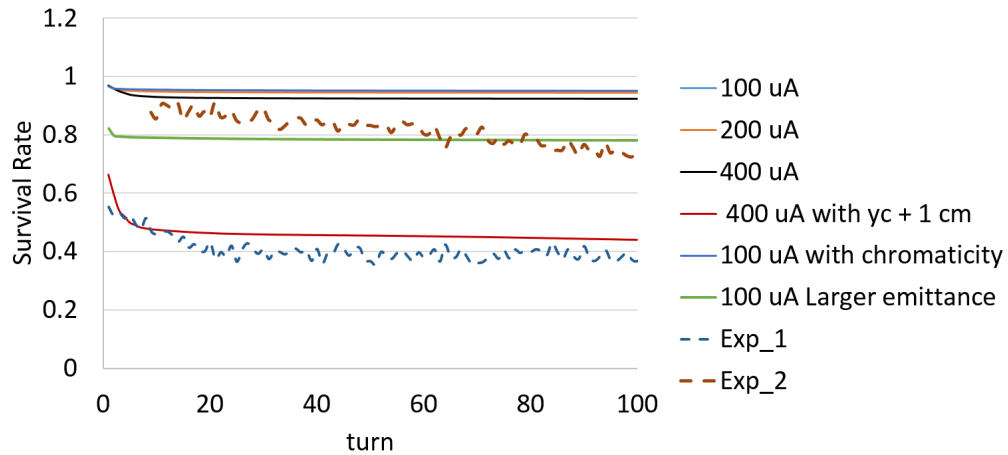

Figure 7.17: Comparison between the simulation and the experimental results.

In Fig. 7.17,Exp_1 and Exp_2 (dashed lines) are the same cases as in Fig. 7.16.

They are chosen to stand for the experimental results for low intensity (Exp_1) and high intensity (Exp_2).

All the simulated cases here are conducted with 10^5 number of macro particles and a $(64, 64, 50)$ 3D grid. In the phase space, except for "Larger Emittance" and "400uA with yc + 1cm", all the other cases follow the distribution in Fig. 7.2 and Fig. 7.3 for the transverse direction and Fig. 7.4. Uniform distribution of the longitudinal intensity which is more like the real case has been chosen here. In the case of "*Larger emittance*", $\sigma(\varepsilon_x) = 100/2$ [mm.mrad] $\sigma(\varepsilon_y) = 70/2$ [mm.mrad] have been used. In the case of "400uA with yc + 1cm", as the title suggests, $400\,\mu A$ is assumed and the beam centroid has been moved 1 cm in the phase space in the vertical direction to simulate the mismatch in the phase space.

Here is the description of each case:

a). "100 uA", 100 μA beam intensity is assumed.

b). "200 uA", 200 μA beam intensity is assumed.

c). "400 uA", 400 μA beam intensity is assumed.

d). "100 uA with chromaticity", 100 μA beam intensity is assumed and transported with chromaticity.

e). "Larger emittance", a larger emittance than other cases assumed.

f). "400 uA with yc+1 cm", 400 μA beam intensity is assumed and beam centroid moved up 1 cm in the vertical phase space.

Case a, b and c are used to compare the space charge effects on the beam loss. They are plotted separately again in Fig. 7.18.
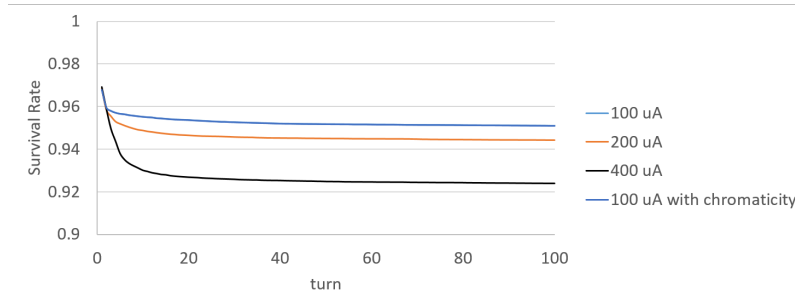

Figure 7.18: Survival rate comparison among different beam intensities.

We can see that from Fig. 7.18 and Fig. 7.17, the space charge does increased the beam loss rate at the beginning (Stage I) but the absolute loss rate is within 8% given the beam intensity of 400 µA (which is not achieved in the KEK-DA ECRIS). So it is unlikely the reason for the fast loss happened as in Exp_2. Case *d* suggests that the chromaticity effect which should be reasonably small is neither the reason.

Larger emittance will result in immediate loss at injection, accounting for about 20% beam loss in the simulation. Case *f* phase space mismatch at injection which is similar the the Exp_2 case in the beam commissioning is the most important reason for the fast beam loss after injection. In Case *f*, the beam gets lost very quickly due to the extra injection error we set in the simulation. In the beam commissioning, we would correct the injection error with steering magnets at the LEBT line which can be typically make the centroid deviation less than 5 mm after correction.

However, the experimental results show that for higher intensity, after Stage I (when the beam spread to occupy the whole phase space due to betatron oscillation and the space charge perturbation), the higher intensity case (Exp_1) tends to get lost much more faster than the lower intensity case (Exp_2). Simulated results with higher intensity don't show such obvious difference in beam loss trend from the lower intensity.

In general, we have confirmed that the fast loss after the injection are mainly due to the phase space mismatch at the injection, space charge effects did affect the beam loss but turned out not to be the dominant source at this stage. After 20 turns or so, the beam with high intensity in the simulation does not yield the beam loss to the same extent as suggested by the experiment. This suggests that other sources such as (D) and (E) need to be investigated.

7.5 Summary

In this chapter, the simulation code has been applied to the KEK-DA for beam study.

The lattice of the KEK-DA ring has been calculated with the simulation code.

The beam emittance blow-up was investigated with the simulation at various beam intensities. It was proved that the vertical emittance increases very quickly but came to an close-to-equilibrium state very fast for higher intensity beam compared with the lower intensity beam for which the emittance blow-up process was very slow. The horizontal emittance continued to increase when the longitudinal emittance continued to raise due to space charge forces.

For the beam loss study with the simulation, several cases were simulated to identify the sources for beam loss. The space charge contributed to the beam loss

at the beginning but its contribution to the beam loss was less than that from the phase space mismatch.

The reasons for the larger beam loss at higher intensity at Stage II are still unidentified. Other factors in the ring and beam in the ECRIS and LEBT line would be worth to investigate and the simulation code should be extended to include them.

Chapter 8

Conclusions

8.1 Summary

The primary objective of the KEK-DA is to demonstrate a compact fast cycling induction synchrotron. This thesis described the experimental studies on beam commissioning from the ion source to the ring and focused on the simulation code that was originally developed to understand beam loss in the KEK-DA ring as well as essential properties of beam dynamics there.

In Chapter 1, the brief history of the induction synchrotron was introduced. The KEK-DA of a fast cycling induction synchrotron, was realized by renovating the former KEK-PS Booster Ring. All the thesis work were done at this facility.

In Chapter 2, the beam dynamics of the induction synchrotron was reviewed. The equations of single particle motion were self-consistently derived from the Hamiltonian. The transfer matrices for lattice elements such as drift section, combined function type magnet and quadrupole magnet were derived in the 6D phase space. The transfer matrices have been implemented as essential components in the simulation code that is described in Chapter 6.

In Chapter 3, the subsystems with their latest status of the KEK-DA, without which the present beam studies could not have been realized, were presented. It should be emphasized that the experimental results would have never been obtained without various improvements performed by the present author which have not been documented in any officially written form. For instance, forced cooling of the guiding magnet under the serious surrounding condition in the mid-summer to make the field stabilized is one of them.

In Chapter 4, the KEK-DA ECRIS was described. In order to suppress the discharge problem in the extraction region of the original KEK-DA ECRIS, redesign

of the extraction electrode and orifice have been initiated by the present author. In addition, the replacement of the plasma chamber, gas support system, and vacuum pump have been conducted. With the present status of instruments, the optimization work for the operational parameters employing the IGUN simulation were described and the experimental results were analyzed.

In Chapter 5, two experimental studies using the profile monitors on the LEBT line were discussed. In the first experimental study, the Courant-Snyder parameters and the transverse beam emittance were measured. The results in the vertical direction were fairly good, while the horizontal ones were with some ambiguity because of the momentum dispersion effects. In the second experimental study, a quasi-3D profile monitor had been developed by modifying the original wire-grid based profile monitors. With the quasi-3D profiles observed at the PR2, the 4 ms long beam was found to have a bending part while the 4 ms beam was found to have a shifted beam head and tail. It turned out from careful experiments and circuit analysis that the beam loading effects take place in the extraction region of the ECRIS and the post-acceleration column of the HVT, resulting in the momentum modulation in the 4 ms long beam. The momentum modulation had been known to be induced as a result of chopping of the beam pulse in a short time period of 4 ms beam by the Einzel Lens Chopper [22]. This fact was confirmed in the present experiment in the LEBT line for the first time.

In Chapter 6, the simulation code developed for the induction synchrotron was discussed. The structure of the simulation code was described with two flow charts. The core calculation includes the momentum kicks due to space charge effects and the orbital evolution of the particle distribution is obtained from macro-particle tracking using the transfer matrices, which were derived in Chapter 2. The sub-3D space charge solver was discussed in details with the justification of its validity.

In Chapter 7, the simulation code was applied to the KEK-DA. At first, the lattice functions were calculated assuming the lattice elements of the KEK-DA ring. The beam emittance blow-up in terms of total charge in a beam bunch in the KEK-DA ring was discussed where coupled motion made the horizontal emittance continue to increase while the vertical emittance blow-up slows down very quickly. In the simulation aiming to identify the beam loss in the KEK-DA ring, space charge effects were found less dominant than the injection error at the early stage after injection. There are still unknown factors causing the beam loss which can not be explained by present simulation code.

146

8.2 Perspectives

We have discussed the novel KEK-DA, focusing on the beam dynamics from production in the ion source through the ring itself, as well as key instruments. We can state the following perspective views, based on the newly recognized characteristics of the fast cycling induction synchrotron system in this thesis work and the originally developed 3D simulation code that allows us to track the motions of macro-particles over its entire acceleration cycle.

For the present KEK-DA, the following works will be very helpful in the beam physics studies:

1. Compensate the beam loading effects at the post-acceleration column of the HVT. A proposed circuit was given in Fig. 5.30;

2. Install emittance monitor at different locations of the LEBT line. This will be of great help in obtaining the emittance of the beam from the source and the emittance blow-up along the LEBT line;

3. Measure the beam profile with flying wire scanner or other monitor in the ring. The turn-by-turn beam profile in the ring will provide a direct way to evaluate the beam size evolution which is very helpful in studying the emittance blow-up due to space charge and other collective effects.

For the future induction synchrotron accelerators, the above list still stands. In addition, we strongly suggest that both the LEBT line downstream and the injection section should be designed as dispersion free region. This will make injection mismatch much easier to be corrected.

In the numerical side, the application of the simulation code has not been exhausted and some future work can be undertaken. In the beam commissioning with barrier bucket pulses and acceleration with pulse density control, the longitudinal emittance is expected to increase. As a result, the beam emittance blow-up in the horizontal direction can be expected in such a dispersive system. We had plenty of beam commissioning results under barrier buckets and acceleration pulse [7,8]. Therefore, to understand how the longitudinal emittance blow-up under these conditions through simulation is very interesting from the point view of beam dynamics and it is also helpful to optimize the confinement voltage pulses and the acceleration scheme with simulation.

Moreover, as suggested in Sec. 7.4, more beam physics should be included in the present simulation code to make it a much more realistic tool in identifying the beam

loss mechanism in the induction synchrotron.

In the end, we would like to emphasize the original contributions of this thesis work to the general accelerator community.

Firstly, the quasi-3D profile monitor developed here can be simply applied to other beam transport line with a minimum cost. It is based on the wire-grid profile monitor so only the data capture and signal processing units should be replaced, without touch on the existing beam line. With slightly upgrade, this monitor can be used to measure the complete quasi-3D beam profile for a single shot. Usually the beam profile refers to transverse profile, either in horizontal or vertical direction as in the case of a wire monitor. In contrary, the quasi-3D profile monitor provides a way in capturing the longitudinally dependent beam profile. In any possible case that the beam profile may vary along the longitudinal direction, the quasi-3D profile monitor developed here can serve as a cost-effective solution. It can be used to measure the longitudinal beam momentum modulation within a beam pulse as shown in this thesis. It can also be used to confirm whether the beam head and beam tail have the same beam size or not. It can also provide a more realistic relative particle intensity distribution in a quasi-3D way which is very helpful in the simulation work as initial distribution.

Secondly, the simulation code developed with this thesis is an indispensable tool in the design and study of the induction synchrotron. At present, the KEK-DA is the only demonstration facility. However, it is expected that with more technology breakthroughs, other induction synchrotron accelerators featuring widely-band acceleration and flexible beam manipulation will be constructed in the near future. The simulation code developed here will continue to be used in investigating the present KEK-DA and it will be updated to meet the needs of new facilities.

Appendix A

Simulation Design

The physics used in the simulation have beam discussed in Chapter 2 and Chapter 6. The design of the simulation code will be described here.

The simulation code has been developed in an Object-oriented programming (OOP) way so most building blocks are a series of classes which are designed to simulate the real object in an accelerator system.

We listed all the header files here in case some one would like to see how we designed the simulation code from the very beginning. The actual implementations is too long to be attached here.

The external settings files in the case of the KEK-DA are given in Appendix B. Similar files can be generated by the user for a totally different machine.

Table A.1: Development environment.

Develement Platform	Windows 10	Windows 7, 8.1
IDE	Visual Studio 2015 Community	Visual Studio 2013
Language	C++	
External Library	Intel MKL	Gnuplot

A.1 Class diagram

The class diagram is shown in Fig. A.1. The details of each class will be given in the next section. The brief description of each class are:

1). *Config* with the simulation settings imported in an external file;

2). *Particle* used mainly as the referential particle in a *Beam* object;

3). *Beam* hold the information of a beam such as the distribution;

4). *Element* base class standing for the real object in the system, a list of this can be used to build a beam line or ring.

5). *Drift* derived class from *Element*, straight section element, without magnetic field;

6). *Bend* derived class from *Element*, defined by k0 and k1;

7). *Quad* derived class from *Element*, quadrupole magnets;

8). *InductionCell* special element, no length, used to kick the beam with voltage pulse;

9). *Monitor* special element, no length, record the tracking information when the beam pass it;

10). *Beamline* require a element list to initialize, will be used to track the beam;

11). *Ring* derived class from *Beamline*, special *Beamline* in which beam can be tracked repeatedly;

12). *Boundary*, defined by an external file with a list of boundary shapes, imported as a object list by the *BeamLine* where it can be reached with an ID by the *element*;

13). *MagneticField* will be a property of a *Ring* object where it returns the Magnetic field with a given t.

14). *Gnuplot* used for plotting.

Simply speaking, after properly setting up each object, the *Beam* object will be used in the pass function of a *Beamline* object with specified simulation settings.
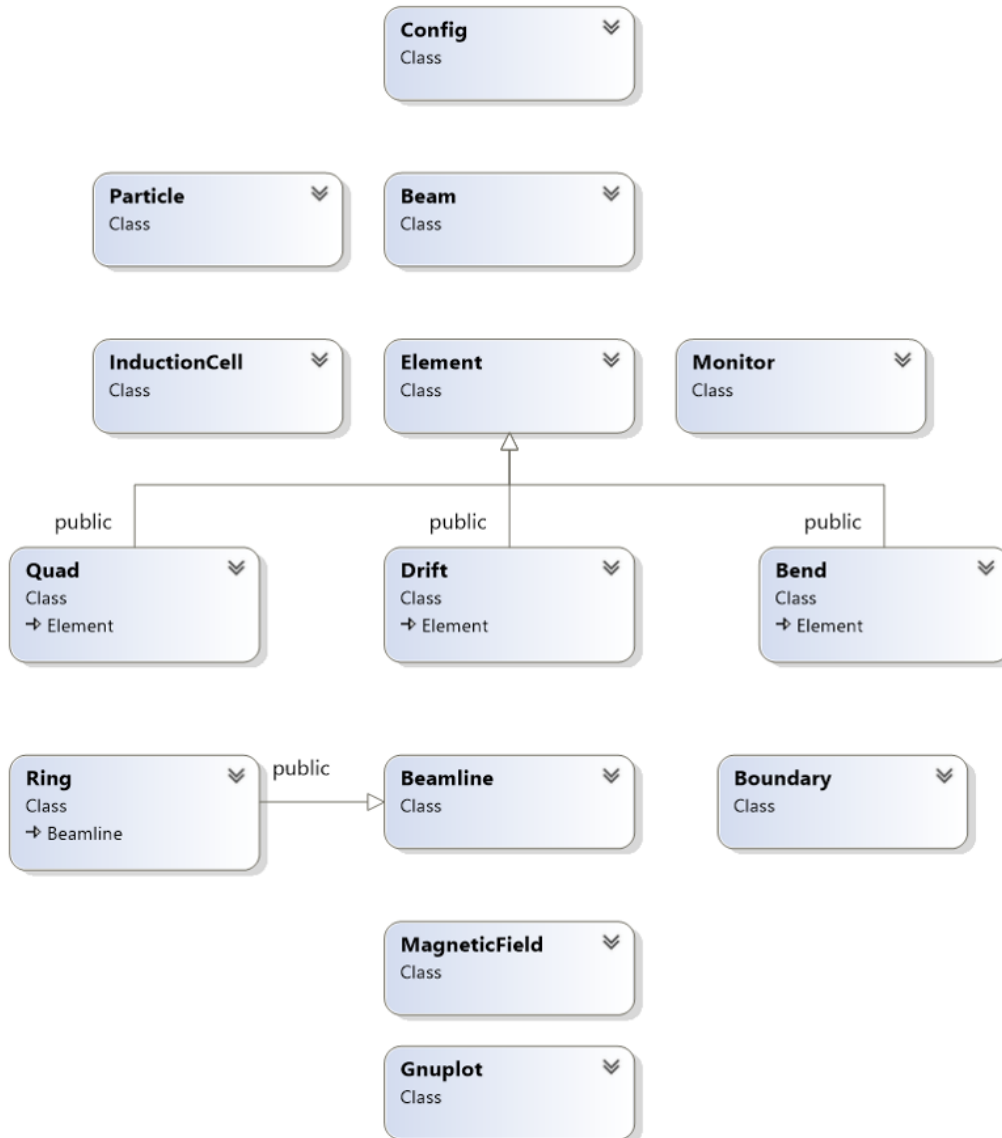
Figure A.1: Class diagram of the simulation code.

A.2 Class design

Config

Description

All the initial settings for the simulation will be imported by the program from a file at the beginning, default to be "configuration.txt" in the code. In order to pass these settings to different objects, these variables are save in a *Config* object. It will include the information for the reference particle, the file name for the distribution, the file names for the beam line layout and boundary list and other simulation related parameters. In addition, it also includes the grid number which can be set freely by the user. The flags like the space charge and chromaticity can be also set by the user at the beginning based on their needs.

By allow users to prepare their own distribution and beam line layout, this program can be applied to different machines with a great flexibility in running the simulation.

Members and Implementations

Listing A.1: Config Class

```cpp
#pragma once

class Config
{
public:
    //****referece particle****
    unsigned int A; // mass number
    unsigned int Q; // charge state
    double V;  //  [MV]
    //****beam****
    string distributionFileName;
    double totalCharge;//C
    unsigned int Nx;
    unsigned int Nz;
    //****beam line****
    string beamLineFileName;
    string boundaryFileName;
    //****simulation****
    unsigned int mode; // 0-lattice, 1-Bmin,2-Bac
    double stepSize; // [m]
```

```cpp
    double tMax; // [ms]
    unsigned int turnMax;
    unsigned int outputTurnStep;
    unsigned int B_mode;
    double B_rho;
    double B_f; // [Hz]
    double B_min;
    double B_max; // [T]
    double B_delay; //[s]
    double SC_Threshhold;
    //****flag****
    bool idealBminFlag;
    bool lossFlag;
    bool chromaticityFlag;
    bool spacechargeFlag;
    bool gpuFlag;

public:
    //load with default values
    Config();
    virtual ~Config();
    // import the Configuration from a file
    void import(string filename);
    // return the cofiguration details with a string
    string info();
};
```

Particle

Description

This class is mainly used to generate the referential particle object in a *Beam* object. Usually, it should have only one such object in a *beam* object.

It has the fundamental properties as a particle and these properties can be automatically updated when the particle is accelerated (for example, initial energy) or when it has to be synchronize with the external ramping magnetic field.

A *Particle* object should be initialized with A, Q and initial energy V.

Members and Implementations

Listing A.2: Particle Class

```cpp
class Particle
{
public:
    Particle();
    Particle(const double &A, const int &Q, const double &V);
    virtual ~Particle();
    unsigned int chargeState;
    double massNumber;
    double mass; //[kg]
    double beta;
    double gamma;
    double momentum;
    double restEnergy; //[MeV]
    double totalEnergy; //[MeV]
    double kineticEnergy; //[MeV]

    double selfClock;//[s], self timing
    double clockUpdate(double ds);

    // MV
    void accelerate(double v);
    // magnetic rigidity, [T.m]
    void synchronize(const double Brho);
    // set present particle to a new particle
    void set_new(const double &A, const int &Q, const double &V);

    // display the values at present
    string info();
};
```

Beam

Description

This class will be used to stand for a beam object which can interact with the *Beamline* object. Usually, there should be only one such an object in the simulation.

The most important properties of a *Beam* object are the referential particle and the beam distribution. The 3D PIC is also done in this object so the grid number is

necessary. The charge density from 3D PIC can be used directly to calculate the beam induced space charge potential and also output the beam intensity profile. Some RMS values or standard deviations, like the beam size and beam emittance, are also calculated here.

A *Beam* object should be initialized with A, Q and initial energy V for the referential particle and total charge for the beam with the grid numbers. Notice that we chose the same horizontal and vertical grid number, so only one number (Nx) is required here.

Members and Implementations

Listing A.3: Beam Class

```cpp
class Beam
{
public:
    //reference particle
    Particle referenceParticle;

    //beam
    vector<double> distributionArray;//6*N (x,xp,y,yp,ds,dpp)
    vector<unsigned int> surviveMark;//N 1-living 0-lost
    vector<unsigned int> selectedID; // selected ID for output
    unsigned int selectedNumber;
    unsigned int macroParticleNumber;
    unsigned int lostParticleNumber;
    unsigned int livingParticleNumber;
    double survivalRate;

    double totalCharge;
    double macroParticleCharge;

    double width;
    double height;
    double lengthTime;

    double xcenter;
    double ycenter;
    double zcenter;
```

```cpp
    double tcenter;

    double xmax;
    double xmin;
    double ymax;
    double ymin;
    double dtmax;
    double dtmin;
    double zmax;
    double zmin;


    //RMS value
    double mX, mY, mZ;//mean, or COD for X,Y, center for Z.
    double mXP, mYP, mDPP;
    double rmsX, rmsY, rmsZ;//size, in RMS
    double rmsXP, rmsYP, rmsDPP;//divergence
    double rmsEX, rmsEY, rmsEZ; // emittance
    double nrmsEX, nrmsEY, nrmsEZ; // normalized emittance
    double sX, sY, sZ;//size, in standard deviation
    double sXP, sYP, sDPP;//divergence
    double sEX, sEY, sEZ; // emittance
    double nsEX, nsEY, nsEZ; // normalized emittance


    unsigned int statisticsNumber;// 25 at present including survival rate

    //grid related
    unsigned int gridNumber;
    unsigned int gridN, gridNN, gridNz;
    vector<double> gridRho; //charge density on grid
    vector<int_3> gridIndex; //used externally, boundary class
    vector<double_3> gridSigma;

    vector<double_3> gridE;

public:
    Beam();
    Beam(unsigned int A_, unsigned int Q_, double V_,
        double totalCharge_, unsigned int Nx_, unsigned int Nz_);
    virtual ~Beam();
```

```cpp
    void sychronize(double Brho);

    void meshing_to_grid(double& xmin_, double& xmax_,
        double& ymin_, double& ymax_,
        double& zmin_, double& zmax_);

    // read distribution from an external file
    void external_distribution(string& path);

    // show distribution of the beam, >20 will be ignored
    void show_distribution_part(unsigned int maxNumber);
    ;

    /* statistical descriptioin */
    void statistical();

    // find the boundary of the beam
    void find_boundary();

    // show parameters at present for beam include reference particle and
        beam, simulation settings
    void info();
    void info_short();

    string info_statistical();

    // output the file to the "out" folder
    void output_distribution(string filename);
    void output_distribution_selected(string filename);
    // output the profile
    void output_profile(string filename);
};
```

Element

Description

This class is designed to stand for the drift sections and magnets in the accelerator system.

An element should have some basic properties like length and the cross section shape. Two shapes are considered in the simulation code: rectangular and elliptical. Because different element have different properties, so a *TypeID* is used to differentiate the element type.

The *Element* class is designed as a basic class which is not directly used in building the beam line. Instead, three derived class, *Drift*, *Bend* and *Quad* are designed with their own properties. The dipole coefficient ($k0$) and quadrupole coefficient ($k1$) of a magnetic field are used to define these magnets. At this moment, no higher order coefficients are considered.

As an element list (like Table B.1) is required to generate the beam line, to differentiate each element, they have properties like *id* in a beam line, *name* of the element and cross section *shape*. These parameters from the element list are required to initialize an *elmement* object.

Additional properties are required for the derived class in initialization. For example, $k0$ and $k1$ for *Bend* and *Quad* objects.

One important property of these elements is the transfer matrix, this should be set accordingly and when chromaticity is turned on, every particle in a beam will have a different transfer matrix. The transfer matrix depends on the particle energy and the step size, so during the particle transportation, the run-time temporary transfer matrix will be calculated.

Members and Implementations

Listing A.4: Element Class

```
/*
TYPEID:
   #TypeID
         0-Element
         1-Drift    2-Bend    3-     4-Quad    5-
         6-Sextuple 7-Monitor 8-InductionCell 9-InjKicker

   #crossSectionID
         0-Rectangular (a,b,ac,bc), if a=b, circular
         1-ellipse  (a,b,ac,bc), half width, half height, if a=b, square
             ac-deviation of the horizontal center from the referential
                 beam orbit
             bc-                vertical
```

```
TM: Transfer Matrix
    default TM includes no chromaticity
    for chromaticity, the TM depends on the dp/p

DERIVIED CLASSES
    Drift
    Bend
    Quad

*/

#pragma once
#include "Beam.h"
#include "Functions.h"
#include <amp.h>
#include<amp_short_vectors.h>

using namespace function;
using namespace concurrency;
using namespace concurrency::graphics;
//using namespace concurrency::precise_math;

class Element
{
public:
    Element(unsigned int id_, string name_, unsigned int crossSectionID_,
        double length_);
    virtual ~Element();

    unsigned int id;
    string name;
    unsigned int typeID;
    unsigned int crossSectionID;//boundary list ID

    double length;//default to be zero
    unsigned int lostParticleNumber;

    //transfer matrix for referential particle, particle dependent
    double TM[6][6]; //dynamically change by set_T

    // transfer twiss parameters
```

```cpp
    double TMtwiss[6][6]; //(3*3 for x, 3*3 for y)

    // display the transfer matrix
    //void show_TM();
    void info();
    string info_string();
    double presentPosition;


protected:
    void set_TMtwiss();

public:
    // return the determinant of the transfer matrix
    double TM_determinant();
    double TM_determinant_new();

    void transfer_twiss(double_2& beta, double_2& alpha, double_2& gamma);
    void transfer_dispersion(double_2& D_);

    // transfer the beam without chromaticity
    void transfer_single(double& x, double& xp,
        double& y,double& yp,
        double& z,double& dpp);
    void transfer_cpu(Beam& bunch);
    void transfer_gpu(Beam& bunch);
};

class Drift :
    public Element
{
public:
    Drift(unsigned int id_, string name_,
        unsigned int crossSectionShapeID_, double length_);
    virtual ~Drift();
    // no chromaticity
    void set_TM(double length, double gamma_0=1.0);
};

class Bend :
    public Element
```

```cpp
{
private:
    /*
    set TM with chromaticity, reltated to dpp, ds
    */
    void set_TM_C(double M[][6],
        double dpp, double length_, double k0_, double k1_,
        double gamma_0 = 1.0);
public:
    double k0;
    double k1;
public:
    Bend(unsigned int id_, string name_,
        unsigned int crossSectionShapeID_,
        double length_, double k0, double k1);
    virtual ~Bend();
    // no chromaticity
    void set_TM(double length_, double k0_, double k1_, double
        gamma_0=1.0);
    // First synchrotron radiation integral, I1, for momentum compaction
        factor in a ring
    double iOne(double D, double Dp);
    void transfer_chromaticity_cpu(Beam& bunch, double ds);
    void transfer_chromaticity_gpu(Beam& bunch, double ds);
};

class Quad :
    public Element
{
private:
    void set_TM_C(double M[][6],
        double dpp, double length_, double k1_t, double gamma_0 = 1.0);
public:
    double k1;
public:
    Quad(unsigned int id_, string name_,
        unsigned int crossSectionShapeID_,
        double length_, double k1);
    virtual ~Quad();
    // no chromaticity
    void set_TM(double length_, double k1_, double gamma_0 = 1.0);
```

```
    void transfer_chromaticity_cpu(Beam& bunch, double ds);
    void transfer_chromaticity_gpu(Beam& bunch, double ds);
};
```

InductionCell

Description

This is a special class designed to stand for the induction cell. It has a special element $TypeID$, 7.

At first, a base pulse is imported by initialization, then the base pulse can be used to kick the beam when there is no table which contains turn by turn settings for the pulse.

When the table is required, it will import the turn by turn settings and modify the pulse in different ways depending on this is a V_{acc} object or V_{bb} object.

The base pulse file name and the turn by turn table file name have names similar to the induction cell name. For example, if the name of the element is "IC_Vbb", then by default, the base pulse will be "IC_Vbb.txt" and the table file will be "IC_Vbb_Table.txt".

Any number of induction cells can be included in the element list with their own setting files. An whether to turn on these induction cells (ON) or whether to include its table settings ($tableFlag$) are set by the user in the element list.

Note that the base pulse can be arbitrary shape. The illustration in the comment of the source code is only used to differentiate the barrier bucket pulses and acceleration pulses.

Members and Implementations

Listing A.5: InductionCell Class

```
/*

DESCRIPTION
    id -- the id inside the vector which will hold the vector of ICs
    name -- name in the element list
    pulsetype --1, Vbb; 2,Vac
    pulse, double_2: time and voltage for key points

    pulse description:
```

```
pulse will be recorded as a sequance of (t,V) points
where t has a constant distant, delta t
so that for a given t, we can easily find its position index
and return the voltage at that position


single pulse
delay    width

       _____
       |       |  amplitude
_____|      |
_ _ _ _ _ _|      |

standard pulse set:

delay width duration

       _____
       |       |
_____|       |___
              |       |
              |_____|

standard with second amplitude: amplitude2 > 0.0
delay width duration      delay2      width2 duration2 tail

       _____              _____
       |       |   amplitude1          |       |  amplitude2*
_____|      |___        _____|      |___        ____
              |       |                              |       |
              |_____|                              |_____|

*tail is necessary if fall time exists, and should be larger than that
*amplitude2 can be different from amplitude1
*rise and fall time are not shown in the above figure

* set rise and fall time to zero yields square pulse, otherwise
    trapezoidal
* if necesary, sec distance, wid


? how to deal with that when front turn pulses last to this turn?
    set a remaining pulse sequence, add it for next use
```

```
        except for the external input mode, the code can reflect the
            acceleration
        voltage to the next use if a given window T is larger than the
            totalLength

    ON -true or false, pulse density control

*/

class InductionCell
{
public:
    unsigned int id;
    string name;
    unsigned int pulseType;// 1-Vbb 2-Vacc
    bool ON; //turn on or off the induction Cell

    //table related
    unsigned int tableTurnMax;
    unsigned int tableFlag;
    vector<double> tableDistance;
    vector<double> tableAmplitude;
    vector<bool> tableON;
    vector<double>tableT;

private:

    double totalLength;
    unsigned int pointNumber;
    double deltaT;
    double newDeltaT;
    double delayT;

    //present pulse
    double pulseBaseAmplitude;
    vector<double_2> pulseBase; //t,V
    vector<double_2> pulse;
    ////previous pulse, if exist
    //remaining pulse, if exist
    double pulseRemLength;
    vector<double_2> pulseRem;
```

```
public:

    InductionCell(unsigned int id_, string name_, unsigned int pulseType_
        = 1,
        bool ON_=0, bool tableFlag_ = 0);
    ~InductionCell();

    void info();
    // return a voltage at t
    double Voltage(double t);

    /*
    set pulses
    */
    // //import external profile
    void set_pulse_external(string filename);
    void read_in_table(string filename);
    void set_pulse(double distance_, double amplitude_);

    // kick the beam
    void pass_single(double& dt, double& dpp, double k);
    void pass_beam(Beam& beam, unsigned int turn);
    void output_pulse(string filename_, unsigned int turnID_=0);

};
```

Monitor

Description

Monitor is another special element with $TypeID = 8$. It save the information of the beam and its loss record when the beam passes it. Any number of monitors can be included at different places in the element list.

In the thesis work, we chose the location of the Bunch Monitor.

Members and Implementations

Listing A.6: Monitor Class

```cpp
class Monitor
{
public:
    unsigned int id;
    string name;

    unsigned int turnMax;
    vector<unsigned int> turnID;

    vector<double> lossRecorder;
    vector<double> time;

    unsigned int elementNumber;
    vector<double> elementPosition;//set by beam line
    vector<string> elementName;

    unsigned int statisticsNumber;
    vector<double> beamStatistics;

    string caseName;

    Monitor(unsigned int id_,string name_, string caseName_);
    ~Monitor();

    void initialize();

    // output the distribution of the beam
    void distribution(Beam& bunch, unsigned int turnID_);
    void beam_statistics(Beam& bunch, unsigned int turnID_);

    void info();

    //output the profile: horizontal, vertical, longitudinal
    void profile2D(unsigned int boundaryID, string filename);

    void save_to_file();
    void post_process();
    void plot_distribution();
    void plot_other();
    void show_message(string msg);
};
```

Beamline

Description

The *Beamline* class is designed to stand for the beam line in the accelerator system. The element list will be used by the *Beamline* object to build the beam line in the simulation and the beam will interact with the *Beamline* object. As a result, it has several groups of element. And a list of index to mark the sequence of each element in its own group. Beside, a group of boundaries which is looked up by a boundary id from each element. The Ring class is derived from the Beamline class as a special beam line which has properties like *turn*, *radius* and magnetic field.

When the beam passes each element, the transfer matrix will be called by individual element to transport the beam distribution or the space charge will be calculated with specific boundary shape and kick the beam if space charge flag is turned on.

A *Beamline* object can also calculate parameters like the Courant-Snyder parameters and dispersion functions.

Members and Implementations

Listing A.7: Beamline Class

```
/*
beamLineType
    0-transport line
    1-ring
*/

#ifndef BEAMLINE_H
#define BEAMLINE_H

#include "Element.h"
#include "Beam.h"
#include "Monitor.h"
#include "InductionCell.h"
#include "Boundary.h"
#include "MagneticField.h"
#include "Functions.h"
```

```cpp
#include <amp_short_vectors.h>
#include<sstream>
#include <fstream>

using namespace function;
using namespace concurrency::graphics;//double_3

class Beamline
{
protected:
    // read in a configuration file to build the beam line
    void _build(string path,string caseName);

    vector<int> _elementIndex;//element identifier, 1-8
    vector<int> _indexWithinContainer;//
    vector<double> _elementLength;//length for each element;
    vector<double> _elementPosition;
    vector<string> _elementName;

    vector<Drift> _Drift;//type 1
    vector<Bend> _Bend; //type 2
    vector<Quad> _Quad; //type 4
    vector<Monitor> _Monitor; //type 7
    vector<InductionCell> _InductionCell; //type 8

    vector<Boundary> _Boundary; //cross section list
    vector<int>_BoundaryIndex;

    vector<double> _position;
    vector<double_2> _beta;
    vector<double_2> _alpha;
    vector<double_2> _gamma;
    vector<double_2> _dispersion; /* m */
    vector<double_2> _acceptance; /* mm */
    vector<double_2> _acceptEmittance; /* mm.mrad */
    vector<int> _boundaryIDforLattice;
public:
    Beamline(unsigned int type, string path, string caseName);
    ~Beamline();
    unsigned int elementNumber;
    double length;
```

```cpp
string name;
//double s;
unsigned int beamLineType;

unsigned int stepCount;

double clock;
double distance;
unsigned int turn;
vector<double>lossRecorderTemp;
void set_boundary_profile(string path, unsigned int Nx, unsigned int
    Nz);

//display element
void show_element_select(unsigned int n);
void show_element_all();

// the twiss parameter along the line for a given set of twiss
    parameters
void twiss_para_line(double stepSize,
    double_2 beta_in,double_2 alpha_in, double_2 gamma_in,
    double_2 D_in);
// output the twiss parameters
void twiss_para_out(string filename);
void TM_out(string filename);

//pass the beam through a small stepsize
void pass_stepSize(Beam& beam, double ds,
    unsigned int elementIndex, unsigned int elementID,
    unsigned int boundaryID, bool chromaticityFlag_=0, bool
        spacechargeFlag_=0);
// pass the beam through the whole line
void pass_line(Beam& beam, double stepSize_,
    bool chromaticityFlag_=0, bool spaceChargeFlag_=0, bool
        lossFlag_=1);

void pass_particle(double ds,
    double& x, double& xp,
    double& y, double& yp,
    double& z, double& dpp);
void loss_mark(Beam& beam, unsigned int boundaryID);
```

```
    void monitor_record(Monitor& monitor_, Beam& beam, unsigned int
        turnStep_);

};

#endif

class Ring :
    public Beamline
{

public:
    //.x and .y
    double_2 beta0;
    double_2 alpha0;
    double_2 gamma0;
    double_2 bareTune;
    //.D(s) and D'(s)
    double_2 Dispersion0;

    double momentumCompactionFactor;
    double transitionGamma;
    double_2 natrualChromaticity;
    double averageRadius;

    //magnetic field related--unique to a ring
    MagneticField B;

public:
    Ring(unsigned int type, string path,string caseName, MagneticField B_);
    ~Ring();

    // the twiss parameters along the line, if this is a ring
    void twiss_para_ring(double stepSize);
    //periodic solution for a ring
    void periodic_twiss_para();

    void pass_ring(Beam& beam, double stepSize_, unsigned int turnMax_,
        bool chromaticityFlag_=0, bool spaceChargeFlag_=0, bool
            lossFlag_=1);
```

```
    void pass_ring_new(Beam& beam, double stepSize_, unsigned int turnMax_,
        bool chromaticityFlag_ = 0, bool spaceChargeFlag_ = 0, bool
            lossFlag_ = 1);

    void info();
    void info_out(string filename);
private:
    /*
    calculate the transitino gamma and momentum compaction factor and
        natural chromaticity
    after periodic_twiss_para() which calculate the initial beta, alpha
        and gamma
    */
    void momentum_compaction_factor_etc(double stepSize, double_2 D);

};
```

Boundary

Description

As mentioned, two boundary shapes are considered. A *Boundary* object has two roles in the simulation:

1). Judge the particle loss;

2). Calculate the beam induced space charge potential and kick the beam.

A boundary list will be imported by the *Beamline* object and each element in the *Beamline* object has a index to specify its boundary shape.

Intel MKL library is used in the simulation code to solve the linear system formed by the boundary matrix which is a sparse array. In fact, this is the most difficult part so we left more comments in the source code here.

Members and Implementations

Listing A.8: Boundary Class

```
/*
```

```
two boundary shape considered\
typeID 1-Rectangular, defined by two side length
       2-ellipse, defined by two arm length

linear solver for Ax=b, using MKL

Criterion: reflect the potential distribution
of the beam distribution
Too large: memory/computing consuming
too small: accuracy

[refer to page 3352 for the indexing description: MKL manual 2015]

NI - (ia) column
NJ - (ja) column indices for U triangle - none 0 element
NN - size for x and b, equal to the potential points

ia[NI]
ja[NJ]

a[NJ]

b[NN]
x[NN]

note that when alocate the memory, use pointer and new to allocate the
    memory
on the heap instead of directly initilize it in the class.

Initilization inside the class will result in "stack overflow error"
    because the
default stack size is only 1MB;

in case of a mesh of 64*64 is chosen, in this scheme

NN = 64*64;
NJ = 5*NN - 4;
NI = NN + 1;

fill ia, ja, and a considering the matrix
```

```
Symetric square boundary

-4  1    .... 1 ........
1   4   1..... 1.......
..........
.....1...1 4   1... 1.
..........
............ 1....1   4
*/

class Boundary
{
private:
    unsigned int N, Nrhs, NN, NI, NJ;
    unsigned int gridPointNum;
    MKL_INT n;

    MKL_INT *ia, *ja;
    double *a;
    MKL_INT mtype;      /* Real symmetric matrix */
    double *b, *x; // only used in solve, comment out
    MKL_INT nrhs;    /* Number of right hand sides. */
    /* Internal solver memory pointer pt, */
    /* 32-bit: int pt[64]; 64-bit: long int pt[64] */
    /* or void *pt[64] should be OK on both architectures */
    void *pt[64];
    /* Pardiso control parameters. */
    MKL_INT iparm[64];
    MKL_INT maxfct, mnum, phase, error, msglvl;
    /* Auxiliary variables. */
    //MKL_INT i;
    double ddum;        /* Double dummy */
    MKL_INT idum;       /* Integer dummy. */

    void _inilization_rect();//fill ia,ja,a
    void _inilization_ellipse();
public:
    unsigned int id;
    unsigned int typeID;
    string name;
    double rx;
```

```cpp
    double ry;
    double x0;
    double y0;
    double xmin, ymin, xmax, ymax;
    //sign to show the grid point is inside(1) or on the boundary(0)
    //used to set the b list
    int *gridPointMark;

    double gxmin;//grid minimum
    double gymin;
    double gr;//grid half width/height
    double d; //finite difference

    //longitudinal
    double gzmin,gzmax;
    double dz; //finite difference in longitudinal direction

private:
    void solve();
    void potential_to_E();
    vector<double_3> gridE;

public:
    Boundary(unsigned int id_,unsigned int typeID_, string name_,
        double rx_,double ry_,double x0_, double y0_,
        unsigned int Nx_=64, unsigned int Nz_=64);
    Boundary(const Boundary& no);//copy constructor
    Boundary& operator=(const Boundary& no);//copy assignment constructor
    virtual ~Boundary();

    inline bool inside_rect(double x, double y);
    inline bool inside_ellipse(double x, double y);
    bool inside(double x, double y);

    void test(double x,double y);
    void calibration(unsigned int particleNumber);
    void calibration3D(unsigned int particleNumber);
    void calibration3D_iterative(Beam& beam, unsigned int times=1);
    void slice_profile_plot(string filename, unsigned int n_);
    void phi_rho_print(unsigned int n);
    void phi_rho_out(string filename);
```

```
    void field_on_axes(string filename);
    void info();
    void info_short();


    // solver for the electric field on the grid for a beam distribution
    void SC_solver(Beam& beam);//self do the meshing
    void SC_solver_new(Beam& beam);//let the beam do the meshing
    //solve the sub3D electric field with iterative method
    void SC_solver_iterative(Beam& beam, unsigned int times=1);
    void SC_solver_iterative_new(Beam& beam, unsigned int times = 1);//let
        the beam do the meshing
    //// kick the beam over ds with electric field on the grid
    void SC_kicker(Beam& beam, double ds);
    void SC_pass(Beam& beam, double ds);

    void matrix_print();
};
```

MagneticField

Description

A *Magnetic* object will be used in a *Ring* object to stand for the ramping or static magnetic field. The basic function is giving the magnetic field at a specific time.

Members and Implementations

Listing A.9: MagneticField Class

```
/*
mode
0-static
1-linear(triangle, linear up and linear down)
2-sine wave like
*/

class MagneticField
{
public:
```

```cpp
    unsigned int mode;
    double Bmin;
    double Bmax;
    double f;
    double T;
    double w;
    double delay;
    double bendingRadius;

public:
    MagneticField();
    MagneticField(unsigned int mode_, double rho_=3.3, double Bmin_ = 0.0,
        double Bmax_ = 0.0,
        double f_ = 1.0, double delay_=0.0);
    MagneticField(const MagneticField& no);

    ~MagneticField();

    // set the magnet for a specific reference particle
    void set_Bmin_from_particle(double amu, double ChargeState, double
        initialV);
    // // return the magnetic field at t
    double B(double t);
    // display the present information of the magnetic field
    void info();
    //output the magnetic field from t=0 to half of the period
    void output(string filename, unsigned int N=100);
};

#endif
```

A.3   Main body of the simulation code

With all these classes defined, the running part of the simulation code is very simple. In fact, this part can be easily modified to simulate for various purposes.

<div align="center">Listing A.10: Main body of the simulation code</div>

```cpp
// Trais.cpp :Xingguang Liu, 2015
//
```

176

```cpp
#include <cstdlib>
#include <iostream>

#include "Config.h"
#include "Beam.h"
#include "Beamline.h"
#include "MagneticField.h"


void main()
{
    /* ------------------------------------------ */
    // -----------0. CONFIGURATION INPUT
    /* ------------------------------------------ */
    Config conf;//default
    conf.import("in/configuration.txt");//external
    cout<<conf.info()<<endl;
    /* ------------------------------------------ */
    // --------I. PREPARATION: ACCELERATOR AND BEAM
    /* ------------------------------------------ */
    //1.1 Beam simple
    Beam beam(conf.A, conf.Q, conf.V,
            conf.totalCharge, conf.Nx, conf.Nz);
    //1.2 magnetic field
    MagneticField B(conf.B_mode,
        conf.B_rho, conf.B_min, conf.B_max,
        conf.B_f, conf.B_delay);
    if (conf.idealBminFlag == 1)
    {
        B.set_Bmin_from_particle(conf.A,
                        conf.Q, conf.V);
    }
    //1.3 accelerator
    string beamLinePath =
                "in/" + conf.beamLineFileName;
    Ring ring(1, beamLinePath, "default", B);
    string boundaryPath =
                "in/" + conf.boundaryFileName;
    ring.set_boundary_profile(boundaryPath,
                conf.Nx, conf.Nz);


    /* ------------------------------------------ */
    /* -----------II. SIMULATION MODE*/
    /* ------------------------------------------ */
```

177

```cpp
if (conf.mode == 0)
{
    cout <<
    "mode 0: Lattice calculation, is selected."
    << endl;
    //0.1 lattice calculation
    if (ring.beamLineType == 1)
    {
        ring.twiss_para_ring(conf.stepSize);
        string twissOutFilepath
                        = "out/twiss.txt";
        ring.twiss_para_out(twissOutFilepath);
    }
    else
    {
        cout<<
        "please define the beam line as a ring."
        <<endl;
    }
}
else if (conf.mode ==1)
{
    cout<<
    "mode 1: Static magnetic field with Vbb, is selected."
    <<endl;
    //check the B field
    if (B.mode != 0)
    {
        cout<<
        "ERROR: Please set the mode of magnetic field to be 0!"
        <<endl;
    }
    //just in case, set the B as Bmin.
    B.Bmax = B.Bmin;
    B.mode = 1;

    //1.1 import the beam distribution
    cout<<"Import beam generation."<<endl;
    string distributionPath =
                    "in/" + conf.distributionFileName;
    beam.external_distribution(distributionPath);

    //1.1-A temp use for injection error
    cout << "injection error analysis" << endl;
    double Errorx = 0.01;
    double Errory = 0.01;
```

```cpp
        double Errorxp = 0.01;
        double Erroryp = 0.01;
        for (unsigned int i = 0;
                i < beam.macroParticleNumber; i++)
        {
            //beam.distributionArray[i * 6]   += Errorx;
            //beam.distributionArray[i * 6+1] += Errorxp;
            beam.distributionArray[i * 6+2] += Errory;
            //beam.distributionArray[i * 6+3] += Erroryp;
        }

        //1.2 tracking the beam
        ring.pass_ring(beam, conf.stepSize, conf.turnMax,
            conf.chromaticityFlag,
            conf.spacechargeFlag,
            conf.lossFlag);

}
else if (conf.mode == 2)
{
        cout<<
        "mode 2: Ramping magnetic field with Vbb & Vacc, is selected."
        <<endl;
        //check the B field
        if (B.mode == 0)
        {
            cout<<
            "ERROR: magnetic field shoulbe be 1 (linear) or 2 (cos)!"
            <<endl;
        }
        //1.1 import the beam distribution
        cout << "Import beam generation."<<endl;
        string distributionPath =
                        "in/" + conf.distributionFileName;
        beam.external_distribution(distributionPath);

        //1.2 tracking the beam
        ring.pass_ring(beam, conf.stepSize, conf.turnMax,
            conf.chromaticityFlag,
            conf.spacechargeFlag,
            conf.lossFlag);
}
else
{
        cout <<
        "The mode should be set to be 0, 1 or 2."
```

```
        <<endl;
    }

    /* ------------------------------------------------ */
    /* -----------III. SIMULATION END */
    /* ------------------------------------------------ */

    system("pause");
}
```

Appendix B

Setting files for the simulation of the KEK-DA ring

B.1 Distribution generation

Mathematica code is used to generate the multivariate distributions used in the simulation, especially for the transverse phase space distribution. For example, Fig. B.1 generate a 2D phase space distribution with n particles defined by the Courant-Snyder parameters β (in meter),α and the emittance ε(in $m.rad$), all values set to be one σ.

```
test[β_, α_, ε_, n_] := Module[{σ1, σ2, γ, a, b, H, ρ, p0, p1, p2, p3},

    γ = (1 + α²)/β ;
    σ1 = √(β ε) ;
    σ2 = √(γ ε) ;
    H = 1/2 (β + γ) ;
    ρ = 1/(H + √(H² - 1)) ;
    (*ρ=α/(γ-β)*) ;
    a = 2;
    b = 1;
    (*ρ=0.2;*)
    data =
     RandomVariate[d = MultinormalDistribution[{0, 0}, {{σ1 * σ1, ρ σ1 σ2}, {ρ σ1 σ2, σ2 * σ2}}],
      n];
```

Figure B.1: *Mathematica* code example for 2D normal distribution.

The result with $test[3.60454, -0.21604, 25 * 10^{-6}, 10^4]$ is plotted in Fig. B.2.
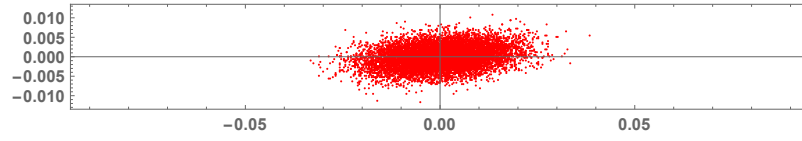
Figure B.2: Example of 2D normal distribution.

B.2   Element list

The complete element list of the KEK-DA ring is shown in Table B.1. There are 65 elements in total. For the format and definition, see Appendix A.

Table B.1: Complete element list of the KEK-DA ring.

Type ID	Name	Shape ID	Length[m]	k0	k1
1	S1_3	3	0.32	0	0
2	M1_F1	3	0.63	0.092	1.096
2	M1_H1	3	0.04	0.092	0
2	M1_D1	3	1.26	0.092	-1.103
2	M1_H2	3	0.04	0.092	0
2	M1_F2	3	0.63	0.092	1.096
1	S2_1	5	0.72	0	0
1	S2_2	5	0.32	0	0
1	S2_3	5	0.42	0	0
1	S2_4	5	0.30	0	0
1	S2_5	3	0.37	0	0
2	M2_F1	3	0.63	0.092	1.096
2	M2_H1	3	0.04	0.092	0.000
2	M2_D1	3	1.26	0.092	-1.103
2	M2_H2	3	0.04	0.092	0.000
2	M2_F2	3	0.63	0.092	1.096

1	S3_1	1	1.01	0	0
1	S3_2	1	0.30	0	0
1	S3_3	1	0.81	0	0
2	M3_F1	3	0.63	0.092	1.096
2	M3_H1	3	0.04	0.092	0.000
2	M3_D1	3	1.26	0.092	-1.103
2	M3_H2	3	0.04	0.092	0
2	M3_F2	3	0.63	0.092	1.096
1	S4_1	3	1.06	0	0
1	S4_2	3	1.06	0	0
2	M4_F1	3	0.63	0.092	1.096
2	M4_H1	3	0.04	0.092	0
2	M4_D1	3	1.26	0.092	-1.103
2	M4_H2	3	0.04	0.092	0
2	M4_F2	3	0.63	0.092	1.096
1	S5_1	3	1.06	0	0
7	B_Monitor	3	0	0	0
1	S5_2	3	1.06	0	0
2	M5_F1	3	0.63	0.092	1.096
2	M5_H1	3	0.04	0.092	0
2	M5_D1	3	1.26	0.092	-1.103
2	M5_H2	3	0.04	0.092	0
2	M5_F2	3	0.63	0.092	1.096
1	S6_1	1	1.06	0	0
8	IC_Vbb	1	0	0	0
1	S6_2	1	1.06	0	0
2	M6_F1	3	0.63	0.092	1.096

2	M6_H1	3	0.04	0.092	0
2	M6_D1	3	1.26	0.092	-1.103
2	M6_H2	3	0.04	0.092	0
2	M6_F2	3	0.63	0.092	1.096
1	S7_1	1	1.06	0	0
8	IC_Vac	1	0	0	0
1	S7_2	1	1.06	0	0
2	M7_F1	3	0.63	0.092	1.096
2	M7_H1	3	0.04	0.092	0
2	M7_D1	3	1.26	0.092	-1.103
2	M7_H2	3	0.04	0.092	0
2	M7_F2	3	0.63	0.092	1.096
1	S8_1	1	0.28	0	0
1	S8_2	1	1.02	0	0
1	S8_3	1	0.82	0	0
2	M8_F1	3	0.63	0.092	1.096
2	M8_H1	3	0.04	0.092	0
2	M8_D1	3	1.26	0.092	-1.103
2	M8_H2	3	0.04	0.092	0
2	M8_F2	3	0.63	0.092	1.096
1	S1_1	3	1.00	0	0
1	S1_2	2	0.80	0.040	0

B.3 Boundary list

In all there are five types of boundaries are considered in the KEK-DA ring which are very close to the real ones. They are shown in Fig. B.3. We could see the extraction kickers ("kext/bext") and septum have the smallest boundary size in the vertical

direction. The straight section is assumed as a circular shape with a large size. Note that the "septum", which also has a very small vertical size, comes into effect only in extracting the beam from the KEK-DA ring, so this boundary shape is not used for present simulation.

These shape are summarized in the following table which will be imported by the simulation code.
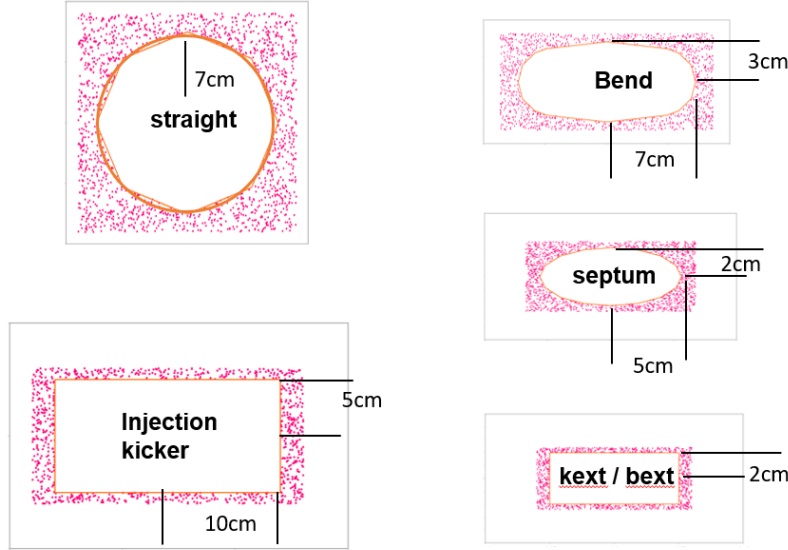
Figure B.3: Boundaries considered in the simulation.

Table B.2: Boundary list in KEK-DA ring.

ID	type ID	name	rx[m]	ry[m]	x0[m]	y0[m]
1	2	idc	0.07	0.07	0	0
2	1	kinj	0.1	0.05	0	0
3	2	blw	0.07	0.03	0	0
4	2	sep	0.05	0.02	0	0
5	1	kext	0.05	0.02	0	0

In case that we don't want the beam loss affect the beam evolution, a larger

boundary list is used in the simulation by increasing all the width rx and height ry to be 10 cm in Table B.2, namely,

Table B.3: Larger boundary list for the KEK-DA ring.

ID	typeID	name	rx[m]	ry[m]	x0[m]	y0[m]
1	2	idc	0.1	0.1	0	0
2	1	kinj	0.1	0.1	0	0
3	2	blw	0.1	0.1	0	0
4	2	sep	0.1	0.1	0	0
5	1	kext	0.1	0.1	0	0

B.4   Simulation configuration

Other simulation related parameters are set through the configuration file which looks like,

Table B.4: Simulation settings in configuration file.

#referece particle	
A(amu)	4
Q	1
V[MV]	0.2
#***beam	
distributionFile	distribution.txt
totalCharge[C]	200e-12
gridNx	64
gridNz	50
#***beamline	

boundaryFile	boundary.txt
ring	ring.txt
#***simulation	
mode	1
stepSize[m]	0.2
t_max[ms]	5
turn_max	100
output_turn_step	1
B_mode	0
B_rho	3.3
B_f[Hz]	10
B_min[T]	0.0391
B_max[T]	0.3
B_delay[ms]	0.0
SC_Threshhold[0-1]	0.1
#***flag	
Flag_ideal_Bmin	1
Flag_Loss	1
Flag_Chromaticity	0
Flag_SpaceChargeEffects	1
Flag_gpu	0

B.5   Pulse profile settings

The pulse profile are used for the induction cell, when it is called, it will kick the beam with a pre-defined pulse profile (in Simulation Mode 1) or a turn-based pulse profile defined by another table (Simulation Mode 2), just as in the beam commissioning.

The predefined pulse profile are imported as "pulseBase" which can be used directly or modified with the table in Simulation Mode 2. The file names by default are set

based on the element name of the induction cell. For example, for the induction cell used for acceleration defined in Table B.1, "IC_Vac", the "pulseBase" profile should be named as "IC_Vac.txt" and the table for this induction cell is imported through "IC_Vac_table.txt". The table can be calculated with an external code, for example, an *Mathematica* one. Notice that this table file should contain enough turns of information used to properly set the pulses for each turn in the simulation. In this way, the program provides the largest flexibility for the user to import a predefined pulse whether it is from the experiment or generated with a function. The external table can also be used to test cases like the over-acceleration or less-acceleration.

These two files look like(partly shown),

Listing B.1: IC_Vac.txt

```
#t[s]    V
0.0E+00 0
2.1E−08 515
4.1E−08 1000
6.2E−08 1000
8.2E−08 1000
```

Listing B.2: IC_Vac_table.txt

#turn	width[us]	V	ON	stage	time[us]				
	T[us]		Vrequried[V]	Vaccu[V]	dpp[%]				
1	4.05	0	0	1	0.0E+00	12.14	0.78	0.00	0.00
2	4.05	0	0	1	1.2E−05	12.14	1.56	0.78	0.00
3	4.05	0	0	1	2.4E−05	12.14	2.33	2.33	0.00
4	4.05	0	0	1	3.6E−05	12.14	3.11	4.67	0.00
5	4.05	0	0	1	4.9E−05	12.14	3.89	7.78	0.00
6	4.05	0	0	1	6.1E−05	12.14	4.67	11.67	0.00
7	4.05	0	0	1	7.3E−05	12.14	5.45	16.34	0.00
8	4.05	0	0	1	8.5E−05	12.14	6.23	21.79	0.01
98	4.01	0	0	1	1.2E−03	12.03	75.97	192.00	0.05
99	4.01	0	0	1	1.2E−03	12.03	76.74	267.97	0.07
100	4.01	0	0	1	1.2E−03	12.03	77.51	344.71	0.09
101	4.01	500	1	1	1.2E−03	12.02	78.28	422.22	0.11
102	4.01	0	0	1	1.2E−03	12.02	79.05	0.50	0.00
103	4.01	0	0	1	1.2E−03	12.02	79.81	79.55	0.02
104	4.01	0	0	1	1.2E−03	12.02	80.58	159.36	0.04
105	4.01	0	0	1	1.3E−03	12.02	81.35	239.94	0.06
106	4.00	0	0	1	1.3E−03	12.01	82.12	321.29	0.08
107	4.00	0	0	1	1.3E−03	12.01	82.88	403.41	0.10
108	4.00	500	1	1	1.3E−03	12.01	83.65	486.30	0.12
1498	1.93	1000	1	2	1.3E−02	5.80	754.61	261.73	0.07

1499	1.93	0	0	2	1.3E−02	5.80	754.86	16.34	0.00
1500	1.93	1000	1	2	1.3E−02	5.80	755.11	771.20	0.19
1501	1.93	1000	1	2	1.3E−02	5.80	755.36	526.31	0.13
1502	1.93	1000	1	2	1.3E−02	5.79	755.61	281.67	0.07
1503	1.93	0	0	2	1.3E−02	5.79	755.86	37.29	0.01

Acknowledgement

This thesis could not have been done without the tremendous support and help from many people around me. I would like to express my greatest gratitude to them.

First and foremost, I have to express my deepest appreciation to my primary supervisor, Professor Ken Takayama who have spent so much time in training me since I was admitted to the KEK-DA group five years ago as a Master student. I never imagined that I would have a opportunity to study the heavy ion accelerator from the ion source to ring physics without entering such a group. I can not figure out a better supervisor who could be so serious and patient in training me in the experimental skills and theoretical analysis. I learned so much from him not only in the work but also in the daily life. He is just that kind of scientist I wanted to become so I feel so lucky that I could be his student and have spent so many years with him.

My special appreciation also goes to my vice supervisor, Professor Kazuhiko Horioka, who is also a great scientist with great patience. I never forgot those days I spent in his laboratories, cracking the problems in the deep night, participating in the seminars and partying with other teachers and students. He also helped me deal with all the procedures in the campus side and encouraged me when I had troubles in the study or daily life. During my thesis examination, his insightful comments helped me finish this thesis.

I have to give my special thanks to other reviewers of my thesis: to Professor Kikuchi who had to travel for a long distance every time for my thesis examination, to Professor Hayashizaki who shared his critical remarks on my thesis writing and presentation, to Professor Xiao whose advices on the simulation played a very important role in the thesis work and finally and to Professor Hasegawa who gave encouraging remarks on my thesis. Without the valuable comments and advices from all these reviewers, the thesis would never be in present shape.

In the process of the development of the simulation code which is a core part of this thesis, there are three specific persons I want to express my gratitude. My thank-you goes first to Professor Jeffrey A. Holmes who shared the source code of

191

List of Figures

194

List of Tables

Bibliography

[1] K. Takayama and J. Kishiro. Induction synchrotron. *Nucl. Instrum. Methods Phys. Res., Sect. A*, 451(1):304 – 317, 2000.

[2] K. Takayama, Y. Arakida, T. Iwashita, Y. Shimosaki, T. Dixit, and K. Torikai. All-ion accelerators: An injector-free synchrotron. *Journal of Applied Physics*, 101(6):063304, 2007.

[3] K. Takayama, J. Kishiro, M. Sakuda, Y. Shimosaki, and M. Wake. Superbunch Hadron Colliders. *Phys. Rev. Lett.*, 88(14):144801, March 2002.

[4] K. Takayam, Y. Arakida, T. Dixit, T. Iwashita, T. Kono, E. Nakamura, K. Otsuka, Y. Shimosaki, K. Torikai, and M. Wake. Experimental Demonstration of the Induction Synchrotron. *Phys. Rev. Lett.*, 98(5):8–11, January 2007.

[5] T. Iwashita, T. Adachi, K. Takayama, K. W. Leo, T. Arai, Y. Arakida, M. Hashimoto, E. Kadokura, M. Kawai, T. Kawakubo, , T. Kubo, K. Koyama, H. Nakanishi, K. Okazaki, K. Okamura, H. Someya, A. Takagi, A. Tokuchi, and M. Wake. KEK Digital Accelerator. *Phys. Rev. ST Accel. Beams*, 14:071301, Jul 2011.

[6] K. Takayama, T. Yoshimoto, M. Barata, K. W. Leo, X. Liu, T. Iwashita, S. Harada, T. Adachi, T. Arai, D. Arakawa, H. Asao, E. Kadokura, T. Kawakubo, H. Nakanishi, Y. Okada, K. Okamura, K. Okazaki, A. Takagi, S. Takano, and M. Wake. Induction Acceleration of Heavy Ions in the KEK Digital Accelerator: Demonstration of a Fast-Cycling Induction Synchrotron. *Phys. Rev. Spec. Top. Accel Beams*, 17(1):010101, January 2014.

[7] T. Yoshimoto, M. Barata, T. Iwashita, S. Harada, D. Arakawa, T. Arai, X. Liu, T. Adachi, H. Asao, E. Kadokura, T. Kawakubo, T. Kubo, K. W. Leo, H. Nakanishi, Y. Okada, K. Okamura, K. Okazaki, H. Someya, K. Takayama, and M. Wake.

Heavy Ion Beam Acceleration in the KEK Digital Accelerator: Induction Acceleration from 200 keV To a few Tens of MeV. *Nucl. Instrum. Methods Phys. Res., Sect. A*, 733:141–146, January 2014.

[8] X. Liu, T. Yoshimoto, K. Takayama, T. Adachi, E. Kadokura, N. Munemoto, S. Takano, T. Kawakubo, K. Okamura, H. Kobayashi, and M. Hirose. Injection and Induction Acceleration of Ar3+ in the KEK Digital Accelerator. *Laser Part. Beams*, 33(02):237–243, 2015.

[9] H. Goldstein, C. Poole, and J. Safko. *Classical Mechanics*. Addison-Wesley, third edition, 2001.

[10] E. D.Courant, M. S. Livingston, and H. S. Snyder. The Strong-Focusing Synchroton: A New High Energy Accelerator. *Phys. Rev.*, 88:1190–1196, Dec 1952.

[11] R. Q. Twiss and N. H. Frank. Orbital Stability in a Proton Synchrotron. *Rev. Sci. Instrum.*, 20(1):1, 1949.

[12] T. Dixit, T. Iwashita, and K. Takayama. Induction Acceleration Scenario From an Extremely Low Energy in The KEK All-Ion Accelerator. *Nucl. Instrum. Methods Phys. Res., Sect. A*, 602(2):326–336, April 2009.

[13] T. Adachi, T. Arai, K. W. Leo, K. Takayama, and A. Tokuchi. A Solid-State Marx Generator Driven Einzel Lens Chopper. *Rev. Sci. Instrum.*, 82(8):083305, August 2011.

[14] T. Adachi and T. Kawakubo. Electrostatic Injection Kicker for the KEK Digital Accelerator. *Phys. Rev. Spec. Top. Accel Beams*, 16(5):053501, May 2013.

[15] H. Kobayashi, T. Kawakubo, and A. Tokuchi. Electrostatic Injection Kicker for the KEK Digital Accelerator Driven by SI-thyristor Matrix Array Power System. In *Proceedings of EAPPC 2014*, Kumamoto, 2014.

[16] H. Kobayashi, X. Liu, T. Kawakubo, and T. Adachi. SI-Thyristor Matrix Array Driven Electrostatic Injection Kicker for the KEK Digital Accelerator and Beam Dynamics Analysis of Injection. In *Proceedings of HIAT 2015*, Yokohama, 2015.

[17] K. Okamura, K. Ise, M. Wake, K. Takaki, Y. Osawa, and K. Takayama. Novel Package of siC-JFET for a Switching Pulse Supply Operating at 1 MHz for an Induction Synchrotron. *IEEE Trans. Plasma Sci.*, 40(9):2205–2210, 2012.

[18] R. Geller. *Electron Cyclotron Resonance Ion Sources and ECR Plasmas.* Institute of Physics, Bristol, first edition edition, 1996.

[19] J. A. Bittencourt. *Fundamentals of Plasma Physics.* Springer New York, New York, NY, 2004.

[20] K. W. Leo. *Ion Beam Handling by an Einzel Lens Chopper for the KEK Digital Accelerator.* PhD thesis, Graduate University for Advanced Studies, 2012.

[21] I. G. Brown. *ECR Ion Sources.* Wiley-VCH Verlag GmbH and Co. KGaA, 2005.

[22] K. W. Leo, T. Adachi, T. Arai, and K. Takayama. Einzel Lens Chopper and Behavior of the Chopped Beam in the KEK Digital Accelerator. *Phys. Rev. Spec. Top. Accel Beams*, 16(4):043502, April 2013.

[23] A. G. Drentje. Techniques and mechanisms applied in electron cyclotron resonance sources for highly charged ions. *Rev. Sci. Instrum.*, 74(5):2631, 2003.

[24] Digital accelerator note. Internal report, KEK.

[25] Y. Shimosaki, E. Nakamura, K. Takayama, K. Torikai, M. Watanabe, M. Nakajima, and K. Horioka. Beam-Dynamic Effects of a Droop in an Induction Accelerating Voltage. *Phys. Rev. Spec. Top. Accel Beams*, 7(1):1–8, January 2004.

[26] X. Liu. Ion Beam Motion and Longitudinal Space-charge Effects in the KEK Digital Accelerator. Master's thesis, Tokyo Institute of Technology, 2012.

[27] X. Liu, T. Adachi, S. Harada, T. Iwashita, K. Takayama, and T. Yoshimoto. Longitudinal Beam Motion in the KEK Digital Accelerator : Tracking Simulation and Experimental Results. *Proceedings of HIAT 2012*, pages 83–88, 2012.

[28] A. Bazzani, E. Todesco, G. Turchetti, and G. Servizi. A Normal Form Approach to the Theory of Nonlinear Betatronic Motion, 1994.

[29] G. Franchetti, I. Hofmann, and G. Turchetti. Six-dimensional Approach to the Beam Dynamics in HIDIF Scenario. *Nucl. Instrum. Methods Phys. Res., Sect. A*, 415(1-2):450–454, 1998.

[30] R. Beatson and L. Greengard. *A short course on fast multipole methods.* 1997.

[31] Y. Shimosaki. *Roles of the Nonlinear Resonance due to the Oscillating Beam Core in the Process of the Halo Formation to Equilibrium State in High Intensity Proton Beam.* PhD thesis, Kyushu University, 2000.

[32] F. W. Jones, W. Mall, and C. Geneva. A Method for Incorporating Image Forces in Multiparticle Tracking With Space Charge. In *EPAC 2000*, pages 1381–1383, Vienna, 2000.

[33] W. H. Press, S. A. Teukolsky, W. T. Vetterling, and B. P. Flannery. *Numerical Recipes 3rd Edition: The Art of Scientific Computing.* Cambridge University Press, third edition edition, 2007.

[34] L. Vorobiev and R. York. Space charge calculations for sub-three-dimensional particle-in-cell code. *Phys. Rev. Spec. Top. Accel Beams*, 3(11):1–5, 2000.

[35] T. Kikuchi and K. Horioka. Beam behavior under a non-stationary state in high-current heavy ion beams. *Nucl. Instrum. Methods Phys. Res., Sect. A*, 606(1-2):31–36, jul 2009.

[36] K. Takayama, T. Adachi, T. Arai, D. Arakawa, H. Asao, Y. Barata, S. Harada, K. Horioka, T. Iwata, E. Kadokura, T. Kwakubo, T. Kubo, K. W. Leo, X. Liu, K. Mochiki, N. Munemoto, H. Nakanishi, Y. Okada, K. Okamura, M. Okamura, K. Okazaki, H. Someya, K. Takahashi, S. Takano, M. Wake, and T. Yoshimoto. Heavy Ion Beam Factory for Material Science Based on the KEK Digital Accelerator. *Nucl. Instrum. Methods Phys. Res., Sect. B*, pages 1–7, June 2013.

[37] M. Hirose, K. Takayama, T. Yoshimoto, and X. Liu. Beam Confinement Dynamics in a Barrier Bucket. In *Proceedings of HIAT 2015*, 2015.